Investigations on the capabilities of THz production at the PITZ facility

Dissertation
zur Erlangung des Doktorgrades
an der Fakultät für Mathematik, Informatik und Naturwissenschaften
Fachbereichs Physik
der Universität Hamburg

vorgelegt von
Prach Boonpornprasert

Hamburg
2020

Gutachter/innen der Dissertation:	Prof. Dr. Jörg Roßbach Dr. Mikhail Krasilnikov
Zusammensetzung der Prüfungskommission:	Prof. Dr. Sven-Olaf Moch Prof. Dr. Jörg Roßbach Prof. Dr. Wolfgang Hillert Dr. Mikhail Krasilnikov Dr. Evgeny Schneidmiller
Vorsitzende/r der Prüfungskommission:	Prof. Dr. Sven-Olaf Moch
Datum der Disputation:	24.01.2020
Vorsitzender Fach- Promotionsausschusses PHYSIK:	Prof. Dr. Günter Hans Walter Sigl
Leiter des Fachbereichs PHYSIK:	Prof. Dr. Wolfgang Hansen
Dekan der Fakultät MIN:	Prof. Dr. Heinrich Graener

Eidesstattliche Versicherung

Hiermit versichere ich an Eides statt, die vorliegende Dissertationsschrift selbst verfasst und keine anderen als die angegebenen Hilfsmittel und Quellen benutzt zu haben.

Die eingereichte schriftliche Fassung entspricht der auf dem elektronischen Speichermedium.

Die Dissertation wurde in der vorgelegten oder einer ähnlichen Form nicht schon einmal in einem früheren Promotionsverfahren angenommen oder als ungenügend beurteilt.

Hamburg, den 17.10.2019

Prach Boonpornprasert

Acknowledgement

I would like to express my very great appreciation to:

- Dr. Mikhail Krasilnikov, Prof. Dr. Jörg Roßbach and Dr. Frank Stephan for supervising, guidance, encouragement to do this work and proofreading the thesis;
- All member of the PITZ group from 2013-2019 for many useful discussions and providing a nice working atmosphere;
- Dr. Matthias Gross, Dr. Li Xiangkun, Dr. Hamed Shaker, Dr. Osip Lishilin, James Good, Gregor Loisch, and Raffael Niemczyk for proofreading the thesis;
- Engineers and technical staff at PITZ group for their helpful;
- Dr. Mikhail Yurkov, Dr. Evgeny Schneidmiller, Dr. Barbara Marchetti, Dr. Steffen Wunderlich and Dr. Francois Lemery, colleagues from DESY Hamburg, for many useful discussions.
- Dr. Bernhard Schmidt for the THzTransport code.
- Assoc. Prof. Dr. Chitrlada Thongbai, Asst. Prof. Dr. Sakhorn Rimjaem and Asst. Prof. Dr. Jatuporn Saisut from Chiang Mai University, Thailand, for many useful discussions.
- All my colleagues who pursued PhD during my time at PITZ, Dr. Igor Isaev, Dr. Georgios Kourkafas, Dr. Osip Lishilin, Gaurav Pathak, James Good, Gregor Loisch, Raffael Niemczyk, Georgi Georgiev for their helpful;
- My family, especially my mother and my brother, for their support.

Abstract

The European XFEL has planned to perform pump-probe experiments by using its x-ray pulses and THz pulses. A promising concept to provide the THz pulses is to generate them using a tunable high-power accelerator-based THz source. The Photo Injector Test Facility at DESY in Zeuthen (PITZ) can serve as a prototype for the development of the THz source. This thesis investigates the capabilities to generate THz pulses using electron bunches from the PITZ accelerator and three methods of THz radiation generation including Self-Amplification of Spontaneous Emission Free-Electron Lasers (SASE FELs), Coherent Transition Radiation (CTR), and Coherent Diffraction Radiation (CDR).

Studies of the THz SASE FEL using 4 nC electron beams and an APPLE-II type undulator with a period length of 40 mm in the helical mode were performed. Start-to-End (S2E) simulations show that FEL pulse energies at 100 μm and 20 μm wavelengths (corresponding to 3 THz and 15 THz frequencies) of up to 2.5 mJ are achievable. Experimental optimization and characterization of 4 nC electron beams for the SASE FEL option were performed at PITZ. Parameters of the beam, including slice emittance, slice energy spread, and current distribution, were measured. FEL simulations based on measured beam parameters show that the FEL pulse energies are in the sub-mJ level.

S2E simulations of the THz radiation generated by CTR and CDR were performed. By using a short Gaussian photocathode laser pulse and an electron bunch compressed by velocity bunching with bunch charge up to 1 nC, CTR and CDR pulse energies up to 4 μJ and frequencies covering up to 0.4 THz are achievable. Corresponding experimental generations of CTR and CDR were performed successfully. Average pulse energies of up to 1.85 μJ and coherent frequencies of up to 1.5 THz were measured. Furthermore, S2E simulations and corresponding experiments of the THz radiation generated by using a comb beam were performed. Several narrow-band peaks at higher-order harmonics were observed in the spectral distributions.

Zusammenfassung

Der europäische Röntgenlaser (engl. European X-ray Free Electron Laser, E-XFEL) wurde gebaut, um hochbrillante, ultrakurze Pulse von räumlich kohärentem Röntgenlicht für die Grundlagenforschung bereitzustellen. Einige vorgeschlagene Experimente setzen sowohl die Röntgenpulse der Anlage als auch die Bereitstellung von Pulsen im Terahertzfrequenzbereich (THz) voraus, mit deren Hilfe ein Probenmaterial angeregt wird, bevor es mit dem Röntgenlicht diagnostiziert wird (sog. Pump-probe-Experimente). Ein vielversprechendes Konzept, die benötigten THz-Pulse bereitzustellen, ist eine flexible, beschleunigerbasierte THz-Quelle. Der Photoinjektor Teststand bei DESY in Zeuthen (PITZ) könnte als Prototyp für die Entwicklung einer solchen Quelle dienen. Im Rahmen dieser Arbeit wurde untersucht, inwieweit PITZ dazu geeignet ist. Drei Möglichkeiten zur Erzeugung von THz-Strahlung mit den Elektronenstrahlen von PITZ wurden dafür untersucht: (i) selbstverstärkende spontane Emission in einem Freie-Elektronen Laser (engl. self-amplified spontaneous emission free-electron laser, SASE FEL), (ii) kohärente Übergangsstrahlung (engl. coherent transition radiation, CTR) und (iii) kohärente Beugungsstrahlung (engl. coherent diffraction radiation, CDR).

Die Studien zum THz SASE FEL Aufbau wurden unter Annahme von Elektronenpaketen mit 4 nC Ladung, die in einem Undulator vom Typ APPLE-II mit einer Periodenlänge von 40 mm in helikaler Anordnung strahlen, durchgeführt. Simulationen von der Elektronenquelle bis zum Ende des gesamten Aufbaus (engl. Start-to-end, S2E) ergaben, dass bei 100 μm und 20 μm THz-Wellenlänge Pulsenergien von bis zu 2.5 mJ erreicht werden können. Elektronenpakete mit 4 nC Ladung wurden daraufhin auch experimentell bei PITZ untersucht. Ihre Eigenschaften, unter anderem die Emittanz entlang des Pakets (engl. Slice emittance), die Breite des Teilchenenergiespektrums entlang des Pakets (engl. Slice energy spread) und der Stromverlauf im Elektronenpaket wurden vermessen und optimiert. FEL-Simulationen mit den experimentell erreichten Strahlparametern zeigen erreichbare THz-Pulsenergien im Bereich von einigen 100 μJ.

Weiterhin wurden S2E-Simulationen für die THz-Erzeugung mittels CDR und CTR durchgeführt. Mit einem kurzen, Gauss-förmigen Photokathodenlaserpuls und Kompression der damit erzeugten Elektronenpakete mittels eines Geschwindigkeitsunterschieds der Elektronen entlang des Pakets konnten bei einer Gesamtladung des Elektronenpakets von 1 nC THz-Pulse mit bis zu 4 μJ Gesamtenergie bei einer Frequenz von bis zu 0.4 THz

erreicht werden. Bei den entsprechenden Experimenten wurden THz-Pulse mit bis zu 1.85 μJ Pulsenergie und einer kohärenten Frequenz bis zu 1.5 THz gemessen. Schließlich wurde die Erzeugung von THz-Strahlung mittels Pulszügen aus mehreren Elektronenpaketen in S2E-Simulationen und experimentell untersucht. Mehrere schmalbandige Maxima bei höheren harmonischen Vielfachen der Grundfrequenz konnten dabei im Spektrum der erzeugten THz-Strahlung beobachtet werden.

Contents

Chapter 1

Introduction

Electromagnetic radiation (EMR) is a tool to visualize nature. It can be described by its frequency or wavelength. A chart that shows the range of frequencies of EMR and their respective wavelengths, so-called the EMR spectrum, from radio frequency to gamma-ray is illustrated in Fig. 1.1.

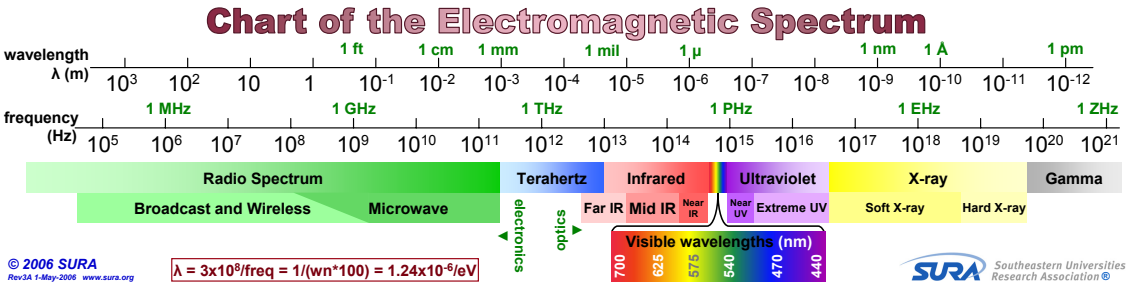

Figure 1.1: Chart of spectrum of electromagnetic radiation (EMR) [1]

In research of the composition and structure of matter, the wavelengths of the EMR determine the spatial scale of the measurements. By using the EMR with short pulses, it is possible to study dynamics processes at the temporal resolution, which is comparable to the pulse duration of the EMR. The European X-ray Free-Electron Laser (XFEL) facility was built to generate high brilliant, ultra-short pulses of spatial coherent X-rays and use them for scientific researches [2]. Some properties of the generated x-ray pulses are listed in Table 1.1. With these properties, the x-ray pulses can be used to film ultra-fast phenomena of matter on the atomic scale [3]. Furthermore, such high peak brilliance makes them a unique tool for exploring not only crystalline structures but also non-crystalline structures [4].

Table 1.1: Some parameters of the generated x-ray pulses from the European XFEL [3]

Parameter	**Value**	**Unit**
Pulse per second	27 000	pulse
Wavelength	0.05 to 4.7	nm
Pulse duration	< 100	fs
Peak brilliance	5×10^{33}	photons / s / mm^2 / mrad^2 / 0.1%BW

In Fig. 1.1, the electromagnetic spectrum that covers the frequency range of 0.1 to 10 THz, or the wavelength range of 3 mm to 30 µm, is a combination of Terahertz and Far Infrared bands. Generally, both bands are called together as the terahertz (THz) spectrum. EMR with THz frequencies (THz radiation) is widely used in many branches of scientific research and applications [5]. Science and technology concerning THz radiation have become one of the most exciting research fields. Their related publications have increased exponentially for decades [6]. In spectroscopy, THz radiation is an efficient tool for non-destructive spectroscopy such as low-energy excitations in electronic materials, low-frequency vibrational modes of condensed phase media, and vibrational and rotational transitions in molecules [7]. By using THz radiation with short pulse duration, it allows time-resolved measurements of the interactions, so-called THz time-domain spectroscopy [8].

An advanced technique of time-domain spectroscopy is to use the first EMR pulse to ”pump” the matter to its excited state, then use the second EMR pulse whose time delay with respect to the first pulse is controllable to ”probe” the excited matter. This technique is often referred to as pump-probe spectroscopy or pump-probe experiment [8]. By using THz pulses as the pump pulses and using femtosecond x-ray pulses as the probe pulses, one can film ultra-fast phenomena of the matter on the atomic scale during its excited state.

Several x-ray FEL facilities, such as LCLS and PSI, have planned to perform pump-probe experiments by using their x-ray pulses and THz pulses [9–11]. The European XFEL realizes many research opportunities by pump-probe experiments and organized a workshop called Terahertz Science at European XFEL in 2017 to collect feedback about the research opportunities and overview of the THz sources [12]. Requirements of an ideal THz source summarized from the workshop are

- Tunable temporal pulse shape from single-cycle pulse multi-cycle pulse
- Tunable frequency from 0.1 to 30 THz (wavelength of 3 mm to 10 µm)
- Minimum pulse energy of 10 µJ at all frequencies
- Options for stable or non-stable carrier-envelope phase (CEP)
- Repetition rate of at least 0.1 MHz to ideally 4.5 MHz

- Temporal jitter must be better than 0.1/frequency, e.g., $<$100 fs at 1 THz, $<$20 fs at 5 THz, and $<$10 fs at 10 THz.

Conventional laser-based THz sources have been planned to be implemented at the European XFEL based on the existing optical pump-probe laser [13]. The laser-based sources can generate THz pulse with unprecedented peak power for narrow spectral ranges. However, the average power, pulse repetition rate, and frequency tuning range of such sources are limited. Accelerator-based THz sources can overcome these limitations and fulfill all requirements which are listed above.

1.1 Motivations for Development of an Accelerator-based THz Source at PITZ

The Photo Injector Test facility at DESY in Zeuthen (PITZ) has been established to develop, study and optimize high brightness electron sources for modern linac-based short-wavelength Free-Electron Lasers (FELs) like FLASH [14] and the European XFEL. Furthermore, PITZ serves as the facility for commissioning and optimizing RF guns for the European XFEL [15–18]. Therefore, the same characteristics (pulse structure and beam quality) of the electron beam from the RF gun at PITZ are available as they are at the European XFEL.

A description of the PITZ accelerator is given here (More details are explained later in Chapter 3). PITZ consists of two RF accelerating sections; an RF photoelectron gun (referred shortly as an RF gun) and an RF linear accelerator called CDS booster. Electrons are generated by photoelectric emission from a photocathode inside the RF gun using external laser pulses, then accelerated by the RF gun and the CDS booster. General parameters of an electron bunch at PITZ are following; bunch charge up to 4 nC, bunch duration of 1 to 30 ps and mean momentum up to 22 MeV/c.

A way to meet the essential requirements for the THz source is generating the THz pulses from the same type of electron source which serves the European XFEL and therefore can provide the same time structure and repetition rate as those of the X-ray pulses. Obviously, an ideal setup for the THz source is one similar to the PITZ accelerator. Moreover, a PITZ-like setup is small enough to fit in or to be placed close to the infrastructure of the user facility at the European XFEL so that the transport of the THz pulse to the user experiments is relatively short.

The concept of generating IR/THz radiation by electron bunches from a linear accelerator for pump and probe experiments at the European XFEL was originally proposed in [19]. The reference shows estimations of properties of IR/THz radiation generated from a radiation source based on an electron accelerator similar to the PITZ facility. By using the mechanism of Self-amplified spontaneous emission (SASE) FEL, radiation with the wavelength of 100 µm, pulse energy of millijoule level and spectrum bandwidth of

about 2-3 % can be generated. The reference also suggests that different means for radiation generation such as edge radiation, transition radiation, coherent radiation of tailored or pre-modulated beams can be used. With the current techniques for the production of electron beam at PITZ and the different options for radiation generation, it will be possible to cover wavelengths in the whole radiation spectrum from IR (µm) to THz (µm - mm) wavelengths with a variety of field patterns, and with a high level of radiation pulse energy.

A prototype facility of the accelerator-based THz source with a PITZ-like setup is needed in order to demonstrate that such a source can practically meet all requirements of the THz source. PITZ can be considered as an ideal machine for the prototype. Furthermore, since PITZ is a photoinjector test facility, the accelerator and also the beam-time are adaptable to new developments.

The aim of this thesis is to investigate the capabilities of THz production at the PITZ facility. The results from this thesis can be used as a benchmark for the development of accelerator-based THz sources for pump and probe experiments at the European XFEL.

1.2 Overview of Thesis

This chapter introduces the background, importance, and motivation of the thesis. In Chapter 2, an overview of optical laser-based and accelerator-based THz sources is given. Then, pulse energies from various types of accelerator-based THz sources based on PITZ electron beam parameters are evaluated. Finally, a comparison of the characteristics of the radiations from a PITZ-like with other IR/THz light sources will be presented. Chapter 3 gives a description of the PITZ facility including details of its photocathode laser system, accelerating cavities and electron beam diagnostics systems.

In Chapter 4, details about Start-to-End (S2E) simulations of the IR/THz source based on the PITZ accelerator are presented and discussed. The simulations were focused on the radiation generation with two options: (i) Self-Amplification of Spontaneous Emission Free-Electron Lasers (SASE FELs) and (ii) Coherent Transition Radiation (CTR) and Coherent Diffraction Radiation (CDR).

Details and results of experimental characterization and optimization of the electron beams for the THz SASE FEL option are presented and discussed in Chapter 5, together with FEL simulation results based on the measured beam parameters.

Chapter 6 describes the first experimental measurements of CTR and CDR at PITZ. Details about the CTR/CDR station are presented. Then, the experimental setup, as well as the first characterization results of CTR and CDR generations at PITZ, are presented and discussed.

Chapter 7 is dedicated to discussions on conclusion and outlook of this thesis. The ideas and plans to continue the studies of the THz options at PITZ will be presented.

In appendix A, a summary of formulas of transportation matrices and electron beam

parameters is given. In appendix B, Calculations of THz SASE FEL based on an LCLS-I undulator and PITZ accelerator are presented.

Chapter 2

Overview of Modern THz Radiation Sources

As introduced in Chapter 1, intense THz radiation in pulse-mode with an ultra-short duration (picosecond to femtosecond) and with a pulse energy of at least in micro-Joule level is generally required for THz time-domain spectroscopy [20]. Two categories of EMR sources are generally used to generate such intense THz pulse: laser-based sources and accelerator-based sources [12]. This chapter gives an overview of various THz radiation sources, including thermal, laser-based, and accelerator-based radiation sources.

An overview diagram that classifies the THz radiation sources into various categories based on their mechanisms is shown in Fig. 2.1 and will be discussed in the next sections. Then, THz radiation generation using various accelerator-based methods based on PITZ electron beam parameters are evaluated by calculations. Next, an overview of the characteristics of THz radiation from the various sources is given and compared. Finally, concluding remarks are given in the last section.

2.1 Thermal Radiation Sources

Thermal radiation is electromagnetic radiation emitted from matter when it is at a temperature above absolute zero (0 K). The simplest case of thermal radiation is blackbody radiation that can be theoretically explained by Planck's radiation law [21]. Blackbody radiation has a broadband spectrum and its peak wavelength (λ_{max}) is temperature dependent which can be simply calculated by the Wien's displacement law, $\lambda_{\mathrm{max}} T = 2.898 \times 10^{-3}$ m $\cdot$ K. Peak wavelengths in the THz frequency range (3 mm to 30 µm) correspond to a blackbody temperature range of about 1 to 100 K.

Natural extraterrestrial thermal radiation sources consist of cosmic background radiation [22] and stars like the sun. Laboratory sources of thermal radiation include the mercury-vapor lamp [23] and the globar which is a silicon carbide rod electrically heated

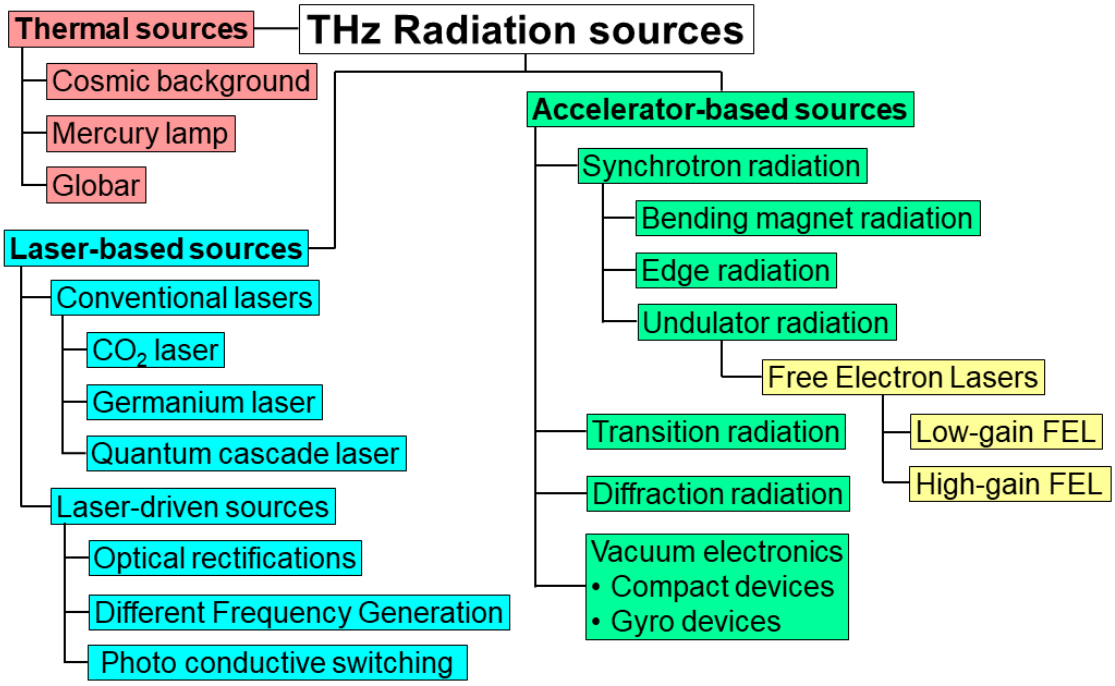

Figure 2.1: Overview diagram of THz radiation sources.

to high temperatures (> 1000 K). Both sources generate continuous-wave radiation with a broadband spectrum. They are common budget radiation sources for Fourier Transform Infrared (FTIR) spectroscopy [24].

Generally, the thermal radiation sources are continuous, incoherent, and have low radiation intensity. Therefore, they are not applicable for THz time-domain spectroscopy.

2.2 Laser-based THz Sources

Laser devices use the principle of stimulated emission to generate coherent electromagnetic radiation. Laser-based THz sources are categorized into two groups: conventional lasers and laser-driven sources.

2.2.1 Conventional Lasers

A laser device which electrons of its laser-active medium are still bound to atomic, molecular or solid-state quantum energy levels during the stimulated emission process is categorized as a conventional laser [25]. Electromagnetic radiation generated by the conventional lasers is coherent, monochromatic, collimated, and intense [26]. This section

presents a few examples of conventional lasers that can be used as IR/THz radiation sources.

A **Carbon Dioxide** (CO_2) **Laser** uses a gas mixture of CO_2 and other types of gas as the laser active medium. It emits lasing based on transitions in molecular states of CO_2 with a wavelength range from 9 to 11 µm (33.3-27.3 THz). The average output power is in the range from a few milliwatts to many kilowatts depending on the size of the laser system [27, 28]. CO_2 lasers are widely used in industrial and medical applications. An example of a CO_2 laser is the commercial product model p400 from Synrad [29]. It can generate laser pulses with a maximum pulse energy of 1 J at 100 Hz pulse repetition rate at the wavelength of 10.6 µm.

A **Germanium Laser** or a p-Ge laser is a semiconductor laser (also called laser diode) where the laser active medium is made of germanium. Recent development of the p-Ge laser [30] demonstrated generation of THz radiation pulses with frequency tunable in the range of 1.2 - 2.8 THz and average power of 10 mW. A cooling system is required for the operational temperature of 4.2 K.

A **Quantum Cascade Laser** (QCL) is a special kind of semiconductor laser. It uses periodic structure material layers (superlattice) as the laser active medium. This type of materials allows intersubband transitions, leading QCLs to have a wide tunable range of emission wavelength, which can be determined by the design of the superlattice [31]. The recent development of THz QCL [32] experimentally demonstrated the production of THz radiation pulses with output peak power in the watt-level at the frequency of ∼3.4 THz. The operational temperature is at 10 K. Therefore a cooling system is also required.

2.2.2 Laser-driven Sources

Optical Rectification using Lithium Niobate and Organic Crystals

When a laser beam passes through a nonlinear crystal, the electric field of the laser induces a second-order polarization in the nonlinear crystal. The frequency of the input laser beam is rectified by the induced polarization, resulting in an output laser beam with a lower frequency. This process is called optical rectification (OR) [33]. THz radiation based on the OR technique using lithium niobate ($LiNbO_3$) [34] and organic crystals [35] were experimentally demonstrated. The radiation has a broadband frequency with a maximum pulse energy of a few hundreds µJ at a repetition rate of 10 Hz. Demonstration of OR in laser-induced gas plasma was also demonstrated in [36]. The pulse energy is below 1 µJ with a repetition rate of 1 kHz.

Difference Frequency Generation

The configuration of Difference Frequency Generation (DFG) is similar to OR but with two input laser beams. Both laser beams, with a frequency difference of a few THz, interact through a nonlinear crystal inducing the polarization to oscillate. The polarization oscillates at the sum and difference frequencies which the latter one being the source of a THz laser beam [8]. THz generation based on DFG in the $LiNbO_3$ crystal was experimentally demonstrated [37]. The frequency of the output THz pulses is tunable between 10 and 72 THz with maximum pulse energy up to 19 μJ. DFG using an organic nonlinear crystal was experimentally demonstrated in [38]. The output laser is tunable between 4 and 18 THz with pulse energy of 1.9 μJ.

Photoconductive Switch

A photoconductive switch or photoconductive emitter is made of a photoconductive semiconductor substrate attached to metal electrodes. When the substrate absorbs the pump laser pulses, electron-hole pairs are produced and then accelerated by a bias voltage from the electrodes and radiate electromagnetic radiation. By using the pump pulse with a short pulse duration of sub-ps, the generated output pulse is as short as the pump pulse and its Fourier transformation is a broadband spectrum covering the THz frequency range. Generation of THz pulse using a photoconductive switch was demonstrated in [39]. The THz pulse has pulse energy of about 6 nJ with a repetition rate of 250 kHz.

2.3 Accelerator-Based THz Sources

A simple accelerator-based radiation source consists of an electron beam source and a radiator. The electron beam is generated and accelerated by an electron gun and then in some cases is accelerated again to higher energy by an electron accelerator. Finally, the electron beam is injected into the radiator and emits the radiation. The radiators can be an area with electric or magnetic fields, a boundary between two media, or an inhomogeneous medium.

When a relativistic electron beam travels through an area with the existence of magnetic fields, the beam is accelerated (or bent) by the magnetic fields and emits synchrotron radiation. A simple radiator for synchrotron radiation is a bending magnet with a uniform magnetic field. This radiation is explicitly called as bending magnet radiation. Since actual dipole magnets have a fringe field on their edges, therefore, the electron beam experiences a rapid change of the magnetic field from a uniform field area to a non-uniform field area (or area without field). The emission spectrum from the dipole edge is modified in a characteristic way called edge radiation [40]. By an arrangement of many short dipole magnets with alternating polarity, the electron beam is bent periodically and emits radiation. The set of arranged magnets is called an undulator, and the emitted radiation is

called undulator radiation [41]. With suitable conditions, the electron beam interacts with the self-emitted radiation during passing through the undulator resulting in amplification of the total output radiation. This process is called Free-Electron Laser (FEL) [25].

When the electron beam travels through a boundary between two media with different dielectric constants, it emits transition radiation. The diffraction radiation is emitted when the electron beam travels in the neighborhood of an inhomogeneous medium [42]. Radiators of diffraction radiation can be an aperture in a metallic plate [43], a diffraction grating [44], or a corrugated pipe [45].

This section gives a brief review of some methods of THz radiation generation based on electron accelerators including the bending magnet radiation, edge radiation, undulator radiation, Free-electron lasers (FELs), transition and diffraction radiation. In the end, an overview of THz vacuum electronic devices is given.

2.3.1 Bending Magnet Radiation

When a relativistic electron moves in curved trajectories the bending magnet radiation is generated. Assuming an electron moving under the influence of uniform dipole fields with the bending radius R, the spectral intensity of the emitted radiation can be described by [40]

$$\frac{\mathrm{d}^2 I}{\mathrm{d}\Omega \mathrm{d}\omega} = \frac{3e^2\gamma^2}{16\pi^3\varepsilon_0 c}\left(\frac{\omega}{\omega_c}\right)^2 (1+\gamma^2\theta^2)^2\left[K_{2/3}^2(\xi)+\frac{\gamma^2\theta^2}{1+\gamma^2\theta^2}K_{1/3}^2(\xi)\right], \tag{2.1}$$

where I is the radiation intensity, Ω is the solid angle from the radiation source, ω is the radiation frequency, e is the charge of an electron, γ is the Lorentz factor of the electron, ε_0 is the electrical constant, c is the speed of light in vacuum, $\omega_c = 3\gamma^3 c/2R$ denotes the critical frequency that divides the spectrum in two halves of equal integrated intensity, θ is the observation angle of the radiation, $K_{1/3}$ and $K_{2/3}$ are modified Bessel functions and $\xi \equiv \omega(1+\gamma^2\theta^2)^{3/2}/2\omega_c$.

The generated radiation is mostly concentrated into a small cone with an observation angle of $\sim 1/\gamma$ towards the direction of motion of the bunch, where γ is the Lorentz factor of the electron bunch.

For the emission from an electron bunch, the emitted radiation is obtained by the superposition of the radiation fields from each electron within the bunch. For a relativistic electron bunch, when the wavelength of the emitted radiation is longer than or comparable to the electron bunch length, the radiation waves add up in phase, leading to temporal coherence of the radiation. By neglecting the transverse distribution, the spectral intensity of an electron bunch becomes [40]

$$\frac{\mathrm{d}I}{\mathrm{d}\omega} = N_e\frac{\mathrm{d}I_0}{\mathrm{d}\omega} + N_e(N_e-1)F_\ell(\omega)\frac{\mathrm{d}I_0}{\mathrm{d}\omega}, \tag{2.2}$$

where

$$F_\ell(\omega) = \left| \int_{-\infty}^{+\infty} \rho_\ell(z) \exp(-i\omega z) \mathrm{d}z \right|^2 \tag{2.3}$$

is the longitudinal form factor of the electron bunch, $\rho_\ell(z)$ is a function that describes the longitudinal distribution of the electron bunch, N_e is the number of electrons in the bunch, $\frac{\mathrm{d}I}{\mathrm{d}\omega}$ is the total radiation of the electron bunch and $\frac{\mathrm{d}I_0}{\mathrm{d}\omega}$ is the radiation of a single electron. The first term on the right side of Eq. (2.2) expresses the incoherent radiation which is proportional to N_e while the second term expresses the coherent radiation which is proportional to N_e^2 .

2.3.2 Edge Radiation

Edge radiation (ER) can be observed when radiation wavelengths are longer compare to the dimension of the fringe field. By assuming the size of the fringe field region is zero, the spectral intensity in the far-field can be calculated by [40]

$$\frac{\mathrm{d}^2 I}{\mathrm{d}\Omega \mathrm{d}\omega} = \frac{e^2}{16\pi^3 \varepsilon_0 c} \frac{\beta^2 \sin^2\theta}{(1-\beta\cos\theta)^2}, \tag{2.4}$$

where $\beta = v/c$ is the electron speed in units of c, and θ is the observation angle of the radiation. The spatial distribution is ringlike with a peak intensity at the observation angle of $\sim 1/\gamma$. When the distance of the observer to the edge is less than $\lambda\gamma^2$, a near-field edge radiation can be observed and its spectral intensity can be calculated by [40]

$$\frac{\mathrm{d}^2 I}{\mathrm{d}\Omega \mathrm{d}\omega} = \frac{e^2}{\pi^3 \varepsilon_0 c} \frac{\sin(r\omega\theta^2/4c)}{\theta^2}, \tag{2.5}$$

The spatial distribution of the near-field case is still ringlike with a maximum intensity at $\theta \sim 1/\sqrt{c/\pi\omega r}$. Note that the far-field spectral intensity in Eq. (2.4) is independent of frequency while the near-field spectral intensity in Eq. (2.5) depends on frequency.

In case of a straight section of length L with two bending magnets at its ends, the observed radiation is usually the superposition of ER from from the entrance and the exit edges. By assuming the zero-edge model, the spectral intensity in the far-field can be expressed as [40]

$$\frac{\mathrm{d}^2 I}{\mathrm{d}\Omega \mathrm{d}\omega} = 4\sin^2\left[\frac{\omega L}{4c\gamma^2}(1+\gamma^2\theta^2)\right] \cdot \left[\frac{e^2}{16\pi^3\varepsilon_0 c} \frac{\beta^2\sin^2\theta}{(1-\beta\cos\theta)^2}\right], \tag{2.6}$$

The edge radiation is cylindrical symmetric with radial polarization [40, 46]. The spectral intensity from an electron bunch can also be calculated by using Eq. (2.2).

2.3.3 Undulator Radiation

An undulator magnet is a long periodic arrangement of many short dipole magnets with alternating polarity producing a periodic magnetic field along the undulator with a period length of λ_u. There are two basic types of undulator magnet based on their transverse magnetic field components; the planar undulator with transverse magnetic fields existing only in one axis (vertical or horizontal) and the helical undulator where transverse magnetic fields exist in both vertical and horizontal axes. The undulator parameter K of an undulator magnet can be calculated by [25]

$$K = \frac{eB_0\lambda_u}{2\pi m_e c}, \tag{2.7}$$

where B_0 is the peak magnetic field of the undulator, and m_e is the electron rest mass.

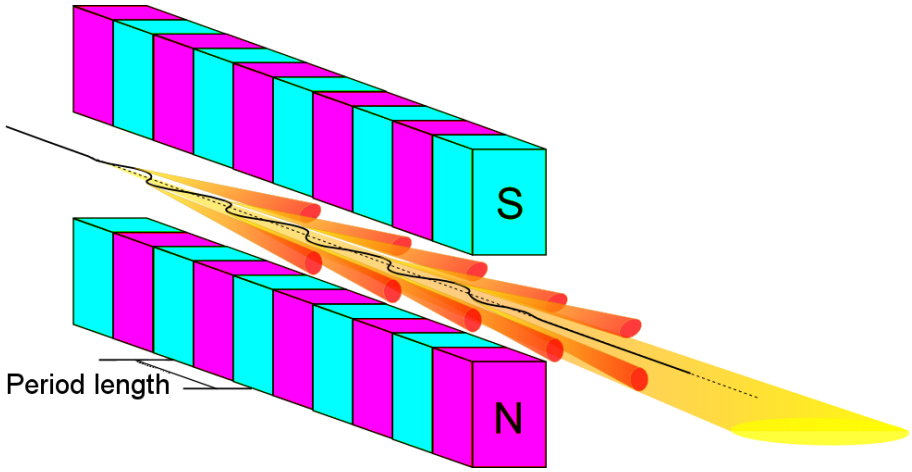

Figure 2.2: Configuration of undulator radiation.

Figure 2.2 illustrates electron motion in a planar undulator and emission of the undulator radiation. When the electron travels through the undulator, the transverse motion of the electron is periodically oscillating by the influence of the magnetic field and it emits radiation. The emitted radiation waves overlap with each other and so interference effects occur. The interference of undulator radiation is constructive at some wavelengths while it is destructive at other wavelengths leading to the appearance of a harmonics spectrum [41, p.1]. The wavelength of the mth harmonics (λ_m) of the undulator radiation in forward direction is [25, p.21,60]

$$\lambda_m = \frac{1}{m}\frac{\lambda_u}{2\gamma^2}\left(1 + K_{RMS}^2\right), \quad m = 1,\ 3,\ 5, \ldots \quad . \tag{2.8}$$

whrer γ is the Lorentz factor of the electron. Note that $K_{RMS} = K$ for the helical undulator and $K_{RMS} = K/\sqrt{2}$ for the planar undulator. This equation shows that the radiation wave-

length can be tuned by varying the undulator period length, the electron beam momentum, and the undulator parameter.

For undulator radiation from a planar undulator, the spectral energy density per electron of the radiation emitted in the forward direction for the mth harmonics is [25, p.22]

$$\left.\frac{\mathrm{d}^2 I}{\mathrm{d}\Omega \mathrm{d}\omega}\right|_{\text{undulator}} = \frac{e^2\gamma^2 m^2 K^2}{4\pi\varepsilon_0 c(1+K^2/2)^2} \cdot \frac{\sin^2(\pi N_u(\omega-\omega_m)/\omega_1)}{\sin^2(\pi(\omega-\omega_m)/\omega_1)} \cdot |JJ|^2 \tag{2.9}$$

where

$$|JJ|^2 = J_n\left(\frac{mK^2}{4+2K^2}\right) - J_{n+1}\left(\frac{mK^2}{4+2K^2}\right), \quad m = 2n+1, \tag{2.10}$$

ω_m is the angular frequency of the mth harmonic, J_n are the Bessel functions of integer order ($n = 0,\ 1,\ 2, \ldots$), K is the undulator parameter, N_u is the number of periods of the undulator.

The observation angle of the undulator radiation cone is narrower than those of the bending magnet and edge radiations by a factor of $\sqrt{N_u}$. By observing on-axis of the planar undulator, the first-harmonic radiation is linearly polarized in the same axis as the electron oscillation plane [41]. The spectral intensity from an electron bunch can be calculated by Eq. (2.2) as well.

2.3.4 Free electron laser (FEL)

Similar to the undulator radiation, the FEL process happens when an electron beam travels through an undulator. However, the FEL process has a feedback mechanism to the electron beam. An FEL can be operated either with setups of a low-gain FEL and a high-gain FEL. Configurations of both setups are shown in Fig. 2.3.

Low-gain FEL

The FEL oscillator as shown in Fig. 2.3 (top) consists of an undulator and an optical cavity. When the electron beam travels through the undulator, the spontaneous radiation is emitted. The optical cavity is set up around the undulator in order to reflect the radiation back into the undulator. The reflected-back radiation can enable the lasing process if of each radiation round-trip a further electron bunch is arriving synchronously, thus overlapping with the radiation inside the undulator field. After each passage, the radiation intensity is slightly increased by a few percents. However, with a sufficient number of turns, the output radiation power can be very high, even reaching gigawatts level at saturation [25].

Qualitative treatment for the low-gain FEL is described in Ref. [25]. An electron beam with a bunch length much longer than the fundamental wavelength is assumed to propagate through the undulator together with a plane electromagnetic wave with an

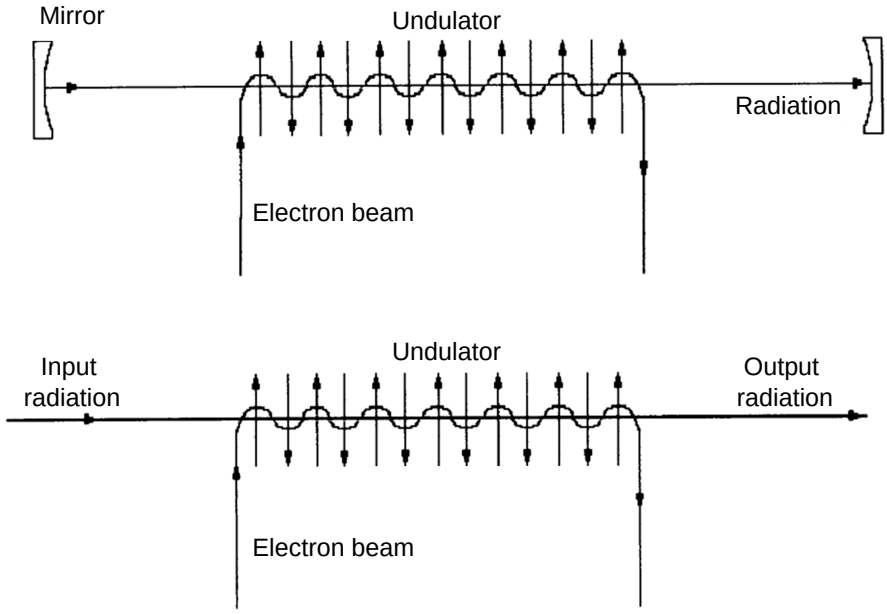

Figure 2.3: Configurations of a low-gain FEL or an FEL oscillator (top) and a high-gain FEL (bottom).

electric field amplitude of E_0. The FEL gain function G is defined as the relative growth of the radiation intensity during one passage through the undulator $G = \Delta I_\ell / I_\ell$ with $I_\ell = c\varepsilon_0 E^2/2$. This gain function can be expressed by

$$G(\eta) = -\frac{\pi e^2 \hat{K} N_U^2 \lambda_u^2 N_e}{4\varepsilon_0 m_e c^2 \gamma_r^3} \frac{d}{d\xi}\left(\frac{\sin^2 \xi}{\xi}\right), \text{with} \tag{2.11}$$

$$\xi = 2\pi N_u \left(\frac{\gamma - \gamma_r}{\gamma_r}\right), \tag{2.12}$$

where N_u is the number of undulator periods, N_e is the number of electrons per unit volume, γ is the Lorentz factor of the electron, γ_r is the Lorentz factor of the resonance condition and $\hat{K}$ is a modified undulator parameter

$$\hat{K} = K\left[J_0\left(\frac{K^2}{4+2K^2}\right) - J_1\left(\frac{K^2}{4+2K^2}\right)\right]. \tag{2.13}$$

The optical cavity length must be equal to the spacing between electron bunches in order to make the optical pulses overlap with the electron bunches. However, the spacing between electron bunches at the European XFEL is about 222 ns (4.5 MHz operation).

This condition leads to a cavity length of about 66.67 m which is not practical for the IR/THz FEL oscillator, especially since each of the x-ray pulses should have its corresponding THz pulse.

High-gain FEL

The setup of a high-gain FEL is shown in Fig. 2.3 (bottom). The electron beam travels through the undulator with a sinusoidal trajectory. The input radiation (seeding) propagates colinear with the electron beam and then interacts with it. Some electrons that lose energy travel on a sinusoidal trajectory with a larger amplitude than other electrons that gain energy. This process results in a modulation of the longitudinal velocity which leads to the concentration of electrons in slices with a period of the fundamental wavelength, known as the so-called microbunching process. Since the length of each microbunch (each slice) is equal to or shorter than the fundamental wavelength, the radiation is emitted coherently from each slice [25].

The theory of the high-gain FEL developed in Ref. [47] presents methods to calculate the FEL parameters. For the case of an electron beam which has Gaussian distributions in transverse phase space and energy spread, the gain parameter (Γ) for the high-gain FEL with a helical undulator is defined as [47]

$$\Gamma = \left[\frac{I_0 \omega^2 \theta_s^2}{I_A c^2 \gamma_z^2 \gamma}\right]^{1/2} \quad , \tag{2.14}$$

where I_0 is the beam current, ω is angular frequency of the FEL wavelength, θ_s is an angle of electron rotation in a helical undulator, $I_A \simeq 17\,\mathrm{kA}$ is the Alfven current, γ_z is the longitudinal relativistic factor in a helical undulator and γ is the relativistic factor. From Γ, the gain length (L_g) can be calculated from the following relation

$$L_g = \Gamma^{-1} \quad , \tag{2.15}$$

and the efficiency parameter ρ of the high-gain FEL [47] can be calculated by

$$\rho = \frac{c\gamma_z^2 \Gamma}{\omega} \quad . \tag{2.16}$$

The gain length and the efficiency parameter relate to the FEL efficiency. For the high-gain FEL, the undulator length (L_U) is required to be much longer than the gain length $(L_U \gg L_g)$ and the efficiency parameter is required to be much smaller than 1 $(\rho \ll 1)$.

Some important physical effects can be included in the FEL calculation via the dimensionless FEL parameters which define the power of the effects. For the high-gain FEL with an axisymmetric electron beam, these dimensionless parameters are [47]:

- The diffraction parameter (B)

$$B = \Gamma \frac{2\sigma^2 \omega}{c} \quad , \tag{2.17}$$

  where σ is the transverse RMS size of the electron beam

- The space charge parameter $\hat{\Lambda}_{\mathrm{p}}$

$$\hat{\Lambda}_{\mathrm{p}}^2 = \frac{2c^2}{\theta_s^2 \sigma_z^2 \omega^2} \quad , \tag{2.18}$$

- The energy spread parameter $(\hat{\Lambda}_{\mathrm{T}})$

$$\hat{\Lambda}_{\mathrm{T}}^2 = \frac{\left\langle (\Delta E)^2 \right\rangle}{\left(E_0^2 \rho^2\right)} \quad , \tag{2.19}$$

where σ_z is the RMS bunch length, $\left\langle (\Delta E)^2 \right\rangle$ is the energy spread in the electron bunch and E_0 is the central energy of the electron bunch.

For the case of the high-gain FEL with a planar undulator, the gain parameter, the efficiency parameter, and the dimensionless FEL parameters are redetermined as follow [47]:

$$\Gamma = \left[\frac{A_{JJ}^2 I_0 \omega^2 \theta_\ell^2}{4 I_A c^2 \gamma_\ell^2 \gamma S} \right]^{1/2} \quad , \tag{2.20}$$

$$\rho = \frac{c \gamma_\ell^2 \Gamma}{\omega} \quad , \tag{2.21}$$

$$B = \Gamma \frac{r_0^2 \omega}{c} \quad , \tag{2.22}$$

$$\hat{\Lambda}_{\mathrm{p}}^2 = \left(\frac{8c^2}{\omega^2 r_0^2 \theta_\ell^2 A_{JJ}^2} \right) \quad , \tag{2.23}$$

$$\hat{\Lambda}_{\mathrm{T}}^2 = \frac{\Lambda_{\mathrm{T}}^2}{\Gamma^2} = \frac{\left\langle (\Delta E)^2 \right\rangle}{\left(E_0^2 \rho^2\right)} \quad , \tag{2.24}$$

where A_{JJ} is a factor specifying the interaction of an electron with the EM field in a planar undulator, θ_ℓ is the maximal angle of electron oscillation in a planar undulator, γ_ℓ is the longitudinal relativistic factor in a planar undulator, S is the transverse area of the electron beam, and r_0 is the radius of the electron beam.

Since the electron bunch travels slower than the emitted FEL radiation, the FEL radiation moves away from the bunch head. The magnitude of the radiation part that slips away from the bunch will remain steady because it is not overlapping with the electron bunch, therefore, no FEL gain. The effect of this process is called slippage effect. Slippage effects prevent to use the steady-state approach in the FEL theory and require to include the time-domain of the FEL process in the analysis. However, the slippage effects can be neglected when the following condition is fulfilled

$$\rho \omega T \gg 1 \quad , \tag{2.25}$$

where T is the bunch duration.

Another important issue is the waveguide effect. For the high-gain FEL operating in the IR and THz wavelength ranges, the size of the vacuum chamber is comparable to the radiation wavelength. Therefore, the vacuum chamber could act as a waveguide and has an influence on the FEL amplification process. For a circular waveguide with radius R, effects of the waveguide on the FEL process can be represented by the waveguide diffraction parameter Ω [47]:

$$\Omega = \frac{\Gamma \omega R^2}{c} \quad . \tag{2.26}$$

The power gain of the high-gain FEL G is defined as the ratio between the output power W_{out} and the external input power W_{ext}:

$$G = \frac{W_{\text{out}}}{W_{\text{ext}}} \quad . \tag{2.27}$$

When the undulator length is long enough, the FEL power gain grows exponentially as a function of the undulator length ($G \propto \exp(z_u)$). The exponential growth continues until the electron beam is completely bunched and starts to overmodulate. At this point, the power gain reaches its saturation.

The high gain FEL amplification process still exists without the external seed laser. Current density fluctuations in the electron beam, which exists in the electron beam due to the effect of shot noise, serve as the input signal in the amplification process. This high-gain FEL process is called *Self Amplified Spontaneous Emission (SASE) FEL* [47]. Since the SASE FEL starts from shot noise, it exhibits significant shot-to-shot fluctuations in pulse energy and spectrum. A way to overcome this problem is to use seeding options [25].

Reference [47] presents methods to calculate the FEL characteristics analytically. The effects of the dimensionless FEL parameters are taken into account. However, many ideal conditions are assumed, and many approximations are used. Moreover, including more conditions into the analysis introduces more complicated mathematical problems. Therefore, numerical simulation codes such as GENESIS [48], FAST [49], MINERVA [50], or SIMPLEX [51] have been used to assess complicated FEL processes.

2.3.5 Transition Radiation

Transition Radiation (TR) occurs whenever an electron passes the boundary between two media with different dielectric constants. Typically, a thin metal plate (foil) is used as a radiator for the TR. Figure 2.4a illustrates an electron arriving at a TR radiator in a direction normal to the radiator plane which then emits transition radiation in backward and forward directions. Analytical treatments of TR based on the assumption that the self-field of the electron is converted into real photons by reflection at the radiator surface are presented in Refs. [43, 52]. When the radiator is a perfectly conducting metal disc foil, the spectral intensity of TR in the far-field can be expressed by

$$\left.\frac{\mathrm{d}^2 I}{\mathrm{d}\Omega \mathrm{d}\omega}\right|_{\mathrm{TR}} = \left.\frac{\mathrm{d}^2 I}{\mathrm{d}\Omega \mathrm{d}\omega}\right|_{\mathrm{GF}} \left[1 - T(\omega a/c, \theta)\right]^2 . \tag{2.28}$$

where I is the radiation intensity, ω is the radiation angular frequency, Ω is the solid angle, a is the radius of the radiator, c is the speed of light, θ is the observation angle,

$$\left.\frac{\mathrm{d}^2 I}{\mathrm{d}\Omega \mathrm{d}\omega}\right|_{\mathrm{GF}} = \frac{e^2}{4\pi^3 \varepsilon_0 c} \frac{\beta^2 \sin^2\theta}{(1-\beta^2\cos^2\theta)^2}, \tag{2.29}$$

is the TR spectral intensity from the Ginzburg-Frank formula for an infinite radiator size, β is the ratio between the electron velocity and the speed of light,

$$\begin{aligned} T(\omega a/c, \theta) = & \frac{\omega a}{c\beta\gamma} J_0\left(\frac{\omega a \sin^2\theta}{c}\right) K_1\left(\frac{\omega a}{c\beta\gamma}\right) \\ & + \frac{\omega a}{c\beta^2\gamma^2 \sin\theta} J_1\left(\frac{\omega a \sin^2\theta}{c}\right) K_0\left(\frac{\omega a}{c\beta\gamma}\right). \end{aligned} \tag{2.30}$$

is the correction function for the finite radiator size, J_0, J_1, K_0, and K_1 are Bessel functions. TR is radially polarized and shows a ringlike radiation. Its radiation intensity is peaked at the observation angle of $1/\gamma$ [40]. For TR from an electron bunch, the spectral intensity can also be calculated by using Eq. (2.2).

2.3.6 Diffraction Radiation

Diffraction Radiation (DR) occurs when an electron travels in the neighborhood of an inhomogeneous medium or a border. Figure 2.4b illustrates an electron that arrives at the DR radiator in a direction normal to the radiator plane. The DR radiator is similar to the TR radiator except that it has an aperture in the radiator plane. When the electron passes through this aperture, the DR is emitted in backward and forward directions. Analytical treatments of DR are also presented in Refs. [43, 52]. When an electron passes through a

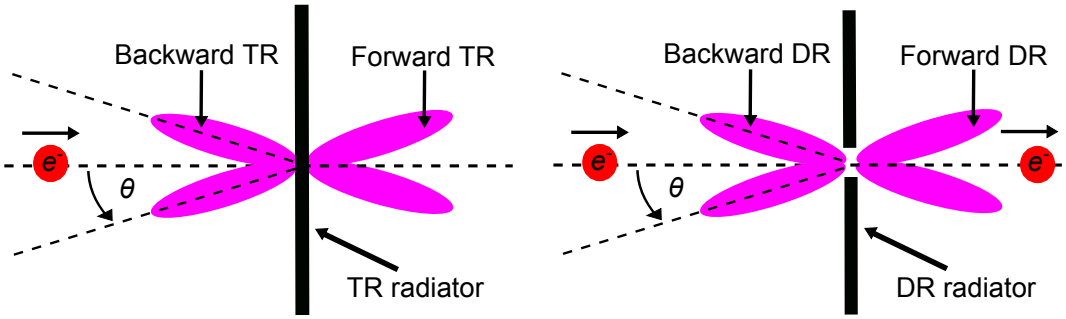

(a) transition radiation (TR) (b) Diffraction radiation (TR)

Figure 2.4: Configurations of (a) transition radiation and (b) diffraction radiation.

circular aperture of radius b on a perfectly conducting disc foil of a radius a as shown in Fig. 2.4b, the spectral intensity of DR in the far-field can be expressed by

$$\left.\frac{\mathrm{d}^2 I}{\mathrm{d}\Omega \mathrm{d}\omega}\right|_{\mathrm{DR}} = \left.\frac{\mathrm{d}^2 I}{\mathrm{d}\Omega \mathrm{d}\omega}\right|_{\mathrm{GF}} \left[T(\omega b/c, \theta) - T(\omega a/c, \theta)\right]^2 . \tag{2.31}$$

Characteristics of DR for this case are quite similar to TR. It is radially polarized and displays a ringlike radiation pattern. The advantage of DR is that the beam is less disturbed when compared with TR.

Not only a metal sheet with an aperture but various devices can also be used as the DR radiators. Another well-known device is a diffraction grating. The radiation is emitted when an electron travels close to the surface of a diffraction grating. This process is called Smith-Purcell Radiation [44]. Another device that becomes interesting recently for THz radiation generation is a pipe with small corrugations [45].

2.3.7 Other Vacuum Electronic Devices

Vacuum Electronics Devices (VEDs) for the generation of THz radiation may be considered as accelerator-based THz sources which are built purposely to use as the *stand-alone* devices for generation of THz radiation. A simple vacuum electronic device consists of an electron source, an interaction circuit, magnets to control electron beam trajectory, an electrons collector, and an output radiation port. It converts input electrical energy into the kinetic energy of the electron beam. Then the kinetic energy is converted into the output radiation by using the interaction circuit [5]. THz VEDs can be categorized as compact devices and gyro device. Their details are described in Ref. [53] and [54], respectively.

2.4 Calculations of THz Sources Based on PITZ Electron Beam Parameters

In order to evaluate the capability of the PITZ accelerator to be used as a accelerator-based THz source, radiation intensities from various methods mentioned in Section 2.3 were calculated based on PITZ electron beam parameters. The calculations were done for two cases: the radiations from a single electron and the radiation from an electron bunch.

For the case of an electron, the electron momentum was assumed to be 22 MeV/c which is close to the maximum beam momentum available at the PITZ accelerator. For the case of an electron bunch, a simulated beam distribution was used as an example beam. It was simulated based on the PITZ accelerator by using the ASTRA program [55]. More details about beam dynamics simulations will be presented later in Chapter 4. This beam has bunch charge of 100 pC, an RMS bunch length of 200 fs FWHM, an RMS transverse size of 0.25 mm and a mean momentum of 22 MeV/c.

For calculation of the bending magnet radiation, the bending radius R was assumed to be 300 mm which is taken from the dipole magnet in the HEDA1 section of the PITZ beamline (see Fig. 3.1).

For calculation of the transition radiation, the radiator size was assumed to be infinite ($a \rightarrow \infty$). For calculation of the diffraction radiation, the radiator was assumed to be an infinite metallic plate with a circular hole with a radius of 1 mm.

For calculation of the FEL radiation, only SASE FEL was considered. A 5 m-long helical undulator with a period length of 40 mm and a 4 nC simulated electron beam were used for the calculation. The Genesis1.3 code [48] was used for simulation of the FEL process and calculation of the output radiation. Details about the FEL simulation will be presented later in Chapter 4, only results of the output radiation are presented here for comparison with other THz radiation sources.

The calculated results of radiation intensity generated by five methods for the case of a single electron are shown in Fig. 2.5. The undulator radiation has the highest spectral intensity at various harmonic frequencies from 5 to 50 THz with narrow-band spectra. The intensity of the bending magnet radiation drops when the frequencies are below 0.1 THz and above 1 THz while the intensity of the edge radiation is constant at all frequencies. The intensities of the transition radiation and diffraction radiation are lowest when compared to the other sources. The intensity of the diffraction radiation significantly drops when the frequencies are above 1 THz.

Figure 2.6 shows the calculation results for the case of an electron bunch. The relative intensity levels from various sources are similar to those for a single electron. The coherent parts cover frequency range up to 0.6 THz. These coherent parts relate to the bunch form factors.

The FEL simulation results, including the energy gain curve, the temporal and spectral profiles of the FEL pulse at the undulator exit are shown in Fig. 2.7. The output FEL

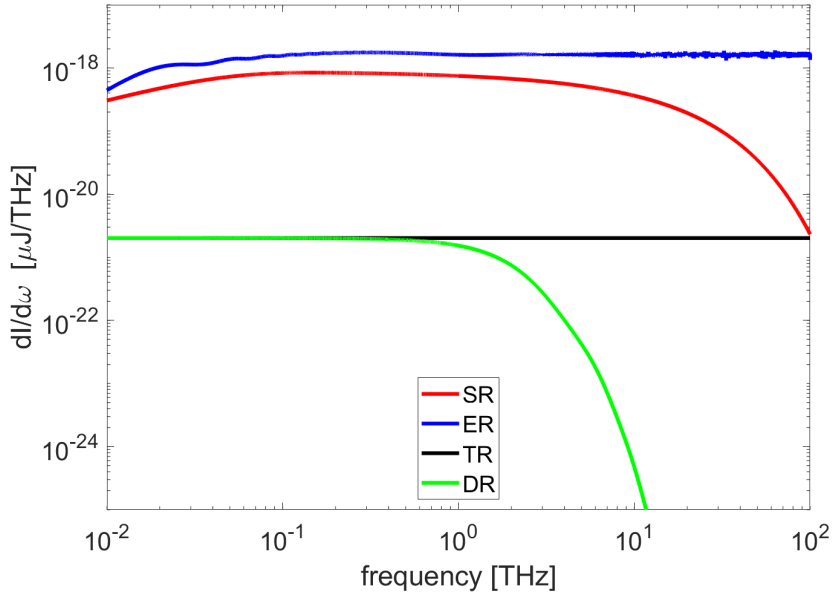

Figure 2.5: Calculated radiation intensity of a single electron as a function of radiation frequency for various accelerator-based THz sources based on PITZ electron beam parameters. Here, SR mean synchrotron radiation, ER means edge radiation, TR means transition radiation, and DR means diffraction radiation.

radiation has pulse energy of 2 mJ, a temporal pulse duration of about 20 ps and a central wavelength of about 100 µm.

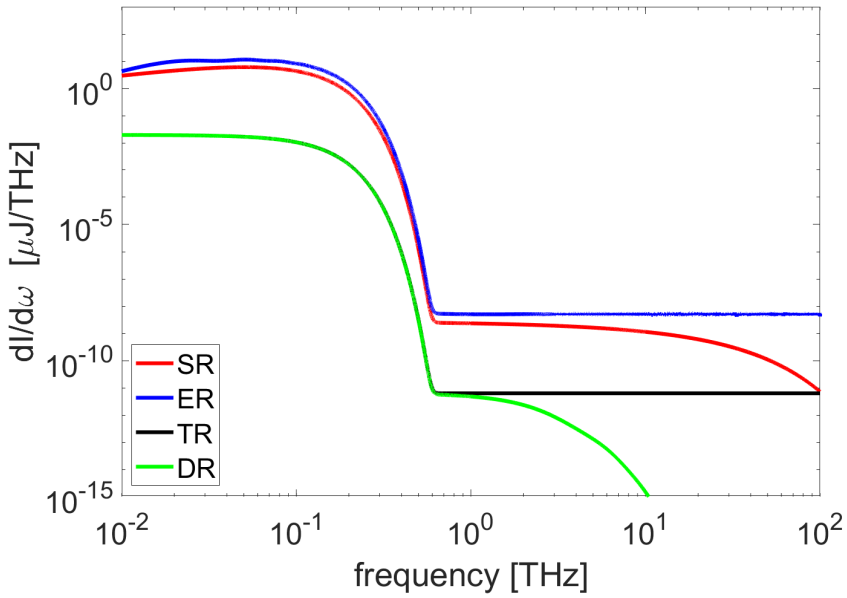

Figure 2.6: Calculated radiation intensity for an electron bunch as a function of radiation frequency for various accelerator-based THz sources based on PITZ electron beam parameters. Here, SR means synchrotron radiation, ER means edge radiation, TR means transition radiation, and DR means diffraction radiation.

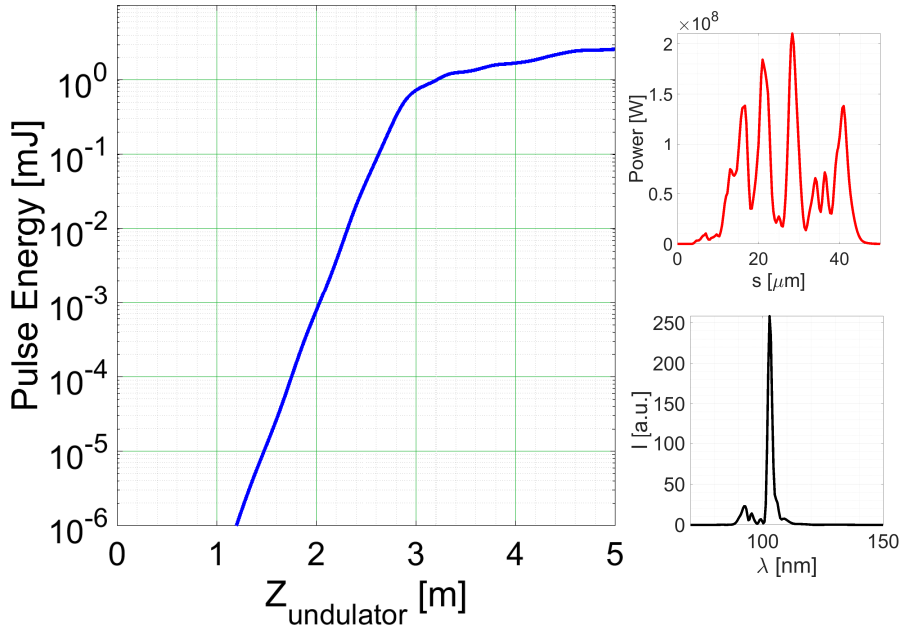

Figure 2.7: Results of SASE FEL simulations using the GENESIS code based on PITZ electron beam parameters. The left plot shows the FEL pulse energy as a function of the position along the undulator (Z_u). The temporal and spectral profiles of the radiation pulse at $Z_u = 5$ m are shown in the upper right and the bottom right plots, respectively.

2.5 Comparison of THz Sources

This section aims to collect and compare the characteristics of various modern THz radiation sources. Only THz sources which can be operated in pulse-mode are of interest, therefore the thermal sources are omitted here. Major characteristics of the laser-based and the accelerator-based THz sources obtained from representative references are listed in Table 2.1. Most of the information was collected from several review papers concerning modern THz radiation sources [5, 6, 12, 40] and several overview papers concerning modern accelerator-based radiation sources [56, 57]. All information in this table is obtained or calculated from experimental data except the calculations of PITZ-based THz sources.

Figure 2.8 shows the plot of pulse energy versus the repetition rate of the pulses from various THz radiation sources as listed in Table 2.1. The red line in the plot represents the repetition rate of 27,000 pulses/second which is the number of the X-ray pulses per second at the European XFEL. Note that; BB means broadband, NB means narrow band, E_{pulse} is the maximum pulse energy, and T_{pulse} is the radiation pulse duration in Table 2.1.

Table 2.1: Summary of pulsed THz sources. The second column presents labels of the THz sources used in Fig. 2.8. Note that; BB means broadband, NB means narrow band, E_{pulse} is the maximum pulse energy, T_{pulse} is the radiation pulse duration, QCL means quantum cascade laser, OR means optical rectification, and DFG means difference frequency generation

Source type	Label	Frequency [THz]	T_{pulse} [ps]	E_{pulse} [μJ]	Rep.rate [Hz]	Ref.
Conventional lasers						
CO_2 laser	CO_2	NB, 28.3	10^9	10^6	10^2	[29]
Germanium laser	Code Name	NB, 1.2 - 2.8	0.3 - 3	~ 667	15	[30]
QCL	QCL	NB, $\sim$3.4	2×10^3	2×10^{-3}	10^3	[32]
Laser-driven sources						
OR, $LINbO_3$	OR,$LINbO_3$	BB, 0 - 0.4	few	436	10	[34]
OR, organic crystals	OR,OH1 OR,DSTMS OR,DAST	BB, 0.1 - 10	N/A	62 - 270	10	[35]
OR, gas plasma	OR,Plasma	BB, 0.5 - 12	< 2	1.9	10^3	[36]
DFG, $LINbO_3$	DFG	NB, 10 - 72	< 0.2	< 19	10^3	[37]
Photoconductive switch	PC-switching	BB, 0 - 3	< 2	6×10^{-3}	250×10^3	[39]
Acc.-based sources (vacuum electronics)						
Bending magnet	BR	BB, 0.1 - 0.5	1	0.07	10	[58]
Edge radiation	ER	BB, 0.1 - 1.5	1	0.07	10	[59]
Undulator radiation	UR	NB, 0.1 - 3	0.5	100	5×10^3	[60]
FEL, optical cavity	FEL-O	NB, 0.5 - 12	< 2	1.9	10^3	[61]
FEL, SASE	FEL-SASE	NB, 4.3	3×10^6	$\sim$500	30	[62]
Transition radiation	TR	BB, 0.1 - 1	0.5	400	10	[63]
Diffraction radiation	DR	BB, 0.1 - 1	0.5	400	10	[63]
Smith-purcell	SMR	NB, 0.2 - 0.4	0.3	N/A	N/A	[64]
Corrugated structure	C-DR	NB, 0.45	0.4	0.4	10	[65]
PITZ-based sources						
Bending magnet	PITZ-BR	BB, 0 - 1	< 1	0.73	2.7×10^3	-
Edge radiation	PITZ-ER	BB, 0 - 1	< 1	0.89	2.7×10^3	-
FEL, SASE	PITZ-SASE	3	20	2×10^3	2.7×10^3	-
Transition radiation	PITZ-TR	BB, 0 - 1	< 1	2.19×10^{-3}	2.7×10^3	-
Diffraction radiation	PITZ-DR	BB, 0 - 1	< 1	2.19×10^{-3}	2.7×10^3	-

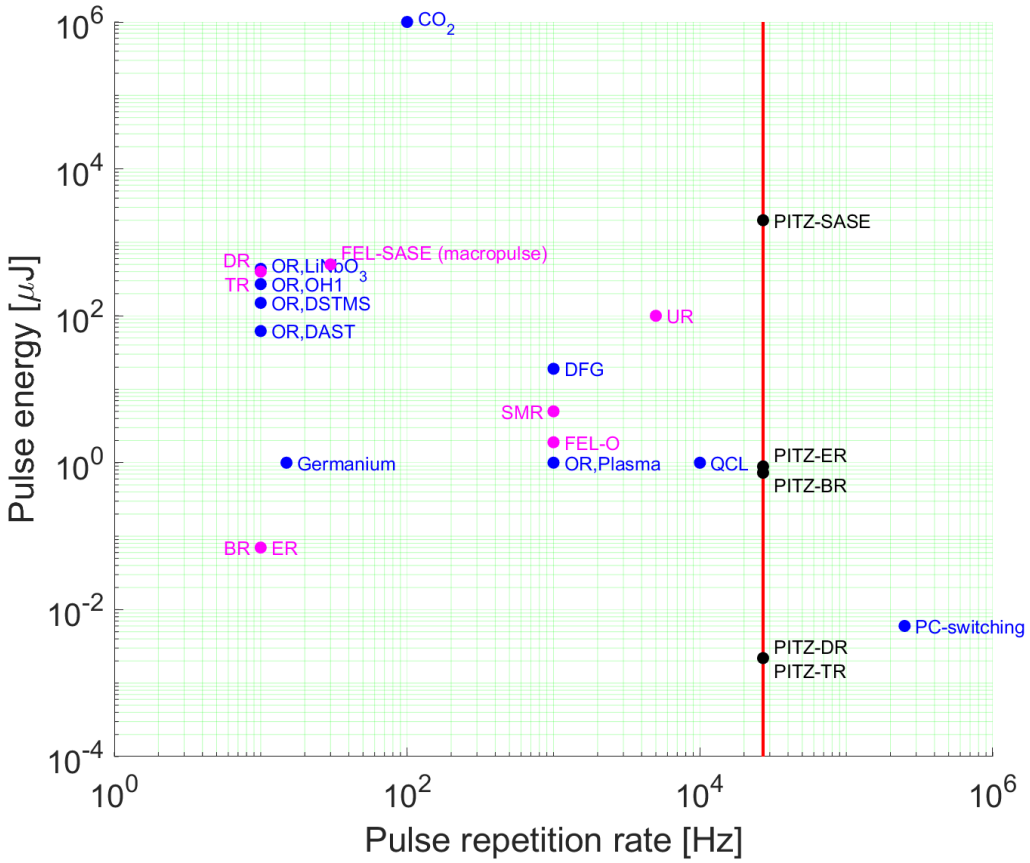

Figure 2.8: Plot of pulse energy as a function of pulse repetition rate for various THz sources as listed in Table 2.1. Information of each label can be found in Table 2.1.

2.6 Concluding Remarks

Advantages of accelerator-based THz sources over the laser-based source are

- *Tunability* - From various means of radiation generation and possibilities of electron beam manipulations, THz radiation with widely-tunable characteristics (e.g., frequency, pulse energy, field pattern, and polarization) can be generated using an electron accelerator.

- *No crystals* - Optical crystals are not used in the mechanisms of radiation generation, therefore no problems from degradation or damage of the crystals by thermal effects.

- *In vacuum process* - The mechanisms of radiation generation happen in the ultra-high vacuum environment, therefore no significant problems from unwanted ionizing radiation and intensity attenuation from air-absorption.

Additionally, THz sources based on the PITZ accelerator have a specific advantage. Since the time structure of the electron pulse train at PITZ can be identical to that at the European XFEL, therefore the time structure of the generated THz pulse train is identical to that of the X-ray pulse train as shown in Fig. 2.8. This allows providing high power, tunable THz pulse for every x-ray pulse.

Since the PITZ-based SASE FEL provides the highest pulse energy compared to the other methods, this method was selected to study further in the next chapters. Other methods which were selected for further studies are the transition radiation and the diffraction radiation using a hole on a metallic plate. Their pulse energies are quite low, but experimental setups are quite simple by modifying an existing screen station in the PITZ beamline.

Chapter 3

Overview of the PITZ Facility

The Photo Injector Test facility at DESY in Zeuthen (PITZ) has been established to develop, study and optimize high brightness electron sources for modern linac-based short-wavelength FELs like FLASH and the European XFEL as already mentioned in Chapter 1. The PITZ beamline was originally designed for the detailed characterization and optimization of the electron beams. Early versions of the beamline layout and their details can be found in references (sorted chronologically) [15], [16] and [66]. Recently, it was modified for applications of electron beams including Plasma Wakefield Acceleration (PWA) experiments [67–69], electron diffraction experiments [70, 71] and THz generation experiments using CTR and CDR which is a part of work in this thesis. A schematic layout of the recent PITZ beamline including the location of the station for THz CTR/CDR generation experiments is shown in Fig. 3.1.

This chapter gives an overview of PITZ. All important components shown in the layout are described including the photocathode laser system, the RF gun section, CDS booster, screen stations, magnets, charge measurement devices, emittance measurement systems, RF deflector, CTR/CDR station and other components. More details of the PITZ accelerator can be found in [15]. Here only details of components related to generation, optimizations and measurements of electron beams for the THz generation studies are presented.

The organization of sections in this chapter is presented in Table 3.1. The components are categorized into two groups. The first group is components for electron beam generation, acceleration and transport. The second group is components for electron beam diagnostics.

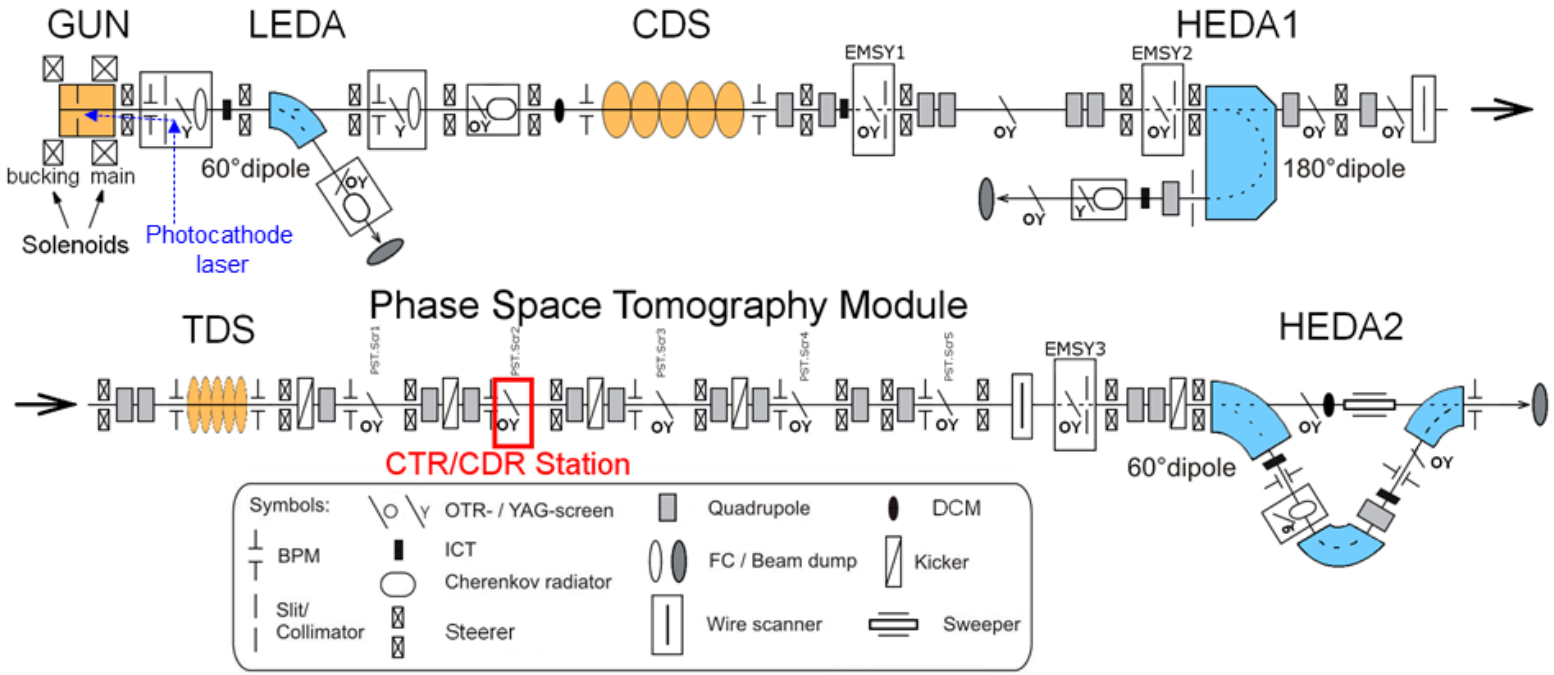

Figure 3.1: Schematic layout of the PITZ beamline.

Table 3.1: List of components of the PITZ accelerator and their corresponding sections which are presented in this chapter.

Components	Sections	Notes
Electron beam generation, acceleration and transport		
Photocathode laser system	3.1.1	Electron beam generation
RF gun section	3.1.2	Electron beam generation
CDS booster	3.1.3	Electron beam accelerating
Quadrupole and steerer magnets	3.1.4 and 3.1.5	Electron beam transport
Electron beam diagnistics		
Faraday cups (FCs) and integrating current transformers (ICTs)	3.2.1	Bunch charge
Screen stations	3.2.2	Transverse distribution
Dispersive sections	3.2.3	Longitudinal momentum
Emittance Measurement SYstems (EMSYs)	3.2.4	Transverse emittance
RF deflector (TDS)	3.2.5	Time resolved measurement

3.1 Components for Electron Beam Generation, Acceleration and Transport

3.1.1 Photocathode Laser System

The photocathode laser system at PITZ was designed, built and developed by the Max-Born Institute, Berlin [72]. The UV laser pulses with a wavelength of 258 nm are generated by this laser system, then transported to the Cs_2Te photocathode inside the gun cavity in order to produce the electron beam by using the photoelectric effect with quantum efficiency (QE) of about 10 % [73]. A detailed description of this laser system can be found in Refs. [74, 75].

The laser system uses a Yb:KGW-based pulse train oscillator. The oscillator generates laser pulses with a wavelength of 1032 nm. Then, the wavelength is converted from 1032 nm to 516 nm by a Lithium triborate (LBO) crystal and finally converted to 258 nm by a beta-Barium Borate (BBO) crystal.

The temporal distribution of the laser pulse can be manipulated by using the laser pulse shaper. It consists of a set of 13 birefringent crystals. It is used to change the short Gaussian temporal shape of the pulses generated by the oscillator to be a comb-like or a flattop shape [76]. Another way for pulse shaping is by using a Lyot filter. The Gaussian pulse duration can be lengthened up to 12 ps FWHM without using the pulse shaper.

The nominal pulse repetition rate of the laser system is 1 MHz in burst mode as presented in Fig. 3.2. The UV laser pulses which are transported to the photocathode have a maximum pulse energy of about 2 µJ. The pulse energy can be reduced by using the

attenuator which is a polarizer and a half wave plate on a rotational stage. The transverse size of the laser can be adjusted by using a Beam Shaping Aperture (BSA) which is a variable-size circular aperture.

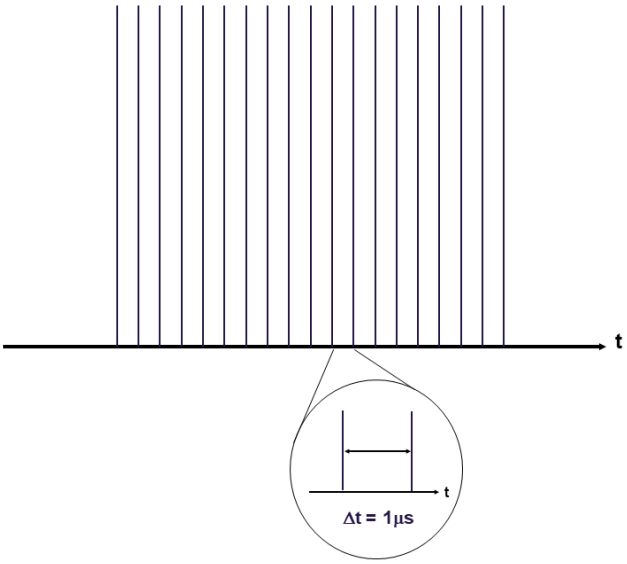

Figure 3.2: Time structure of the photocathode laser pulse train operating with a repetition rate of 1 MHz.

The transverse profile of laser pulses is monitored by using the so-called virtual cathode camera. This is a UV-sensitive CCD camera, for which the distance from the BSA to its location is equal to the distance from the BSA to the photocathode. The temporal profile of the laser pulses is measured by the optical sampling system (OSS) [74] which has a resolution of about 1 ps. The OSS is based on the principle of a cross correlator - scanning short probe laser pulses over the UV laser pulses by changing the relative timing between them. More detail of the OSS can be found in [74].

Examples of the measured temporal and transverse profiles of a laser pulse are shown in Fig. 3.3. The transverse profile was measured by the virtual cathode camera with the BSA diameter size set to 3.2 mm. In-homogeneity of the transverse profile is related to imperfection in frequency conversions in the photocathode system. Three temporal profiles measured by the OSS are shown here including a short (non-stretched) Gaussian profile with duration of 2.4 ps FWHM which is the laser profile without pulse shaping; a long Gaussian profile with duration of 12 ps FWHM which is the laser profile when using one of the Lyot filters and a flattop profile with duration of 22 ps FWHM which is the profile generated by using the pulse shaper.

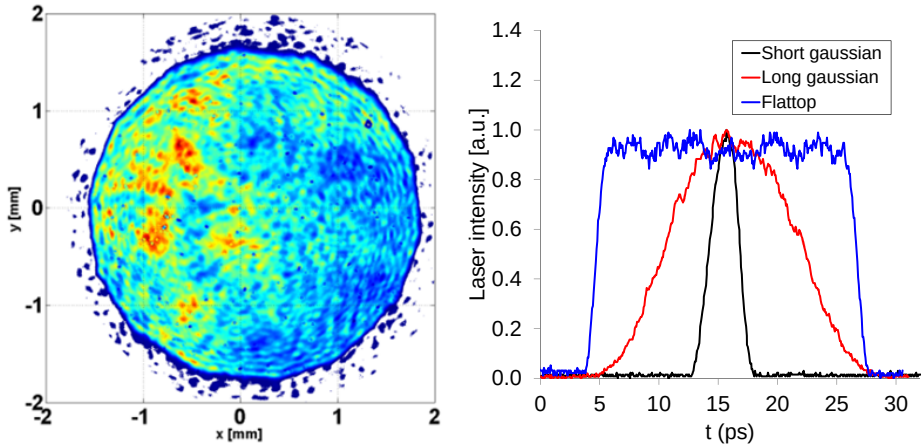

Figure 3.3: Photocathode laser pulse transverse distribution (left plot) and temporal profile (right plot).

3.1.2 RF Gun Section

The RF gun section consists of an L-band RF cavity, main and bucking solenoids as its 3D-model shown in Fig. 3.4. The RF cavity, called the RF gun, is a 1.6 cell normal conducting copper cavity with a Cs_2Te photocathode located at the wall of the first cell. Note that the cathode plane is defined as the zero position of the beamline coordinate $Z = 0$ used in this thesis. The RF gun is surrounded by solenoids as their locations can be seen in Fig. 3.4. The main solenoid is used to focus the electron beam which naturally expands due to the space-charge force. Since the magnetic field from the main solenoid on the photocathode can induce an angular momentum to the extracted electron bunch, the bucking solenoid is installed behind the photocathode and used to eliminate the field from the main solenoid on the photocathode [77]. Important parameters of the RF gun are listed in Table 3.2. The normalized longitudinal electric field profile inside the RF gun is shown in Fig. 3.5 together with the normalized longitudinal magnetic field profile of the main and bucking solenoids.

From Table 3.2, the RF gun operates with RF pulse trains at a repetition rate of 10 Hz, and each RF macropulse has a pulse length of 650 µs. Electron bunches are generated from the laser pulses (see Fig. 3.2) which overlap with the RF pulse train. The time structure of the electron bunch train generated by the RF gun and the photocathode laser are presented in Fig. 3.6.

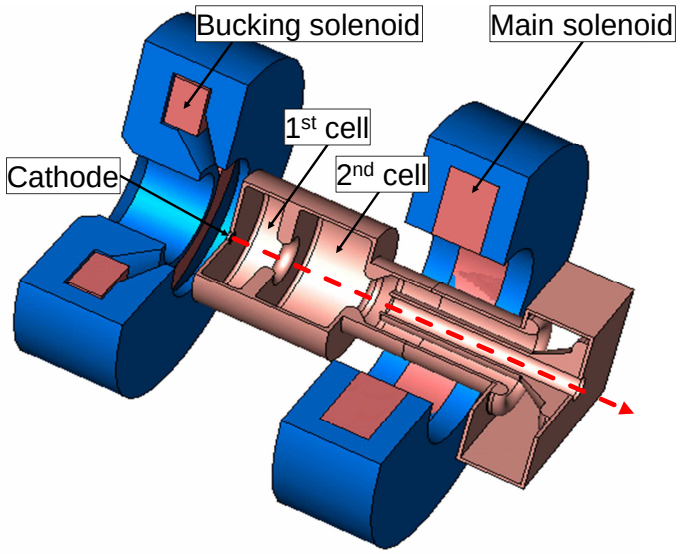

Figure 3.4: 3D-layout of the PITZ gun section. The red-dashed arrow shows the direction of the electron beam.

Table 3.2: Important parameters of the RF gun

Parameters	**Values**
Operating RF frequency	1.300 GHz
Peak power of RF pulse	6.5 MW
Maximum operating RF pulse length	650 µs
RF pulse repetition rate	10 Hz
Maximum accelerating gradient	60 MV/m
Maximum momentum gain	∼7 MeV/c

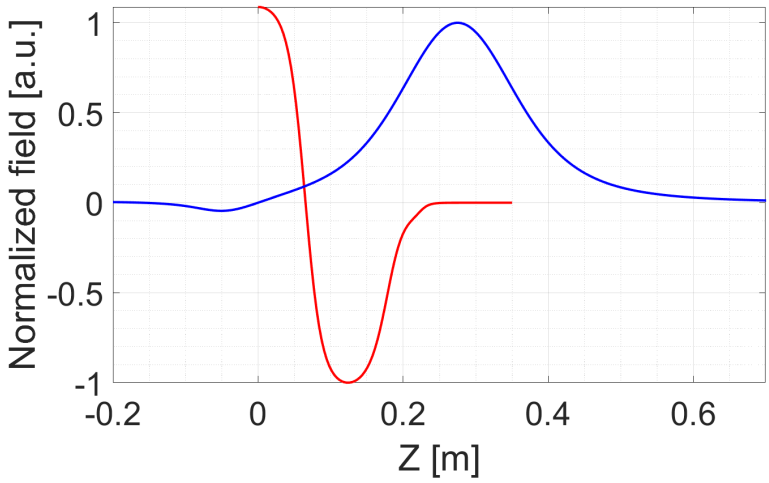

Figure 3.5: Normalized longitudinal electric field profile inside the RF gun (red line) and normalized longitudinal magnetic field profile of the main and bucking solenoids (blue line). Z = 0 is the position of the photocathode.

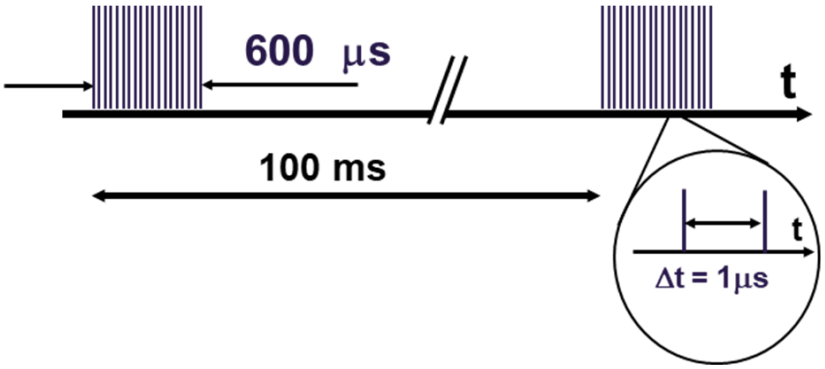

Figure 3.6: Time structure of the electron bunch train generated by the RF gun and the photocathode laser.

3.1.3 CDS Booster

The second L-band RF accelerating cavity in the PITZ beamline is a Cut Disk Structure (CDS) linac called CDS Booster. It is made of normal conducting copper like the RF gun and consists of 14 cells. It was developed by the Institute for Nuclear Research of the Russian Academy of Sciences (INR-RAS) [78]. With a combination of the RF gun and the CDS booster, the electron beam can be accelerated to reach a maximum mean momentum of about 24.5 MeV/m. Important parameters of the CDS booster are presented in Table 3.3. The simulated normalized longitudinal electric field profile inside the booster is presented in Fig. 3.7

Table 3.3: Important parameters of the CDS booster

Parameters	**Values**
Operating RF frequency	1.300 GHz
Peak power of RF pulse	3 MW
Operating RF pulse length	200 µs
RF pulse repetition rate	10 Hz
Maximum accelerating gradient	14 MV/m
Maximum momentum gain	20 MeV/c

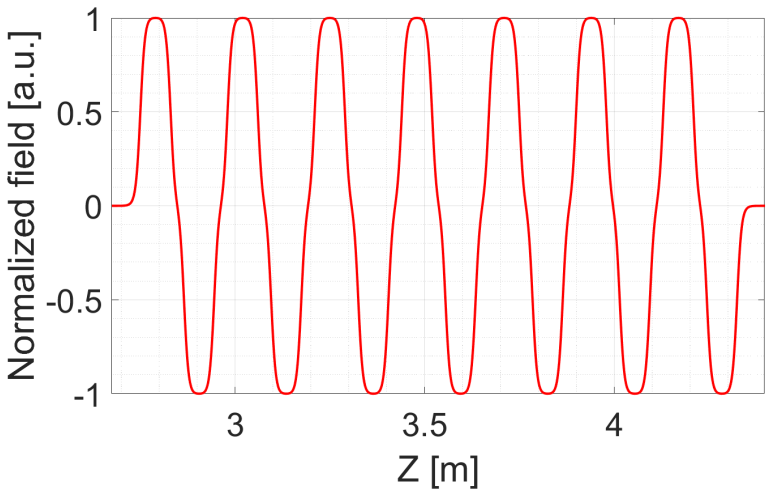

Figure 3.7: Simulated normalized longitudinal electric field profile inside the CDS booster. Z = 0 is referenced as the position of the photocathode.

3.1.4 Quadrupole Magnets

Quadrupole magnets are used for focusing the electron beam. Generally, at least two quadrupole magnets, called quadrupole doublet, have to be used in order to focus the beam in both transverse axes.

Quadrupole magnets are installed at different locations along the beamline for beam transport and focusing. All quadrupole magnets in the straight section are identical and are manufactured by Danfysik [79]. Figure 3.8 presents a plot of the measured quadrupole gradient as a function of the applied current and a plot of the normalized measured transverse magnetic field as a function of the longitudinal position along the quadrupole magnet. Based on these two plots, the quadrupole magnet can provide a maximum magnetic gradient of 8.4 T/m with an effective length of ∼40 mm. Figure 3.9 shows positions of the quadrupole magnet along the straight section of the PITZ beamline.

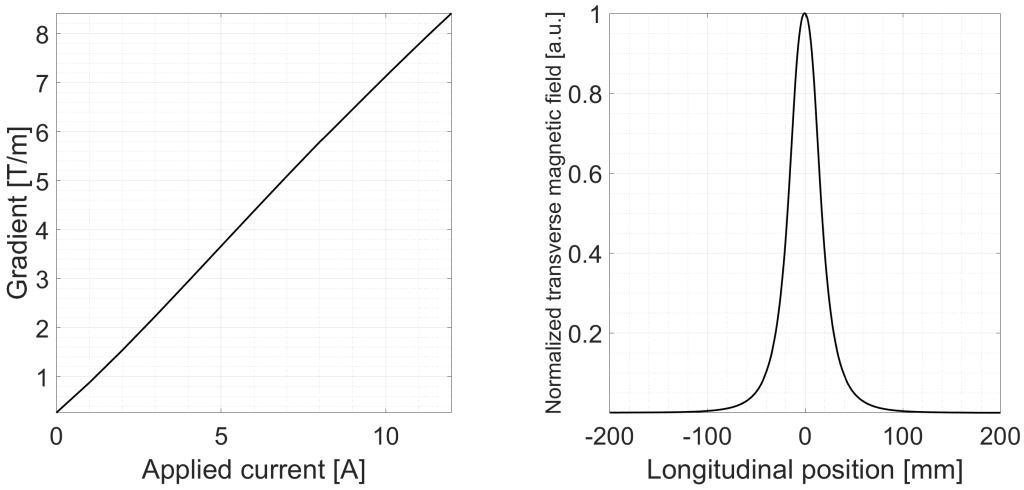

Figure 3.8: The left plot shows measured quadrupole gradient as a function of the applied current, and the right plot shows the normalized measured transverse magnetic field as a function of the longitudinal position along the quadrupole (0 position is the center of the magnet).

3.1.5 Steerer Magnets

A steerer magnet is a small dipole magnet used for controlling the beam trajectory. Air coil steerer magnets are distributed along the PITZ beamline as can be seen from their locations in Fig. 3.1. Generally, the steerer magnets provide a maximum magnetic field of few mT with an effective length of up to 100 mm. More details about the steerer magnets can be found in Ref. [80].

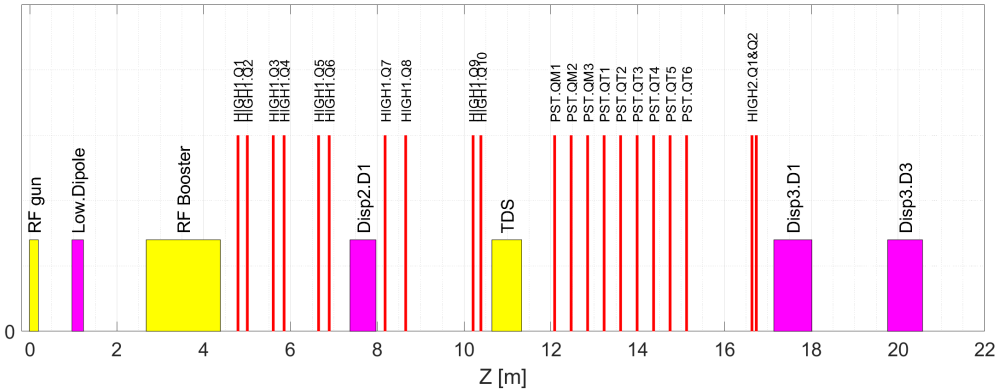

Figure 3.9: Plot of positions of the quadrupole magnets along the straight section of the PITZ beamline. Here, TDS is the RF deflector (see section 3.2.5); Low.Dipole, DISP1.D1, DISP2.D1, and DISP3.D1 are dipole magnets.

3.2 Components for Electron Beam Diagnostics

3.2.1 Charge Measurement Devices

There are two types of charge measurement devices at PITZ, Faraday cups (FCs) and integrating current transformers (ICTs). Locations of the charge measurement devices along the straight section of the PITZ beamline are listed in Table 3.4.

Table 3.4: Charge measurement devices and their location along the straight section of the PITZ beamline

Name	Type	Middle position [m]
LOW.FC1	Faraday cup	0.803
LOW.FC2	Faraday cup	1.379
LOW.ICT1	ICT	0.903
HIGH1.ICT1	ICT	5.117
HIGH2.ICT1	ICT	17.080

A Faraday cup is a copper block designed to collect electrons which impact the block. Then, the collected charges create a corresponding current. There are two FCs, LOW.FC1 and LOW.FC2, installed between the RF gun and the CDS booster. The Faraday cups are suitable for low charge measurements (up to 0.2 nC).

An ICT is a non-destructive charge measurement device by using the principle of electromagnetic induction. There are ICTs (products of Bergoz Instrumentation [81]) installed in the straight section of the PITZ beamline: LOW.ICT1 used for measuring the bunch charge of the beam that exits from the RF gun, HIGH1.ICT1 used for measuring

the bunch charge of the beam that exits from the CDS booster, and HIGH2.ICT1 used for measuring the bunch charge at the ending part of the beamline. The ICTs are mainly used to measure the bunch charge higher than 0.2 nC.

3.2.2 Screen Stations

Many screen stations are distributed over the beamline to measure the transverse distribution of the electron beam at different locations. Inside each screen station, there is a Cerium-doped Yttrium aluminum garnet (Ce:YAG) powder screen, or called shortly as a YAG screen, that is attached to a movable linear stage so that the screen can be moved in and out from the beamline. The light output from the YAG screen is monitored and readout with a 12-bit CCD camera (product model Prosilica GC 1350 of Allied Vision Technologies GmbH [82]). Table 3.5 shows positions and resolutions of the screen stations in the straight section of the PITZ beamline. A plot of their positions w.r.t. the position of the cathode is shown in Fig. 3.10.

Table 3.5: Positions and typical resolutions of the screen stations in the straight section of the PITZ beamline. Various values of resolution at the same screen station means that the station has an option to use different camera lenses.

Screen station name	Position [m]	Resolution [mm/pixel]
LOW.Scr1	0.803	0.040
LOW.Scr2	1.379	0.017
LOW.Scr3	1.708	0.014
HIGH1.Scr1	5.277	0.015, 0.009
HIGH1.Scr3	7.125	0.020, 0.007
HIGH1.Scr4	8.41	0.036, 0.019, 0.006
HIGH1.Scr5	8.92	0.036, 0.020, 0.007
PST.Scr1	12.278	0.038, 0.022
PST.Scr2	13.038	0.037, 0.022
PST.Scr3	13.798	0.036, 0.022
PST.Scr4	14.558	0.037, 0.022
PST.Scr5	15.318	0.037, 0.022
HIGH2.Scr1	16.303	0.035
HIGH2.Scr2	18.262	0.064

3.2.3 Dispersive Sections

Based on the Lorentz force equation, by assuming that the magnetic field vector $\vec{B}$ is normal to the velocity vector $\vec{v}$, the trajectory of the electron motion in a region with

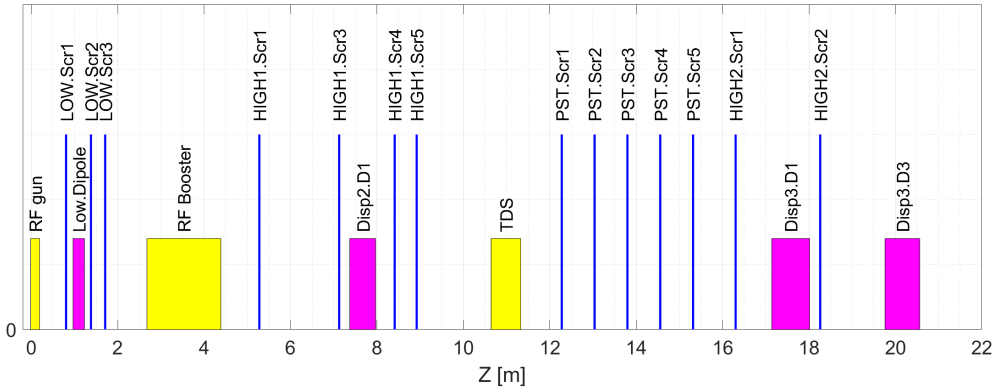

Figure 3.10: Plot of position of the screen station along straight section of the PITZ beamline. Here, TDS is the RF deflector (see section 3.2.5); Low.Dipole, DISP1.D1, DISP2.D1, and DISP3.D1 are dipole magnets.

uniform dipole magnetic field can be described by [83]:

$$\rho\,[\mathrm{m}] = \frac{p}{eB} = 0.2998 \quad \frac{p[\mathrm{GeV/c}]}{B[\mathrm{T}]}, \tag{3.1}$$

where ρ is the bending radius, p is the particle momentum and B is the component of the magnetic field vector that is normal to the velocity vector. Equation (3.1) can be written in terms of the momentum as

$$p[\mathrm{MeV/c}] = \frac{\rho\,[\mathrm{m}] \cdot B[\mathrm{T}]}{0.2998 \times 10^{-3}}, \tag{3.2}$$

This equation means that electrons with different momenta are bent by a dipole magnet to different curves. By placing a screen after the dipole magnet, the transverse distribution measured by this screen represents the momentum distribution of the electron beam. A setup including a dipole magnet and a monitor screen can be called a momentum spectrometer.

There are three dispersive sections used as momentum spectrometers in the PITZ beamline (see Fig. 3.1), Low Energy Dispersive Arm (LEDA), the first High Energy Dispersive Arm (HEDA1) and the second High Energy Dispersive Arm (HEDA2). LEDA is used to measure the longitudinal momentum distribution of the beam that is accelerated by the RF gun while HEDA1 and HEDA2 are used for the beam that is accelerated by the booster [84]. Furthermore, HEDA2 together with the RF deflector (see Section 3.2.5) can be used for longitudinal phase space measurements [85].

3.2.4 Emittance Measurement Systems (EMSYs)

There are three Emittance Measurement SYstems (EMSYs) installed in the PITZ beamline: EMSY1, EMSY2 and EMSY3, as their locations can be seen in Fig. 3.1. Tungsten slits are installed inside these systems in order to use the single slit scan technique for the transverse emittance measurements. Only EMSY1 was used for transverse phase space measurements in this thesis. Details concerning specifications of EMSY1, the principle and the procedure of the emittance measurements are explained in [86] and [16]. They will be reviewed later in Chapter 5.

3.2.5 RF Deflector (TDS)

An RF deflector, also known as a Transverse Deflecting Structure (TDS), is a component that generally is used for time-resolved measurements of an electron bunch including the longitudinal profile, the slice transverse emittance, and the longitudinal phase space. When an electron bunch passes through the TDS, the bunch is deflected by a time-dependent transverse kick. Electrons within the bunch gain transverse momentum linearly dependent on their longitudinal coordinates. By imaging the transverse profile of the deflected bunch, the longitudinal distribution can be derived by using the correlation of the longitudinal positions to the transverse momentum [85].

The TDS of PITZ was designed and built by INR-RAS [85, 87]. It consists of 16 cells with a total length including the vacuum flanges of 0.7 m. The structure is designed to be a traveling-wave cavity and has an RF field mode with a vertical deflecting electric field. Important parameters of the TDS are summarized in Table 3.6.

Table 3.6: Important parameters of the TDS [85]

Parameter	
Operating RF frequency	2.997 GHz
Deflecting voltage	0.2 - 1.7 MV
Operating RF pulse length	0.7 - 3.1 µs
Filling and decay time	< 200 ns

When an electron travels on the axis of the TDS, the Lorentz force from the transverse electric and magnetic fields interacts with the electron. The magnitude of the force (F) can be described by

$$F = A \cdot \cos(\phi + \omega t), \tag{3.3}$$

where A is the total transverse deflecting force amplitude, ϕ is the transverse deflecting force phase, and ω is the angular frequency of the RF field. Profiles of A and ϕ along the TDS operating at PITZ are plotted in Fig. 3.11

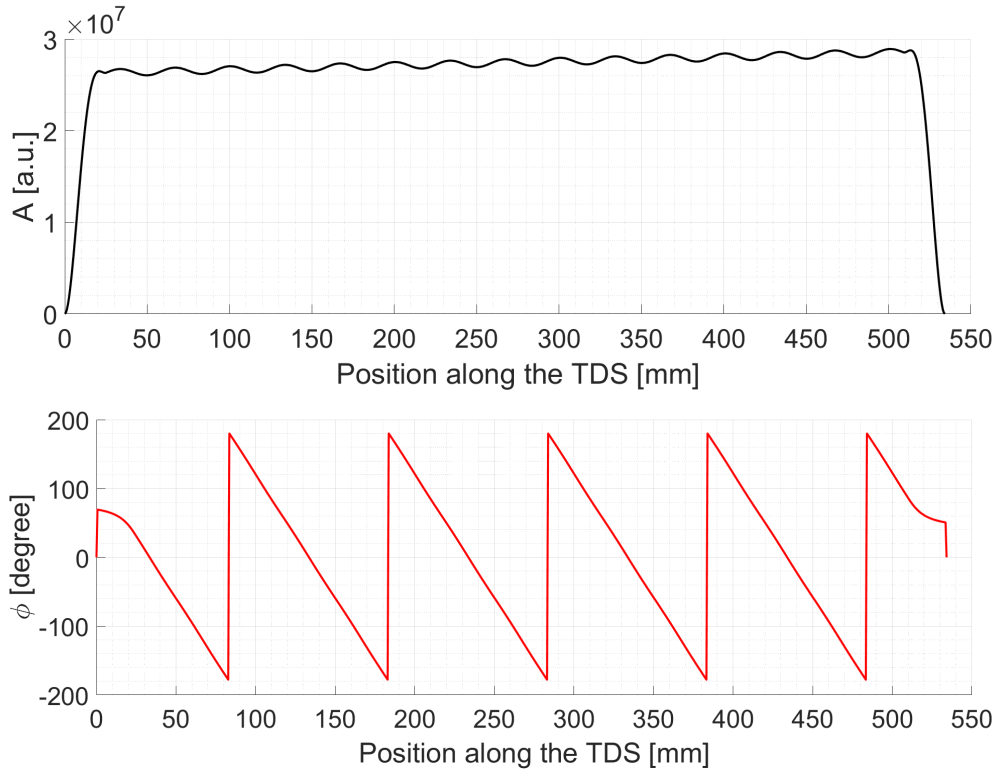

Figure 3.11: Plots of calculated total transverse deflecting force amplitude (top) and calculated transverse deflecting force phase (bottom) as a function of the position along the TDS.

During operation of the TDS, an electron bunch that passes through the TDS experiences a constant phase of the transverse deflecting force. This means each part of the bunch always experiences a nearly constant deflecting force along the TDS. By propagating the longitudinal center part of the bunch through the TDS at the zero RF phase, the center part will go through the TDS witout any deflection while the deflecting angle of other parts depends linearly on the distance from the center part. This relation can be used for the bunch length calculation which will be reviewed later in Chapter 5.

Chapter 4

Start-to-End Simulations of THz sources based on PITZ accelerator

Start-to-end (S2E) simulations of THz radiation sources based on the PITZ accelerator were performed in order to ensure that the radiation can be generated practically and to prepare experiments. The S2E simulations include beam dynamics simulations for optimization and transport of the electron beam starting from the cathode to the point where the radiation is generated and calculations of the THz radiation parameters.

This chapter presents and discusses S2E simulations of THz radiation generation based on the PITZ accelerator for two scenarios: (i) Self-Amplification of Spontaneous Emission Free-Electron Lasers (SASE FELs) using an uncompressed high charge electron bunch and (ii) Coherent Transition Radiation (CTR) and Coherent Diffraction Radiation (CDR) using a short electron bunch. Figure 4.1 shows the schematic layout of the PITZ beamline including radiation stations for simulation studies. For SASE FEL, an extension part including quadrupole magnets and an undulator was assumed to be added to the end of the beamline. For CTR/CDR, an existing screen station (PST.Scr2) located at $Z = 13.038$ m is assumed to be modified to use as a CTR/CDR station.

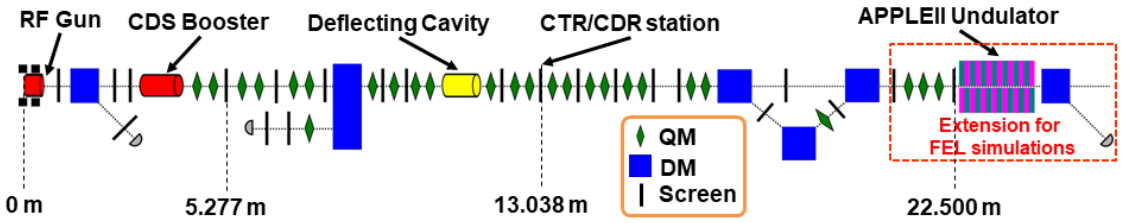

Figure 4.1: Schematic layout of the PITZ beamline including radiation stations for simulations studies. Here QM, DM, and Screen represent quadrupole magnets, dipole magnets, and screen stations, respectively.

4.1 S2E Simulations for the SASE FEL option

Before performing the S2E simulations for the SASE FEL option, the first task is to consider design parameters of the undulator. Then, the beam dynamics simulations using A Space charge TRacking Algorithm (ASTRA) [55] code were performed for electron beam optimization and transport to the assumed undulator entrance. Finally, the THz SASE FEL process simulations based on the optimized electron beams were performed using Genesis 1.3 code [48].

4.1.1 Design Considerations for Undulator

The objective of this section is to determine the undulator type and undulator parameters for generating FEL radiation with tunable resonance wavelength (λ_{rad}) between 20 µm and 100 µm. An APPLE-II type undulator is an undulator that can vary the horizontal and vertical magnetic field components by moving the magnet arrays and yields the ability to vary polarization of the generated radiation [88]. The model of an APPLE-II type undulator from the conceptual design report of the FERMI FEL facility [89] was decided to be used for the simulations. The peak magnetic field B_0 of the undulator for variable polarization mode can be calculated by using the following equation [89]:

$$B_0 = a \cdot \exp\left(-b\frac{g}{\lambda_u} + c\left(\frac{g}{\lambda_u}\right)^2\right), \tag{4.1}$$

where g is the undulator gap and λ_u is the undulator period length. a, b and c are the coefficients for various polarization modes of the undulator where (a, b, c) = (1.76, 2.77, -0.37), (1.54, 4.46, 0.43) and (2.22, 5.19, 0.88) for horizontal, circular and vertical polarization modes, respectively. Relations among B_0, λ_u, g, undulator parameter K, radiation wavelength λ_{rad} and electron beam momentum can be calculate by using equations 4.1 2.5 and 2.6.

Several constraints were considered for the design of the undulator. The minimum gap of the undulator is assumed to be 10 mm for sufficient space for the beam pipe and electron beam transport. The maximum electron beam momentum is limited at 22 MeV/c which is barely below the maximum momentum accessible at PITZ. Figure 4.2 presents the calculated beam momentum as a function of the undulator gap for various radiation wavelengths, undulator period lengths and polarization modes. Under the above-mentioned conditions, the proper period length of the undulator is 40 mm as all plots for this case are collected in Fig. 4.2d. By considering all three polarization mode together, the radiation wavelengths between 20 µm and 100 µm can be generated with beam momenta between 14 MeV/c and 22 MeV/c, and gap widths between ∼10 mm and ∼22 mm. These parameter ranges fit perfectly to the initial constraints.

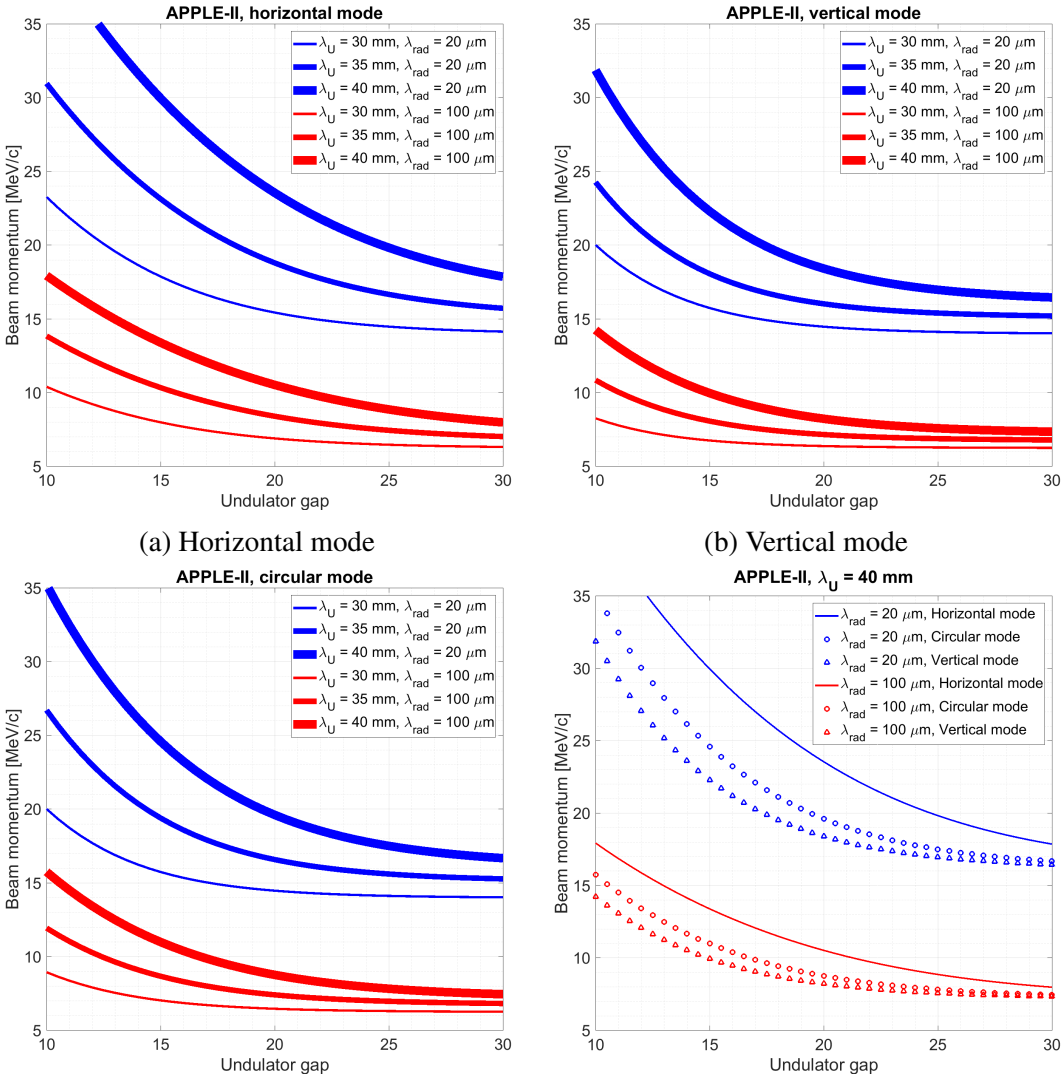

(a) Horizontal mode

(b) Vertical mode

(c) Circular mode

(d) $\lambda_u = 40\,\text{mm}$, all modes

Figure 4.2: Electron beam momenta for radiation wavelengths of 20 µm and 100 µm as a function of the undulator gap for various period lengths and polarization modes of the APPLE-II type undulator.

In further studies, only the helical mode of the APPLE-II type undulator was used for the SASE FEL simulations. The process of S2E simulation studies for the helical mode can be repeated for the studies of the horizontal and vertical modes with almost similar routines and strategies. The difference is matching and transport of electron beam into the undulator. An example of S2E simulation studies using the LCLS-I undulator which is a planar undulator is presented in Appendix A.

4.1.2 Calculation of FEL Parameter Space

An analysis of the FEL parameter space including the saturation power and the saturation length of the SASE FEL at PITZ was performed for two cases of radiation: 100 µm and 20 µm wavelengths. It is performed by using the Genesis1.3 code. The helical undulator with a period length of 40 mm as considered in the previous section was used as the FEL radiator. Electron beams with beam momenta of 15 MeV/c and 22 MeV/c are used for the cases of 100 µm and 20 µm, respectively. The longitudinal current distribution was assumed to have a parabolic shape with a FWHM length of about 7.5 mm. The energy spread of 0.5 % and the transverse slice emittance were assumed to be constant along the bunch.

Figures 4.3, 4.4, and 4.5 show an overview of the simulated saturation characteristics of the SASE FEL versus peak current and emittance. Little dependence of the saturation characteristics on the emittance is observed. Analyzing the influence of the peak current shows that operation at higher currents is preferable for a reduction of the saturation length and for an increase of the peak radiation power. By using an electron beam with 4 nC bunch charge which corresponds to a peak current of 160-180 A, saturation lengths up to 3.5 m and 5.5 m can be expected for the cases of λ_{rad} = 100 µm and 20 µm, respectively.

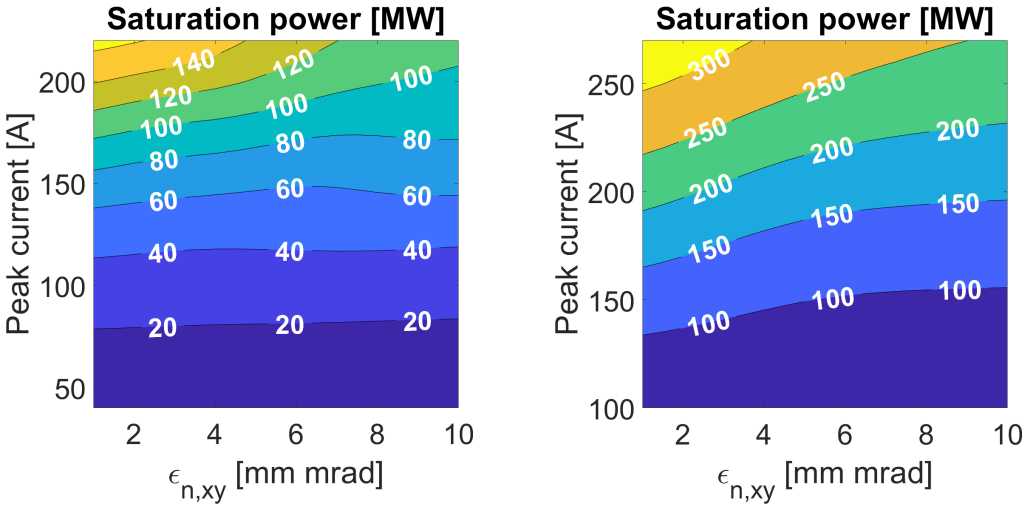

Figure 4.3: Contour plot for the saturation power [MW] versus peak current [A] and normalized emittance [mm mrad]. Left and right plots correspond to the cases of 100 µm using a 15 MeV/c electron beam and 20 µm using a 22 MeV/c electron beam, respectively.

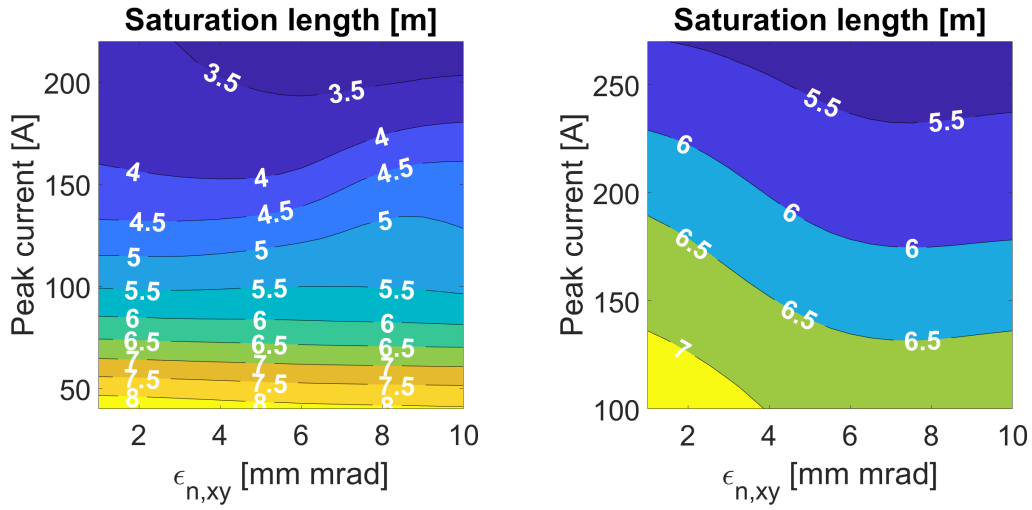

Figure 4.4: Contour plot for the saturation length [m] versus peak current [A] and normalized emittance [mm-mrad]. Left and right plots correspond to the cases of 100 µm using a 15 MeV/c electron beam and 20 µm using a 22 MeV/c electron beam, respectively.

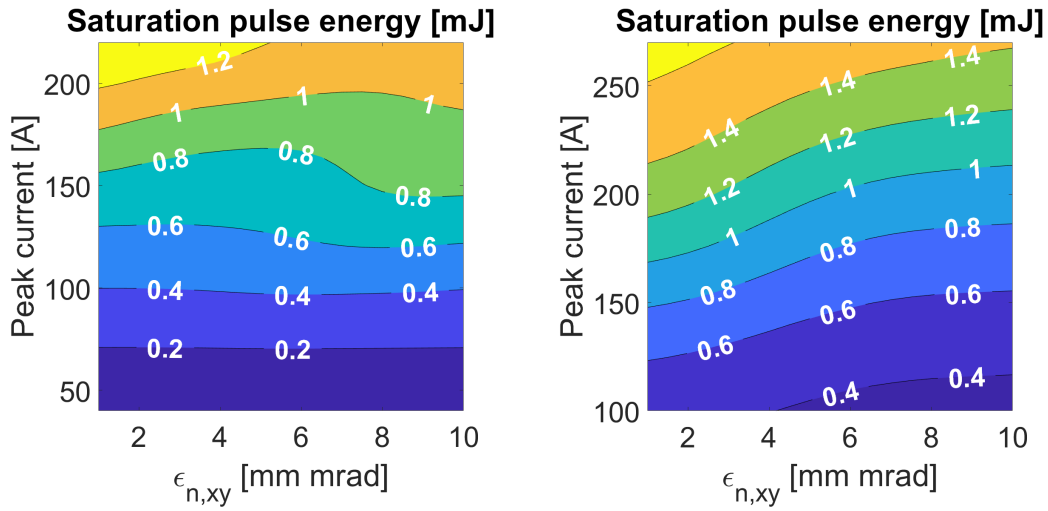

Figure 4.5: Contour plot for the saturation pulse energy [mJ] versus peak current [A] and normalized emittance [mm-mrad]. Left and right plots correspond to the cases of 100 µm using a 15 MeV/c electron beam and 20 µm using a 22 MeV/c electron beam, respectively.

4.1.3 Electron Beam Dynamics Simulations

In order to verify the feasibility of the electron beam parameters assumed in Section 4.1.2, beam dynamics simulations using the ASTRA code were performed with 2×10^5 macro-particles. The simulations include generation and optimization of the space charge

dominated 4 nC electron beams and then transport of the beams to the undulator entrance. The beam transport line layout used in these simulations follows the schematic diagram in Fig. 4.1. Photocathode laser pulses with a flattop temporal profile (FWHM duration of 21.5 ps) were used. In order to ensure that the RMS laser spot size is big enough for generating 4 nC bunch charge, the RMS laser spot size was set to 1.25 mm which is close to the maximum size from the practical point of view (the cathode has a diameter of 5 mm). The peak electric field of the gun cavity was fixed at 60 MV/m and the phase of maximum mean momentum gain (MMMG) was used. For the booster cavity, the peak electric fields were set to 9.8 MV/m and 17.2 MV/m for the beam momenta of about 15 MeV/c and 22 MeV/c, respectively. The booster phase and the main solenoid current were tuned for compromising between low momentum spread and high peak current at the position of the first monitoring screen after the booster called High1.Scr1 located at $Z = 5.277$ m (see Fig. 3.1).

Figure 4.6 shows the contour plots of the energy spread, the peak current and the transverse normalized emittance as a function of the main solenoid current and the booster phase (w.r.t. MMMG) of the 15 MeV/c beam at High.Scr1. The red circles in the plots indicate the booster phase and solenoid current for the optimized beam. With the booster phase of -18° (w.r.t. MMMG) and the main solenoid current of 381 A, the beam has a RMS momentum spread of 55.38 keV/c, a peak current of about 170 A and a transverse normalized emittance of 2.84 mm mrad.

Similarly, figure 4.7 shows the contour plots of the energy spread, the peak current and the transverse normalized emittance as a function of the main solenoid current and the booster phase (w.r.t. MMMG) of the 22 MeV/c beam at High.Scr1. The red circles in the plots indicate the booster phase and solenoid current for the optimized beam. With the booster phase of -10° (w.r.t. MMMG) and the main solenoid current of 383 A, the beam has a RMS momentum spread of 62.09 keV/c, a peak current of about 170 A and an transverse normalized emittance of 2.74 mm mrad.

The next step is to transport the optimized electron beams from the High1.Scr1 to the assumed undulator entrance at $Z = 22.500$ m (see Fig. 4.1). The quadrupole magnets along the beamline were used for beam transport and matching. A fast space charge tracking code Space Charge Optimizer (SCO) [90] was used to optimize the quadrupole magnet gradients, then solutions of the optimized gradients obtained from SCO were plugged into the ASTRA code. Since the FEL radiator is a helical undulator, the matching goal is to have transverse symmetric beam size and emittance at the undulator entrance. Furthermore, the matching strategy is to slightly focus the beam transversely during the transport in order to have a compromise between the smallest beam size and the weakest beam divergence at the undulator entrance.

Figure 4.8a and b shows the evolution of RMS beam sizes and the transverse emittance values of the 15 MeV/c beam transport from the cathode position ($Z = 0$) to the undulator entrance ($Z = 22.50$ m). Black bars in the plots represent the quadrupole mag-

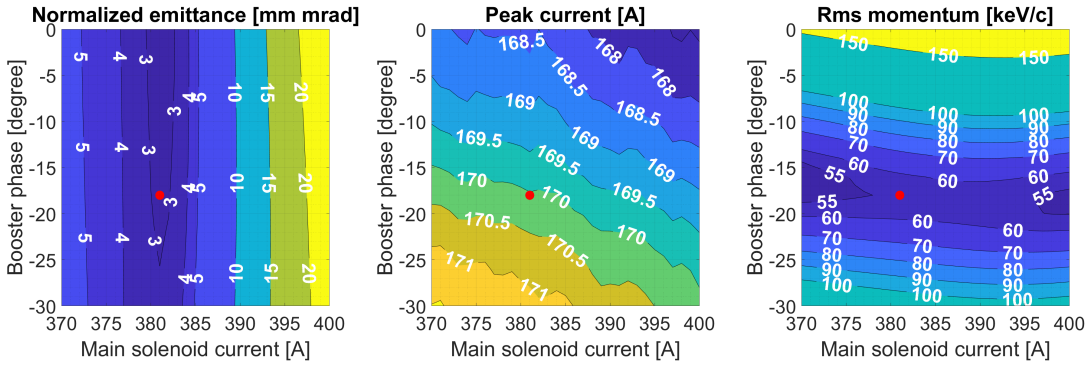

Figure 4.6: Contour plots of the transverse normalized emittance (left), the peak current (middle) and the RMS momentum (right) as function of the main solenoid current and the booster phase (w.r.t. MMMG) of the 4 nC, 15 MeV/c beam at High.Scr1.

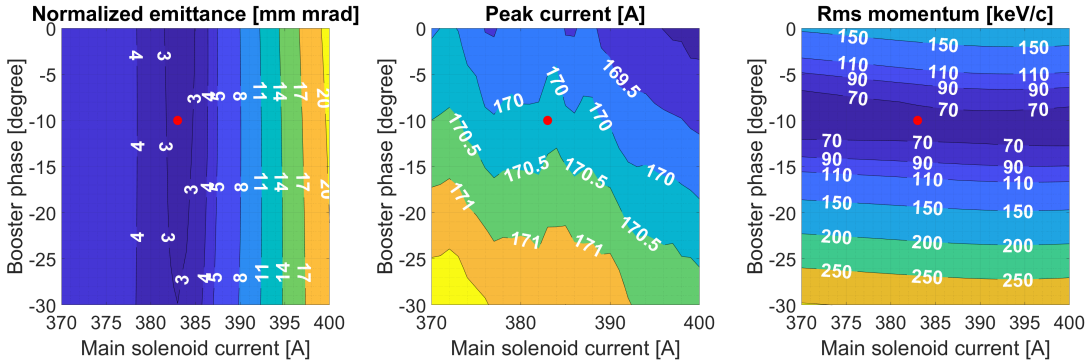

Figure 4.7: Contour plots of the transverse normalized emittance (left), the peak current (middle) and the RMS momentum (right) as function of the main solenoid current and the booster phase (w.r.t. MMMG) of the 4 nC, 22 MeV/c beam at High.Scr1.

net positions and this length represents the relative gradients used for the beam transport. The transverse RMS beam sizes were slightly reduced from about 3 mm at $Z = 6$ m to below 0.5 mm at the undulator entrance ($Z = 22.5$ m) while the transverse focusing has no impact to the longitudinal beam size. For the transverse emittance evolution, the emittance values are increased from the optimized values at High1.Scr1 ($Z = 5.277$ m) during beam transport. However, this issue is not critical since the saturation characteristics of the SASE FEL only little depends on the transverse emittance as studied in Section 4.1.2. Phase spaces and longitudinal profiles of the 15 MeV/c beam at the undulator entrance are shown in Fig. 4.9.

Figure 4.8c and d shows the evolution of RMS beam sizes and the transverse emittance values of the 22 MeV/c beam transport from the cathode position ($Z = 0$) to the undulator entrance ($Z = 22.5$ m). Behaviors of beam parameter evolution are similar to the

15 MeV/c beam case. Transverse phase spaces and longitudinal profiles of the 22 MeV/c beam at the undulator entrance are shown in Fig. 4.10. Important parameters of the beam are summarized in Table 4.1 for both cases of the beam momenta, 15 and 22 MeV/c.

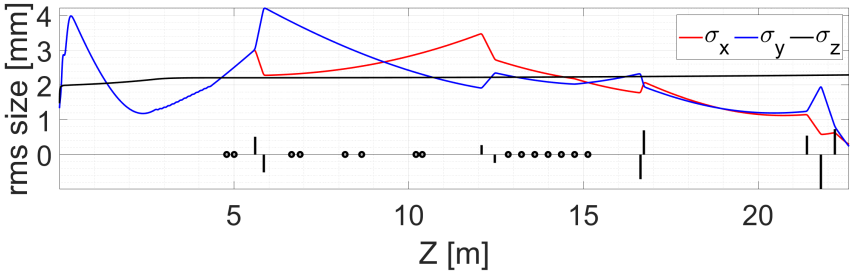

(a) Evolution of the RMS sizes of the 15 MeV/c beam

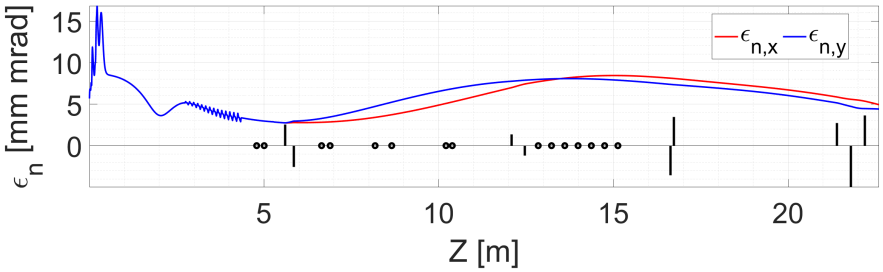

(b) Evolution of the transverse normalized emittances of the 15 MeV/c beam

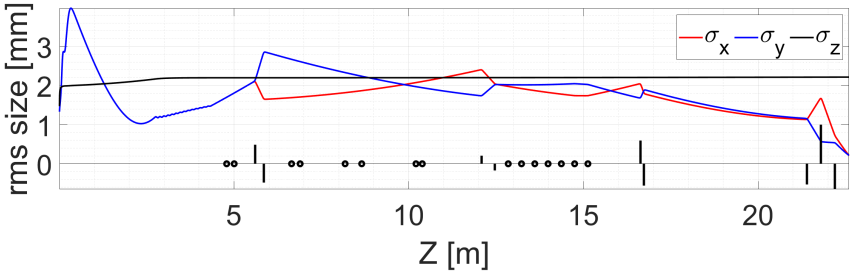

(c) Evolution of the RMS sizes of the 22 MeV/c beam

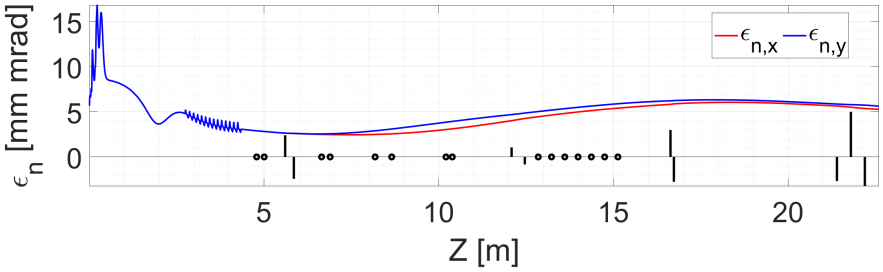

(d) Evolution of the transverse normalized emittances of the 22 MeV/c beam

Figure 4.8: Evolution of the RMS sizes (σ_x, σ_y, σ_z) and the transverse normalized emittances ($\varepsilon_{n,x}$, $\varepsilon_{n,y}$) of the 4 nC, 15 MeV/c beam and the 4 nC, 22 MeV/c beam from the cathode to the undulator entrance. Black bars present applied quadrupole strengths and black circles present zero quadrupole strengths (not use).

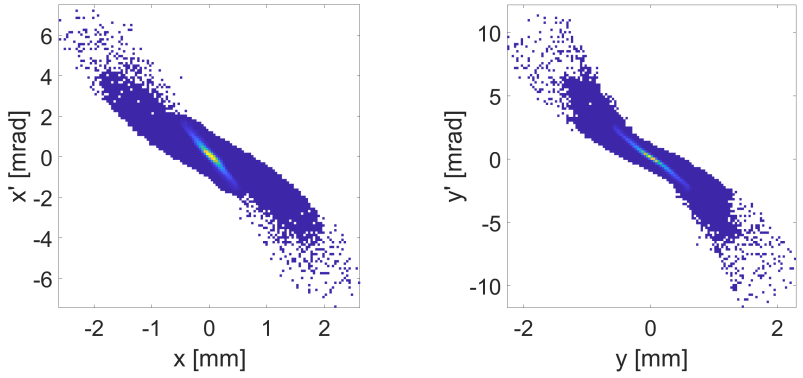

(a) Horizontal phase space

(b) Vertical phase space

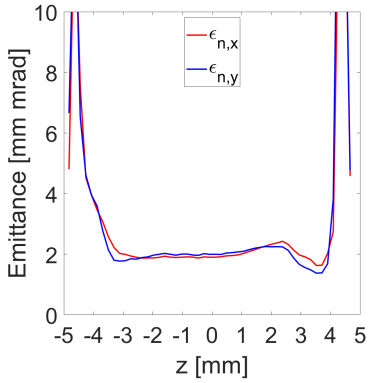

(c) Slice emittance

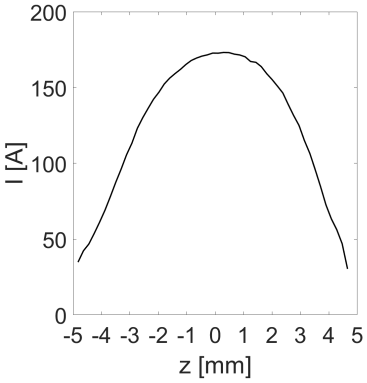

(d) Beam current

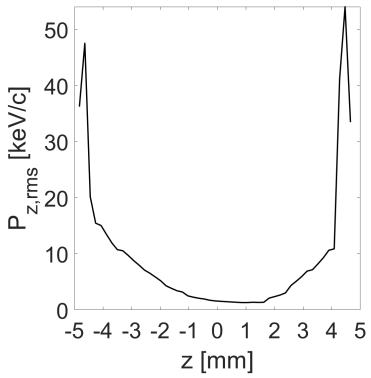

(e) Slice momentum spread

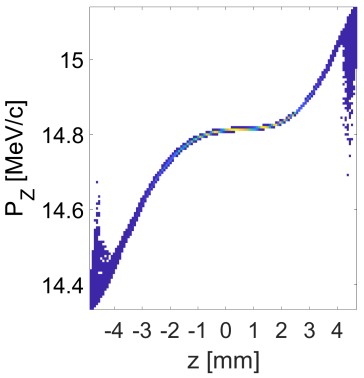

(f) Longitudinal phase space

Figure 4.9: Phase space distributions ans longitudinal slice profiles of the 4 nC, 15 MeV/c beam at the undulator entrance.

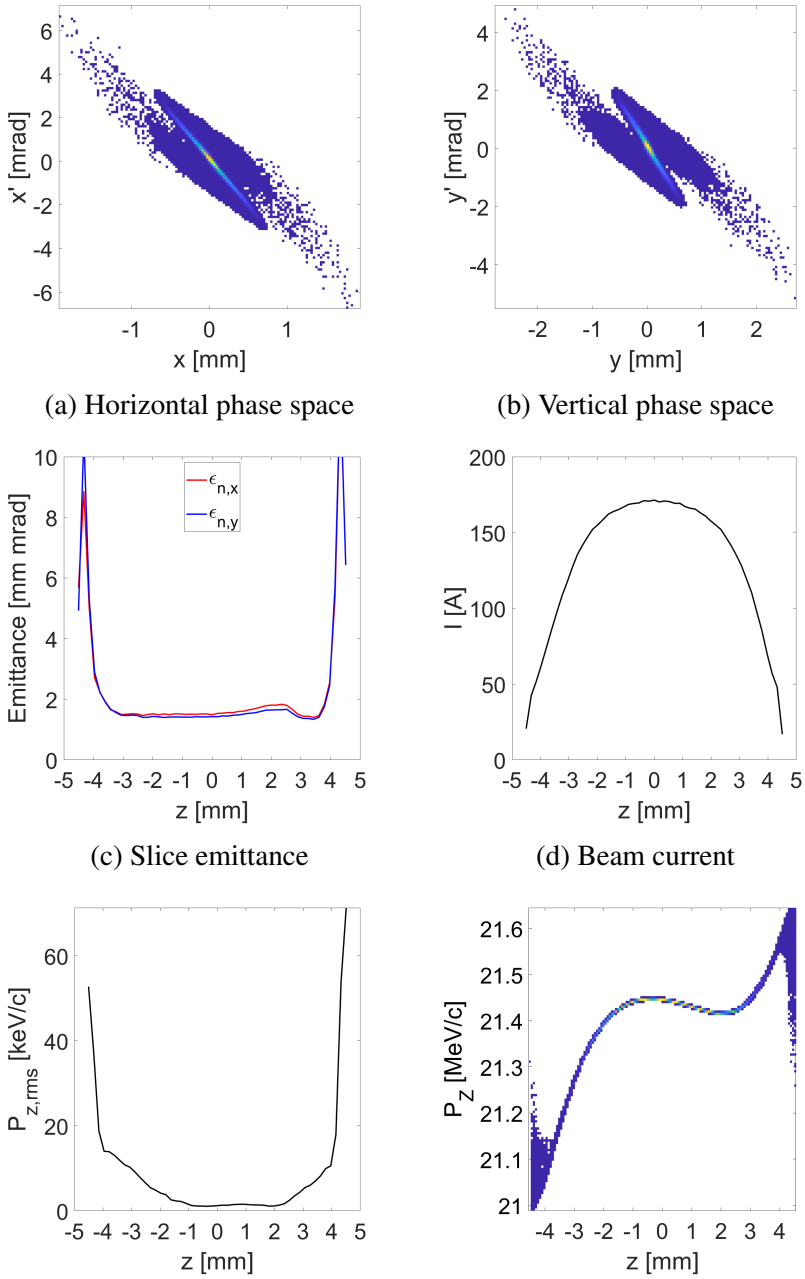

(a) Horizontal phase space

(b) Vertical phase space

(c) Slice emittance

(d) Beam current

(e) Slice momentum spread

(f) Longitudinal phase space

Figure 4.10: Phase space distributions ans longitudinal slice profiles of the 4 nC, 22 MeV/c beam at the undulator entrance.

Table 4.1: The simulated beam parameters at the undulator entrance

Paramaters	15 MeV/c case	22 MeV/c case
Horizontal RMS size (σ_x) [mm]	0.36	0.31
Vertical RMS size (σ_y) [mm]	0.36	0.30
Longitudunal RMS size (σ_z) [mm]	2.29	2.22
Normalized horizontal emittance ($\varepsilon_{n,x}$) [mm mrad]	5.04	5.28
Normalized vertical emittance ($\varepsilon_{n,y}$) [mm mrad]	4.44	5.65
Mean momentum [MeV/c]	14.81	21.44
Uncorrelated momentum spread [keV/c]	129.21	135
Peak current (I) [A]	173	172
Average slice $\varepsilon_{n,x}$ [mm mrad]	2.44	1.81
Average slice $\varepsilon_{n,y}$ [mm mrad]	2.47	1.74
Average slice uncor. momentum spread [keV/c]	5.79	4.90

4.1.4 SASE FEL Simulations

The final step of the S2E simulations is to calculate the FEL radiation from the optimized electron beams. Simulations of the FEL radiation were performed using the Genesis 1.3 code [48]. Several features in the code including time-dependent mode and space-charge effects were used in the simulations. In order to demonstrate the fluctuation due to the SASE FEL process which starts from the shot-noise, the input seed number (IPSEED) for the random particle generator of the Genesis 1.3 code was scanned from 1 to 100.

Parameters and slice profiles of the matched electron beams from the previous section were used as input beams and helical undulator with a period length of 40 mm was used as the FEL radiator. The 15 MeV/c beam (with precise mean momentum of 14.81 MeV/c) was used for the SASE FEL with radiation wavelength of 100 µm which corresponds to the undulator parameter of 1.79. The 22 MeV/c beam (with precise mean momentum of 21.44 MeV/c) was used for the SASE FEL with radiation wavelength of 20 µm which corresponds to the undulator parameter of 0.87.

Figures 4.11 and 4.12 present the pulse energy gain curves along the undulator length for both cases of radiation wavelengths. Grey curves refer to single shot realizations using various seed numbers. The black curves correspond to the average of all one-hundred grey curves while the blue dash-line presents the percentage of standard deviation. Properties of the simulated THz SASE FEL are summarized in Table 4.2. The temporal and spectral profiles of the FEL radiation at saturation position of the 100 µm case are presented in Fig. 4.13. Those of the 20 µm case are presented in Fig. 4.14. Similar to Fig. 4.11 and Fig. 4.12, grey lines refer to single-shot realizations using various IPSEED and the black lines corresponds to their average.

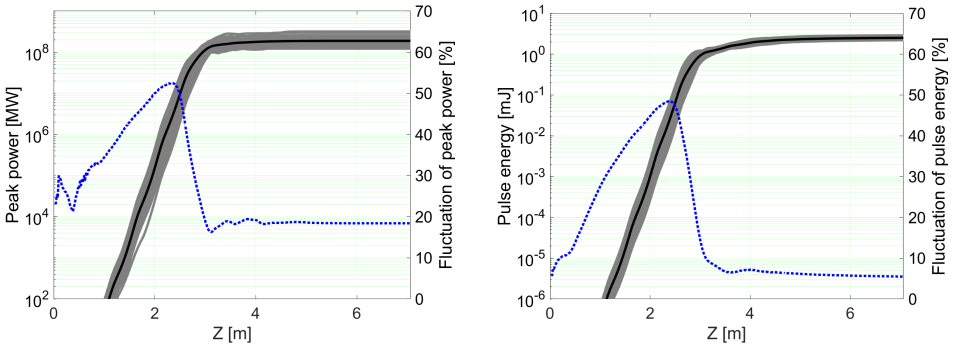

Figure 4.11: Output peak power (left) and pulse energy (right) along the undulator axis for the radiation wavelength of 100 µm using the 4 nC, 15 MeV/c electron beam.

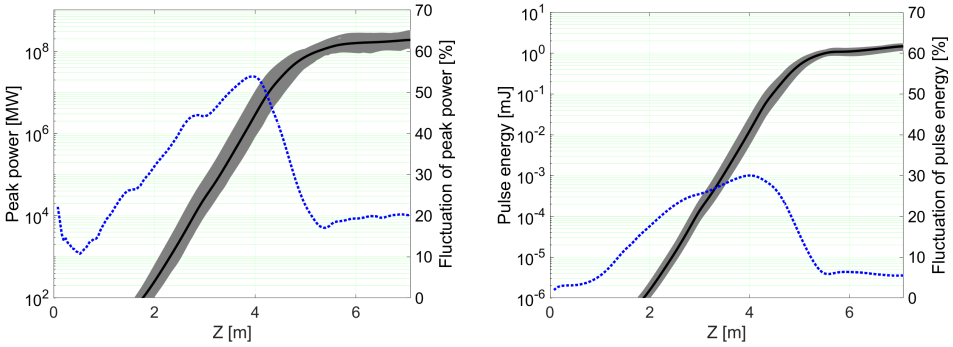

Figure 4.12: Output peak power (left) and pulse energy (right) along the undulator axis for the radiation wavelength of 20 µm using the 4 nC, 22 MeV/c electron beam.

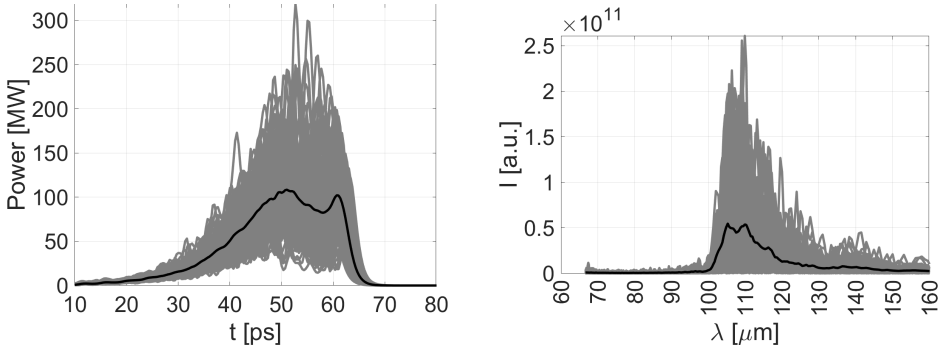

Figure 4.13: Temporal (left) and spectral (right) profiles of the radiation pulses at the undulator exit (Z = 7 m) for the radiation wavelength of 100 µm using 15 MeV/c electron beam.

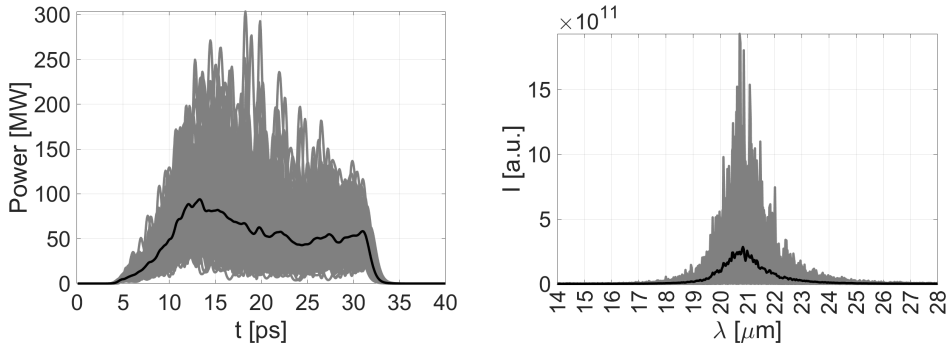

Figure 4.14: Temporal (left) and spectral (right) profiles of the radiation pulses at the undulator exit (Z = 7 m) for the radiation wavelength of 20 µm using 22 MeV/c electron beam.

Table 4.2: The simulated THz SASE FEL radiation properties

Paramaters	100 µm	20 µm
Saturation length [m]	2.94	5.56
Pulse energy at saturation [mJ]	0.78	0.79
Peak power at saturation [MW]	95	93
Pulse energy at the undulator exit [mJ]	**2.51**	**1.46**
Peak power at the undulator exit [MW]	188.7	186.6
Pulse duration (FWHM) [ps]	18	22
Central wavelength	106.4	20.4
Spectral width (FWHM)[µm]	10	0.5

4.1.5 Conclusion Remark for S2E simulations of the SASE FEL

The SASE FEL of a THz source based on the PITZ setup was studied by S2E simulations. An APPLE-II type undulator with a period length of 40 mm in helical mode was assumed to be added to the end of the PITZ beamline and used for producing the FEL radiation. With this undulator parameters, it is possible to produce FEL radiation with wavelengths between 20 µm and 100 µm by using 4 nC electron beams with mean momenta in the range of 15 MeV/c to 22 MeV/c.

Analysis of the FEL parameter space for the radiation wavelengths of 20 µm and 100 µm was done by using the Genesis 1.3 code. It shows that a saturation length up to 6 m can be expected. Beam dynamics simulations using the ASTRA code starting from the cathode to the undulator entrance were performed. The simulations show that the PITZ setup can generate electron beams with reasonable parameters for the SASE FEL and transport the beam to the undulator entrance which was assumed to be located at the end of the current beamline. The FEL simulations using the Genesis 1.3 code based

on the simulated beam parameters show that the FEL process reaches saturation within the undulator length of about 3 m and 6 m for the 100 µm and 20 µm cases, respectively. At the undulator exit, pulse energies of more than 1.4 mJ can be expected from both cases.

The radiation pulses from the SASE FEL have high pulse energies and are suitable to be used for THz field-driven dynamics studies. However, due to the SASE process, the radiation pulses have strong fluctuation which is not suitable for time-resolved dynamics studies. In order to improve the radiation pulse stability, seeding FEL methods have to be implemented. Studies of FEL seeding options will be performed in the future.

4.2 S2E Simulations for the CTR and CDR options

This section presents S2E simulations of the THz CTR and CDR source based on the PITZ accelerator. As described in Chapter 2, the coherent part of CTR relates to the longitudinal form factor which is derived from the Fourier transformation of the longitudinal shape of the electron bunch. Shorter bunch length transforms to a broader form factor in the frequency domain. Therefore, electron bunch compression is necessary to broaden the coherent part of the CTR spectral distribution. Since there is no magnetic bunch compressor in the PITZ beamline, an alternative way to compress the bunch is by mean of velocity bunching.

The velocity bunching process happens when the electron bunch has an energy chirp. The head part of the bunch should have lower energy than the tail part and therefore has slower velocity. When the chirped bunch travels through a drift space, the tail part is moving closer to the head part and therefore bunch compression happens [91]. This energy chirp can be introduced to the bunch by accelerating the bunch off-crest in an accelerating cavity [92]. For this study, the CDS booster cavity was used for this purpose.

This section is organized as follows. First, the important parameters of a typical CTR station are introduced. Then, an overview of the CTR pulse energy based on the conditions of the CTR station and the beamline is calculated. After that, beam dynamics simulations of velocity bunching are presented followed by calculations of the expected CTR and CDR properties. Finally, calculations of CTR generation based on a comb-beam are presented.

4.2.1 Parameters of the CTR station

A screen station named PST.Scr2 located at $Z = 13.038$ m (see Fig. 3.1) was modified to be a CTR station which will be described in detail later in Chapter 6. Figure 4.15 shows a simplified principle layout of the CTR station together with important parameters for the CTR calculations. To simplify the calculation, the radiator is assumed to be a circular metallic screen with a radius of 13.5 mm. The diameter of the circular vacuum window

is 60 mm and the distance between the center of the radiation and the window is 71 mm. This allows an radiation acceptance angle (θ_{max}) of about 0.4 rad.

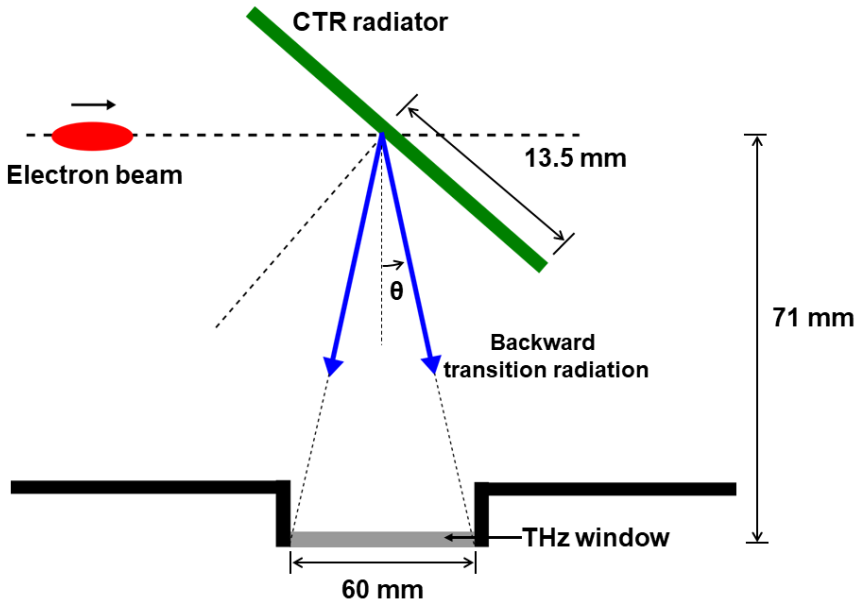

Figure 4.15: Simplified layout of the CTR station.

4.2.2 Calculation of CTR Parameter Space

In order to get an overview of pulse energy of the CTR, the CTR pulse energy for various bunch charges and bunch RMS duration are calculated. The generalized Ginzburg-Frank formula (Eq. (2.28)) was used for the calculations. The electron beam is assumed to have a Gaussian temporal shape and the mean momentum is assumed to be 15 MeV/c ($\gamma = 30$). The total pulse energy is integrated over the frequency range of 0.05 to 5 THz and over the observation angle range of 0 to 0.4 rad. Fig. 4.16 shows the contour plot of the CTR pulse energy in the logarithmic scale as a function of the bunch charge and the bunch RMS duration. The plot shows that a CTR pulse energy of about a few tens μJ is achievable when the electron bunch has a bunch charge of 1 nC and an RMS duration of 500 fs. The plot also shows that the pulse energy is more dependable on the bunch charge than the bunch RMS duration.

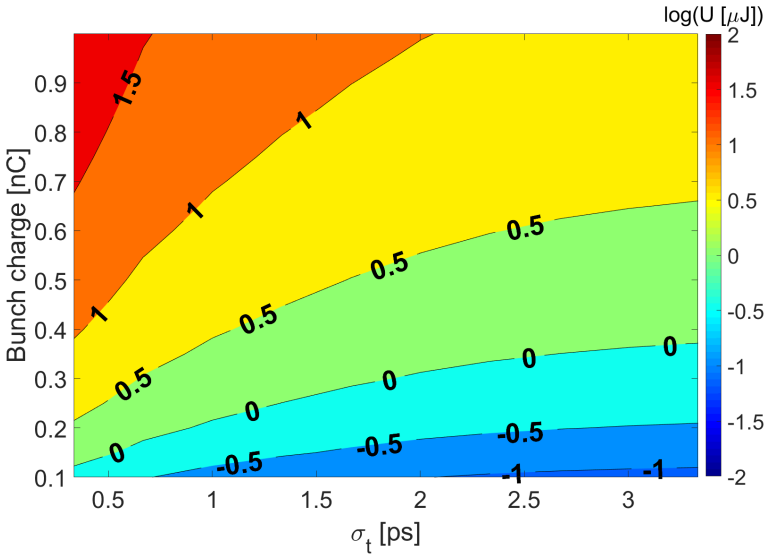

Figure 4.16: Calculated CTR pulse energy as a function of bunch charges and RMS bunch lengths.

4.2.3 Electron Beam Dynamics Simulations

The electron bunch charge needs to be maximized and the bunch length needs to be minimized in order to increase the CTR intensity and to broaden the spectral bandwidth. A popular way to compress a relativistic electron bunch is to use a magnetic chicane [93]. However, the PITZ beamline doesn't have a chicane section that is designed specifically for bunch compression. Another way to compress the bunch is to use velocity bunching. For velocity bunching, the bunch is accelerated off-crest in such a way that the head part of the bunch has energy lower than the tail part after exiting the cavity. Then, the tail part will move closer to the head part when the bunch propagates through a drift distance which means the bunch compression happens [91].

There are two accelerating cavities at PITZ, the RF gun and the CDS booster. Both cavities can be used for bunch compression by velocity bunching. A method to use a photoelectron gun and a buncher cavity to perform linearization of the longitudinal phase space is presented in [94]. However, changing the RF gun phase can have effects on the processes of electron emission for high charge bunch and reduce the emitted bunch charge. Therefore, electron bunch compression for this study was done by using only the CDS booster for velocity bunching.

The ASTRA code was used for tracking the electron beams from the cathode to the CTR station which is located at $Z = 13.038$ m downstream from the cathode as shown in Fig. 4.1. A photocathode laser with Gaussian temporal shape (pulse FWHM duration of 2.43 ps) and bunch charges of 250 pC, 500 pC, 750 pC, and 1 nC were used as input for the

simulations. The RF launch phase in the gun was fixed to Maximum Mean Momentum Gain (MMMG) and only the booster phase was tuned for the velocity bunching. The booster phase was scanned with a step of 10 degrees from 0 to -80 degree with respect to (w.r.t.) the MMMG. For each case of bunch charge, the main solenoid current was tuned to focus the beam on High1.Scr1 (Z = 5.277 m) when the RF launching phases are at MMMG from both cavities. Important input parameters for the ASTRA simulations are listed in table 4.3.

Table 4.3: Input parameters for ASTRA simulations of velocity bunching

Paramaters	**Values**
Laser spot diameter on the cathode [mm]	2
Z_{start} to Z_{end} [m]	0 to 13.038
Bunch charge [pC]	250, 500, 750 and 1000
Peak electric field at the cathode [MV/m]	60.5
Peak electric field in the booster [MV/m]	17.2
Gun phase w.r.t. MMMG phase [degree]	0
Booster phase w.r.t. MMMG phase [degree]	-80 to 0
Main solenoid current [A]	383 to 389

Figure 4.17 presents the simulation results including bunch RMS duration and longitudinal momentum as a function of the booster phase (w.r.t. MMMG) for various bunch charges at Z = 13.038 m. More off-crest of booster phase delivers shorter bunch RMS duration. When the booster phase is at -80 degree, the values of bunch RMS duration are about 1 to 1.5 ps which is reduced by about 50 % from the bunch duration when the booster phase is at 0 degree. The longitudinal momentum of the beam is dependent only on the booster phase and is independent of the bunch charge. With the booster phase of -80 degree, the beam momentum is about 10 MeV/c which is reduced by about 12 MeV/c from the momentum at MMMG phase.

4.2.4 Calculations of CTR

Calculations of CTR based on the simulated bunch properties in Section 4.2.3 and the CTR station parameters in Section 4.2.1 were performed by using the generalized Ginzburg-Frank formula (Eq. (2.28)). Figure 4.18 presents the total CTR pulse energy as a function of booster phase (w.r.t. MMMG) for various bunch charges. The values of pulse energy at each case of bunch charge are almost constant between the phase range of 0 to -50 degree and then slightly increase until -70 degree. At the booster phase of -80 degree, the values of pulse energy are increased significantly. This behavior corresponds to the prediction in Fig. 4.16 where the form factor of the bunch starts to play a role in the total pulse energy when the bunch RMS duration is shorter than 1.5 ps. This means that the coherent part

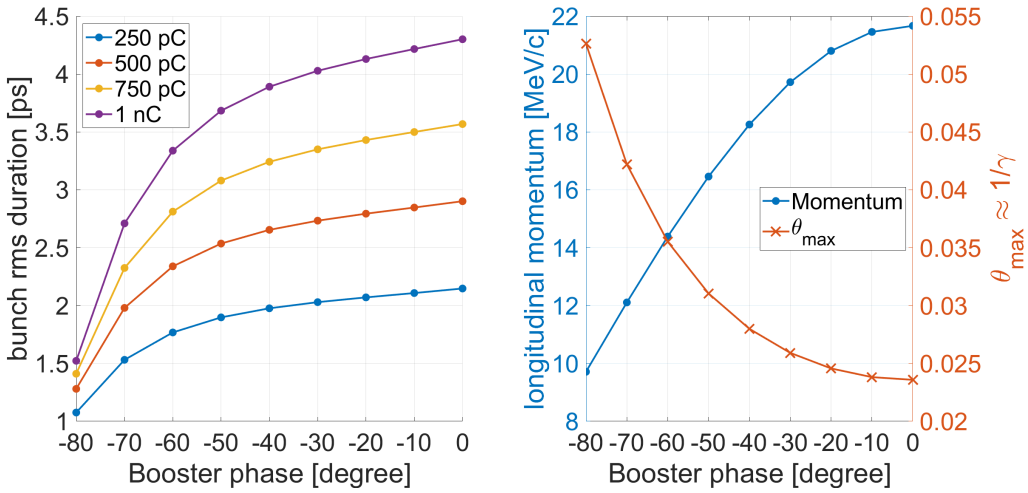

Figure 4.17: Simulated bunch RMS duration (left) and longitudinal momentum (right) as a function of booster phase w.r.t. the MMMG phase for various bunch charges.

of the CTR radiation plays a major contribution to the total pulse energy as revealed in Eq. (2.2).

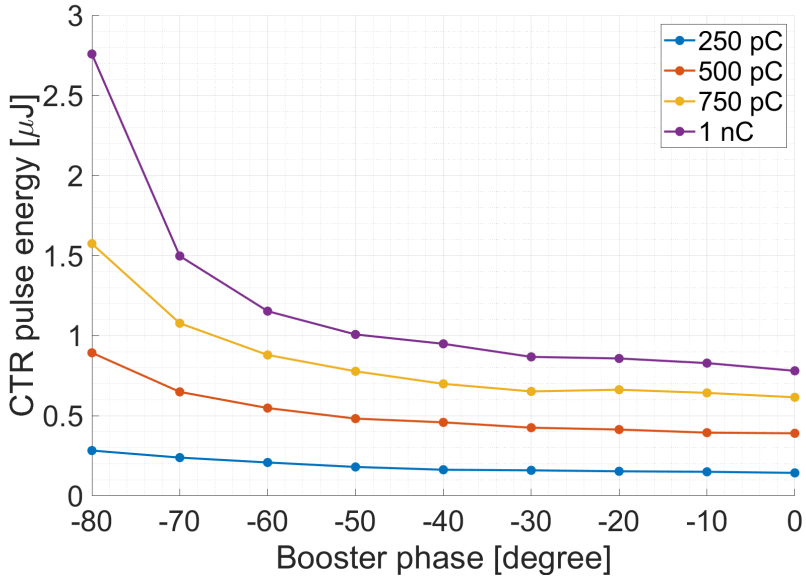

Figure 4.18: Calculated total CTR pulse energy as a function of booster phase w.r.t. the MMMG phase for various bunch charges.

The values of pulse energy are maximized when the booster phase is at -80 degree

(w.r.t. MMMG). Plots of the form factors and spectral distributions at this booster phase for each case of bunch charge are presented in Fig. 4.19. The plots of form factors cover the frequency range up to 0.6 THz. For the plots of spectral distribution, as expected, the spectral distribution of 1 nC has the highest intensity due to the highest bunch charge. The plots also show suppression in the low-frequency part due to finite size of the CTR radiator as predicted by the generalized Ginzburg-Frank formula (Eq. (2.28)).

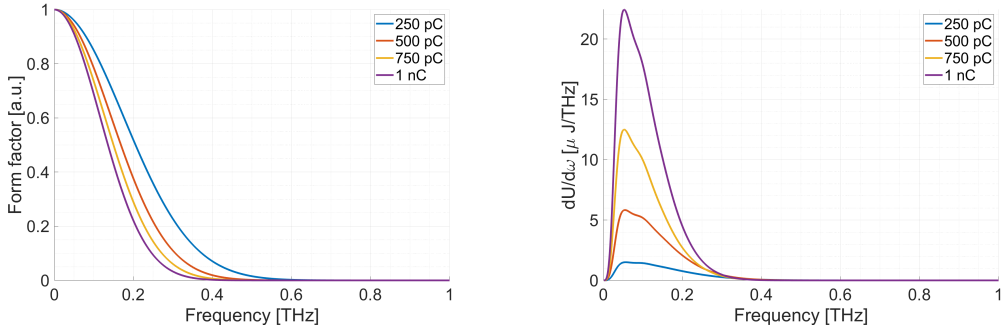

Figure 4.19: Plots of form factors of the bunch (left) and CTR spectral distributions (right) when the booster phase is -80 degree (w.r.t. MMMG) for various bunch charges.

4.2.5 Calculations of CDR

The CDR station setup is similar to the one of the CTR station except the CDR radiator has a circular hole with a diameter of 2 mm as its layout is shown in Fig. 4.20. Calculations of CDR based on the simulated bunch properties in Section 4.2.3 were performed by using Eq. (2.31). Figure 4.21a shows plots of total CDR pulse energy as a function of booster phase w.r.t. the MMMG phase for various bunch charge. The CTR pulse energy for each case of bunch charge and booster phase is also plotted together for comparison. The plots show that CDR pulse energy is only slightly lower than the CTR pulse energy for each case. The corresponding relation can also be observed in plots of spectral distribution as shown in Fig. 4.21b.

4.2.6 S2E simulation of CTR Generated by Using Comb Beam

A comb beam is a beam with a microbunch structure. The form factor of the comb beam shows peaks at higher harmonic frequencies [95]. Therefore, it is interesting to use a comb beam for CTR generation. In this study, the comb beam is produced by a longitudinally modulated photocathode laser pulse. The study process is similar to the S2E simulations using a short Gaussian laser pulse. A comb laser pulse distribution with four micro-pulses as shown in Fig. 4.22a was used as an input laser distribution for the

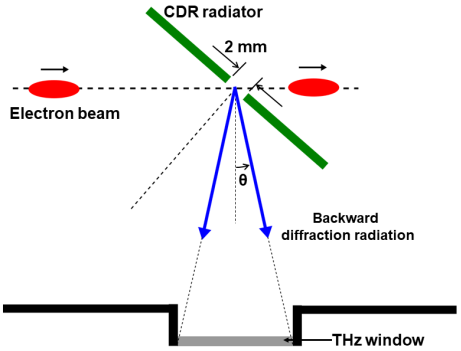

Figure 4.20: Simplified layout of the CDR station.

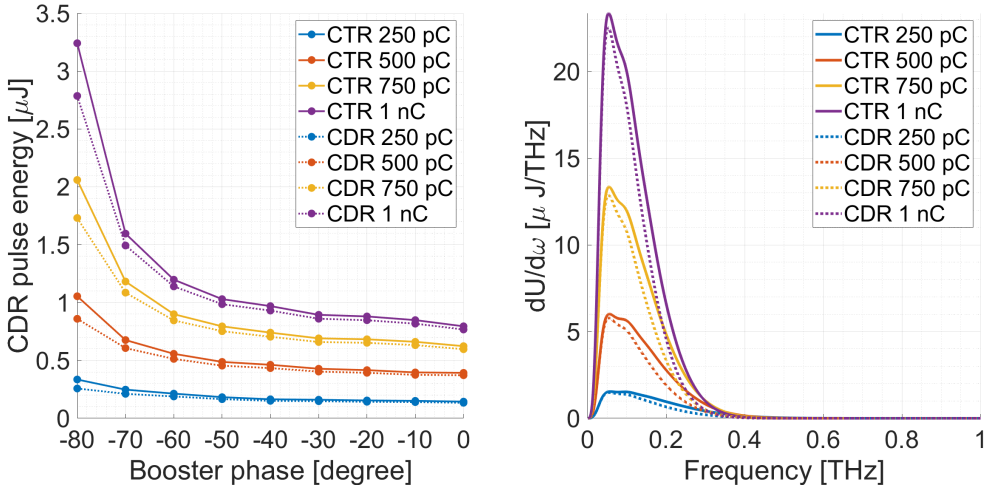

(a) (b)

Figure 4.21: (a) total CTR and CDR pulse energy as a function of booster phase w.r.t. the MMMG phase for various bunch charge. (b) Plots of CTR and CDR spectral distribution when the booster phase is -80 degree (w.r.t. MMMG) for various bunch charges.

ASTRA code. The input parameters in Table 4.3 were also used in this study except the bunch charge was fixed at 1 nC and the booster phase was fixed at the MMMG phase.

The temporal distribution of the simulated 1 nC comb beam at the location of the CTR station is shown in Fig. 4.22b. The distribution of the 1 nC short Gaussian bunch at the booster phase of -80 degree (w.r.t. MMMG) is also shown together for comparison. Current peaks of the comb beam distribution are smeared out by space charge effects and velocity de-bunching due to momentum spread of the electron beam.

Plots of the calculated form factor for the comb bunch and the short Gaussian bunch are presented in Fig. 4.23. The form factor of the comb beam has narrow-band high harmonics frequencies with central frequencies of 0.06 THz, 0.10 THz and 0.15 THz. The plots of spectral distribution in Fig. 4.23 show that the CTR from the comb bunch has lower spectral intensity than the short Gaussian bunch but provides several of narrow-band frequency peaks. By integrating the spectral distribution, the CTR generated by the comb bunch has pulse energy of 1.63 µJ.

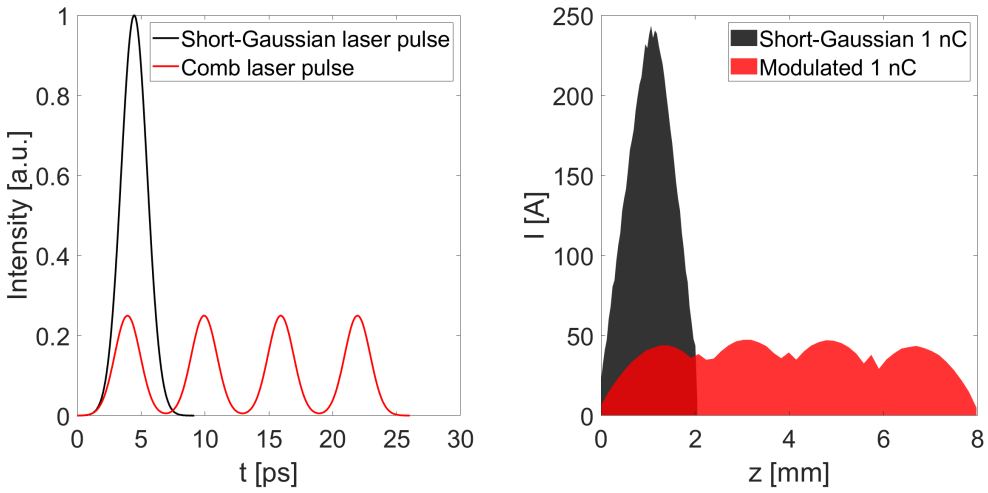

(a) (b)

Figure 4.22: (a) Temporal distribution of the comb photocathode laser pulse with four micro-pulses together with the distribution of the short Gaussian laser pulse. (b) Longitudinal distribution of the 1 nC comb electron bunch (booster phase of MMMG phase) together with the distribution of the 1 nC short Gaussian bunch (booster phase of -80 degree w.r.t. MMMG phase) at Z = 13.038 m.

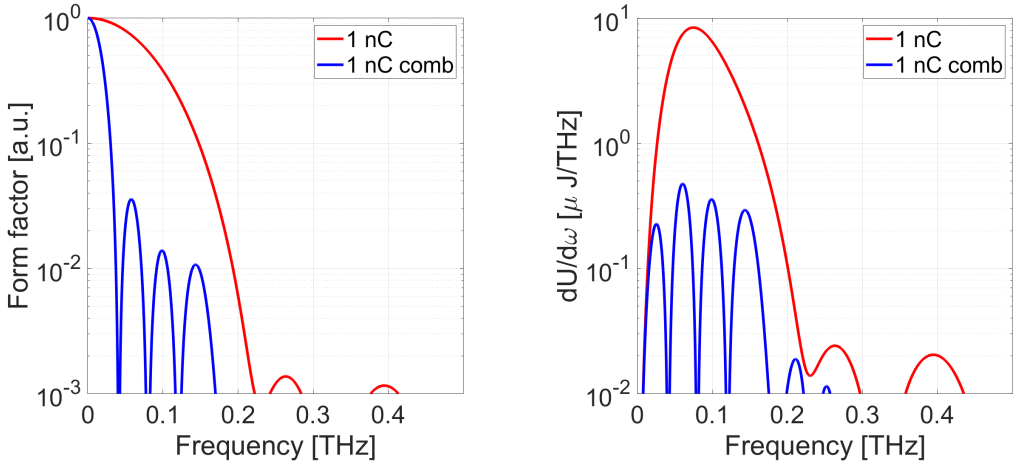

Figure 4.23: Plots of form factor (left) and spectral distribution (right) of CTR for the comb bunch and CTR for the short Gaussian bunch.

4.2.7 Concluding Remarks for S2E Simulations of the CTR and CDR Options

S2E simulations of the THz radiation generated by means of CTR and CDR were performed. By using a short Gaussian photocathode laser pulse and an electron bunch charge up to 1 nC, a CTR radiation pulse energy up to 10 µJ and frequencies covering up to 0.2 THz can be expected. CDR calculations for several cases were also performed. The pulse energy is slightly lower than for the CTR case. S2E simulations of CTR generated by using a comb beam were also performed. The spectral distribution of the comb bunch has several narrow-band frequency peaks.

As seen from the simulation results, the RMS bunch duration can only be compressed down to about 1 ps by velocity bunching using the CDS booster. In order to compress the bunch more, another approach is needed like using a chicane bunch compressor, using shorter photocathode pulses or using an additional buncher cavity.

Chapter 5

Experimental Optimization and Characterization of Electron Beams for Generating the SASE FEL Radiation

In Chapter 4, start-to-end (S2E) simulations of the THz SASE FEL based on the APPLE-II undulator in its helical mode and the PITZ accelerator for a radiation wavelength of 20 µm and 100 µm were performed. In order to demonstrate that such electron beams with the required parameters for the SASE FEL radiation can be obtained practically, experimental optimization and characterization of electron beams with bunch charges of 4 nC for such purpose were performed.

This chapter presents details of electron beam measurements, follow-up beam dynamics simulations, and SASE FEL simulations for these beam parameters. Sections 5.1 to 5.6 present step-by-step the 4 nC electron beam characterization. Then, Section 5.7 presents the follow-up beam dynamics simulations with the same machine conditions as used in the measurements. Finally, details of the SASE FEL simulations based on the measured beam parameters are discussed in Section 5.8.

5.1 Photocathode Laser Characterization

The electron beam optimization tried to follow the strategy established in Chapter 4. However, the PC laser with a flattop temporal shape used in Chapter 4 was not available during the experiments. Therefore, a Gaussian temporal shape with ∼11 ps FWHM pulse duration as its measured profile is shown in Fig. 5.1 was used instead. Initially, the photocathode (PC) laser with a diameter of 5 mm on the cathode was used. However, its transverse distribution measured by the virtual cathode camera (VC2) was extremely non-uniform and radially asymmetric. Therefore, the PC laser diameter on the photocathode was reduced to 3.7 mm for a reasonable transverse distribution. The PC laser transverse

distribution with a diameter of 3.7 mm measured by the VC2 camera is shown in Fig. 5.2.

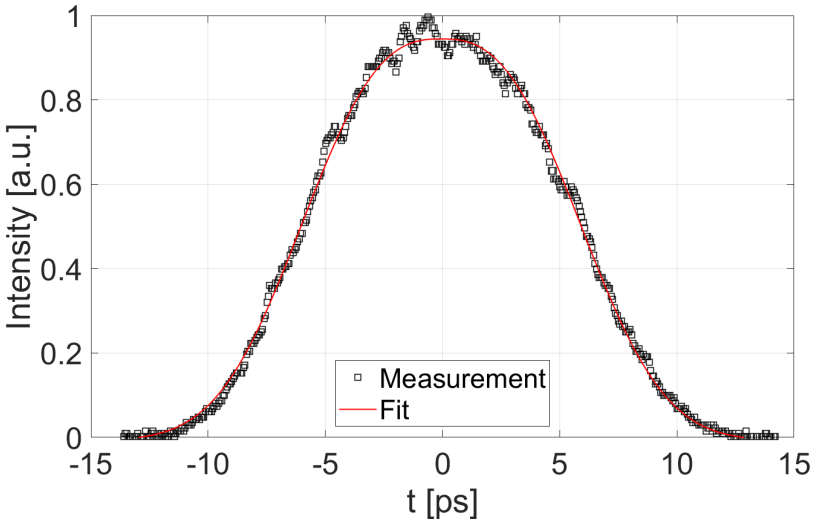

Figure 5.1: Longitudinal PC laser distribution measured by OSS. The profile is Gaussian with a FWHM pulse duration of 11 ps.

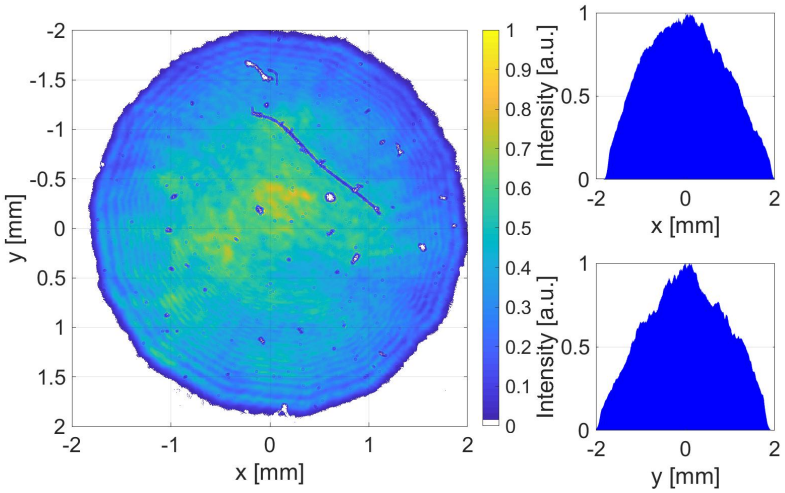

Figure 5.2: Transverse PC laser distribution measured by the virtual cathode camera (VC2) when the laser BSA was set to 3.7 mm. The right plots present projection histograms of each transverse axis. The black hair-line and dots in the left plot are dust in the VC2 optics.

5.2 Charge Production

The emission area homogeneity plays a significant role in electron beam generation and thus, in the measured electron beam properties, especially the beam emittance as studied experimentally in [16]. Therefore, it is important to know the status of the emission area homogeneity by measuring the quantum efficiency (QE) map of the photocathode. The QE map was measured by scanning a laser spot with a diameter of 0.2 mm with 0.2 mm steps around the cathode area. Note that the gun was run with 6.5 MW RF peak power (equivalent to a peak electric field at the cathode of 60.5 MV/m) and the RF phase was set to about the MMMG phase. The measured QE map is shown in Fig. 5.3. The cathode has a QE in-homogeneity especially in the rim area. The green circle presents the border within the photocathode laser with a diameter of 3.7 mm illuminates on the cathode. The QE in-homogeneity is also visible in this area. It increases from about 10 % at the center to about 15 - 20 % at the rim.

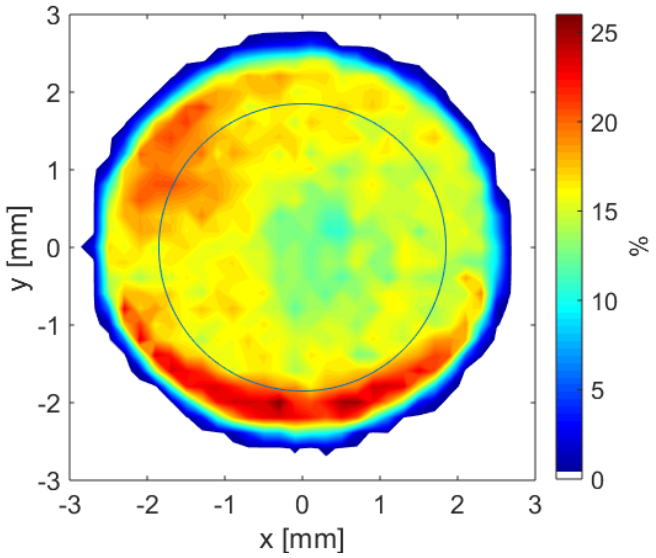

Figure 5.3: QE map of the Cs2Te photocathode.

Another important issue for charge production is the dependence of the produced charge on the laser pulse energy. This issue is important to determine the emission model used in beam dynamics simulations. An inaccurate model can significantly cause discrepancies between simulated and measured beam parameters.

Unfortunately, a dependence of the produced charge on the laser pulse energy was not measured with the laser diameter of 3.7 mm but with 3.5 mm instead. However, the dependencies of the produced charge on the laser pulse energy for both cases are not expected to be much different. Further investigations will be done in follow-up simulations.

Figure 5.4 shows the produced charge measurement as a function of the laser transmission using the laser diameter of 3.5 mm. The red dashed line shows a linear fit which is expected in the quantum efficiency limited emission regime [96]. This linear dependence happens only at low laser pulse energies (i.e., low transmission through the attenuator of the laser system). In order to produce the beam with a 4 nC bunch charge, the laser transmission of about 21 % is needed. It is obviously in the saturation regime of the emission curve.

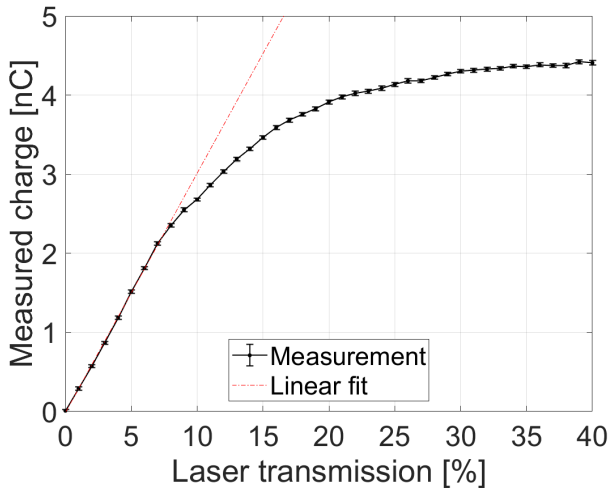

Figure 5.4: Measured charge using Low.ICT1 as a function of laser transmission. A laser spot diameter of 3.5 mm was used for this measurement.

5.3 Beam Momentum Measurement

LEDA is used for measurements of electron beam momentum after the gun and HEDA1 is used for measurements of the electron beam momentum after the booster. As in Chapter 4, two electron beam momenta after the booster are expected, 15 MeV/c and 22 MeV/c. The gun was run with its maximum RF peak power of 6.5 MW (equivalent to a peak electric field at the cathode of 60.5 MV/m). The MMMG phase of the gun was derived by measuring the average beam momentum using LEDA as a function of the gun phase. The measurement results are shown in Fig. 5.5a. The plot shows that the MMMG phase is at the gun phase setpoint of −131 degree. The measured momentum distribution at the MMMG phase is shown in Fig. 5.5b. At the MMMG phase, the average momentum is 6.46 MeV/c and the momentum spread is 54.1 keV/c.

For the 15 MeV/c beam, the booster was run with an RF peak power of 1 MW (equivalent to a peak electric field of 10 MV/m). The average beam momentum and the momentum spread were measured as a function of the booster phase by using HEDA1 and

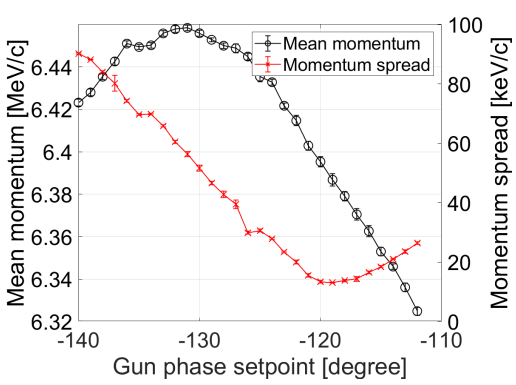

(a) Measurements of mean momentum and momentum spread as a function of the gun phase

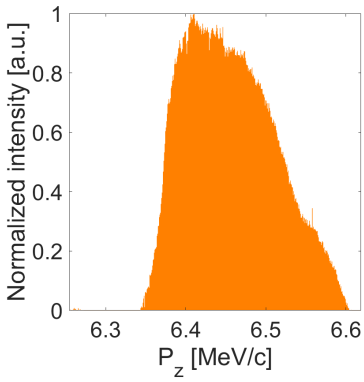

(b) Measured momentum distribution at the gun phase setpoint of −131 degree (MMMG phase)

Figure 5.5: Momentum measurement using LEDA. The gun RF peak power is 6.5 MW.

the measurement results are presented in Fig. 5.6a. The minimum momentum spread (MMS) phase is at the booster phase setpoint of -148 degree. The measured momentum at this phase setpoint is shown in Fig. 5.6b. At the MMS phase, the average momentum is 15.15 MeV/c and the momentum spread is 65 keV/c.

For the 22 MeV/c beam, the booster was run with RF peak power of 3 MW (equivalent to peak electric field of 17.4 MV/m). The measurement procedure is similar to the case of the 15 MeV/c beam. Results of the booster phase scan are shown in Fig. 5.7a and the MMS phase is at the booster phase setpoint of -164 degree. The measured momentum at this phase setpoint is shown in Fig. 5.7b. At this MMS phase, the average momentum is 21.72 MeV/c and the momentum spread is 84.6 keV/c.

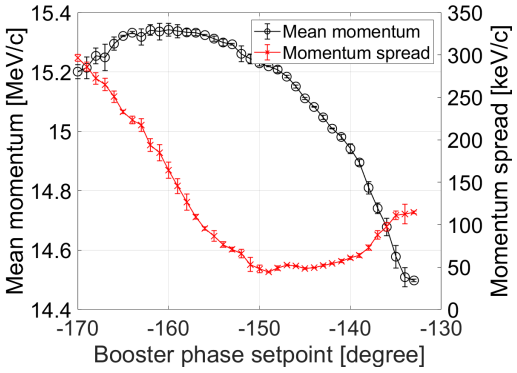

(a) Measurements of mean momentum and momentum spread as a function of the booster phase

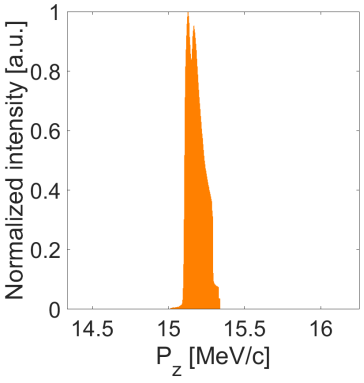

(b) Measured momentum distribution at the MMS phase

Figure 5.6: Momentum measurement using HEDA1. The booster RF peak power is 1 MW.

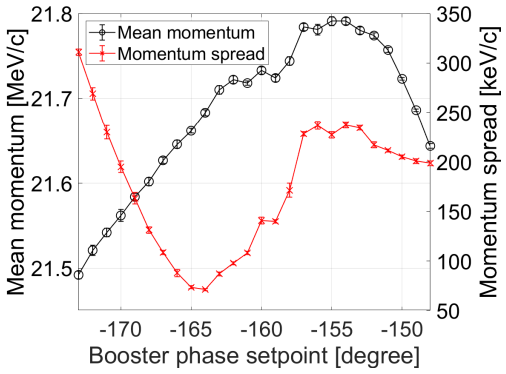

(a) Measurements of mean momentum and momentum spread as a function of the booster phase

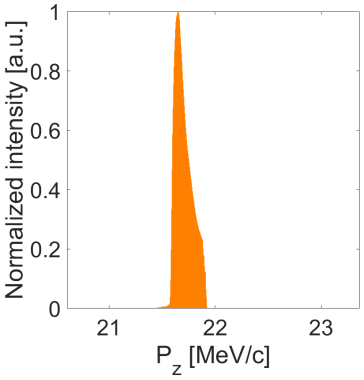

(b) Measured momentum distribution at the MMS phase

Figure 5.7: Momentum measurement using HEDA1. The booster RF peak power is 3 MW.

5.4 Bunch Current Profiles

5.4.1 Bunch Length Measurement Procedure

The bunch length can be measured using the RF deflector (TDS). When the electron beam passes through the TDS, the electrons are deflected vertically in linear dependence on their longitudinal coordinates within the bunch. The deflected electrons travel further through a drift space and are finally imaged on an observation screen. The vertical position on the screen is proportional to the longitudinal position within the bunch as:

$$y = S \cdot z \quad , \tag{5.1}$$

where y is the vertical position, z is the longitudinal position and S is the TDS shear parameter [85]. The S parameter can be measured experimentally by performing a linear fit of the measured vertical mean position as a function of the varied TDS phase. The linear fit will result in the S parameter as [85]:

$$S = K \frac{360^\circ \cdot f}{\beta c} \quad , \tag{5.2}$$

where K is the first order term (or slope) of the linear fit, and f is the RF frequency of the TDS.

5.4.2 Current Profile Measurements

The current profiles of the optimized beam are measured by using the TDS. Two quadrupole magnets, HIGH1.Q9 and HIGH1.Q10, are used for the beam focusing. The screen station PST.Scr2 (located at Z = 13.04 m) is used for monitoring the streaked beam. The principle and procedure of current profile measurement at PITZ are described in Section 5.4.1.

Figure 5.8 shows examples of the beam distributions while the TDS is switched off and on at PST.Scr2. If the TDS phase is set to the zero-crossing phase, therefore, the beam is streaked vertically while the beam center is not moved. Then by scanning the TDS phase, the beam center is moved accordingly. Plots of measured beam center position as a function of the TDS phase are presented in Fig. 5.9. By fitting and using Eq. (5.2), the shear parameters for the cases of 15 MeV/c and 22 MeV/c are 2.98 and 2.96, respectively.

The measured current distributions derived from the streaked profiles and the shear parameters are presented in Figure 5.10. For the case of 15 MeV/c beam, the measured FWHM bunch length is 24.50 ps with the measurement resolution of 2.23 ps and the peak current of 160 A. For the case of 22 MeV/c beam, the measured FWHM bunch length is 17.23 ps with the measurement resolution of 1.27 ps and the peak current of 230 A.

The measured profile of the 22 MeV/c case has a shorter bunch length compared to the measured profile of the 15 MeV/c case. A possible reason for this result is that space charge effects have a stronger influence on the lower energy beam.

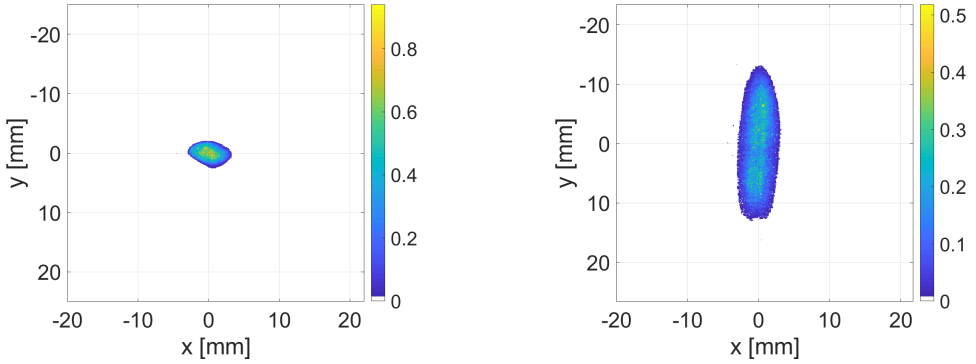

Figure 5.8: Example of the beam profiles at PST.Scr2 while the TDS is switched off (left) and switched on (right) .

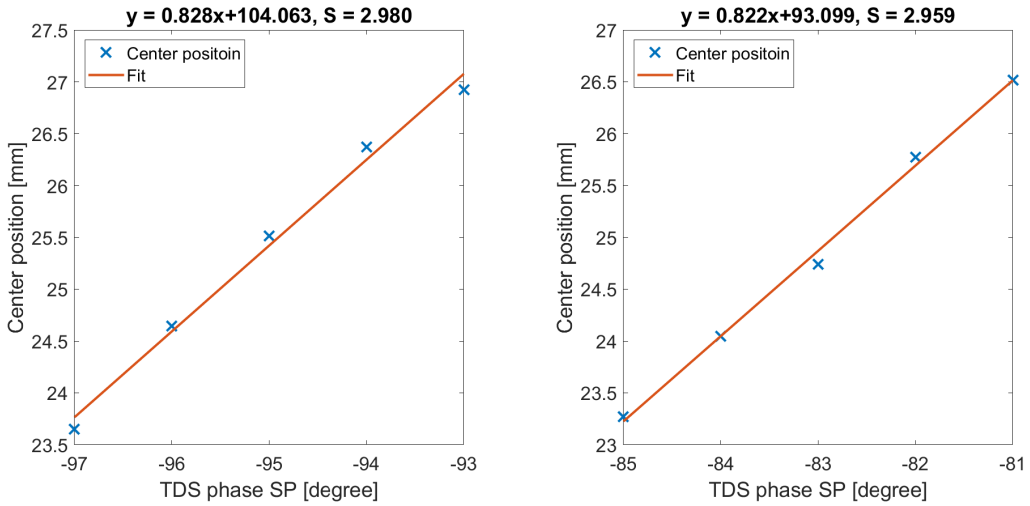

Figure 5.9: Measured center positions of the beam at PST.Scr2 as a function of TDS phase setpoint for the 15 MeV/c case (left) and the 22 MeV/c case (right). The red lines are linear fits to the data.

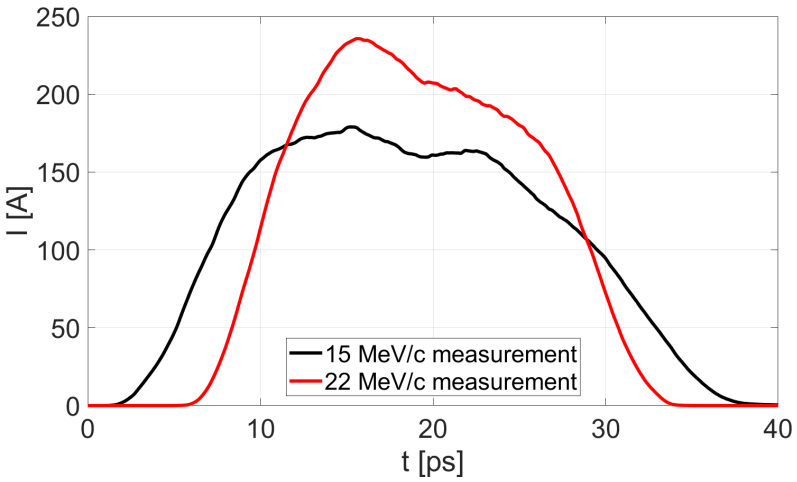

Figure 5.10: Measured beam current distributions of the optimized 4 nC beams with the beam momenta of 15 MeV/c (the black line) and 22 MeV/c (the red line).

5.5 Longitudinal Phase Space Measurement

The longitudinal phase space measurement is similar to the bunch length measurement, but the observation screen is placed downstream from a horizontal bending magnet (the first dipole magnet of HEDA2). The deflected bunch is transported through a dipole magnet called Disp3.D1 and then is imaged on the observation screen Disp3.Scr1. Two quadrupole magnets, PST.QT5 and PST.QT6, were used for transporting the streaked beam from TDS to HEDA2. The distance from the TDS entrance to the dipole entrance is 6.4 m and the distance from the dipole exit to the observation screen is 0.7 m. The dipole magnet has a bending radius of 0.6 m and a bending angle of 60°.

Disp3.D1 of HEDA2 bends the beam horizontally. Therefore the longitudinal momentum distribution is imaged as the horizontal projection of the image on Disp3.Scr1. The beam deflected by TDS shows longitudinal position distribution as the vertical projection of the image. Therefore, the beam image on Disp3.Scr1 is the longitudinal phase space of the beam. Figure 5.11 presents the measured longitudinal phase spaces for the cases of 15 MeV/c and 22 MeV/c. Both longitudinal phase spaces show strong curvature which means there are higher-order space-charge effects on the bunches.

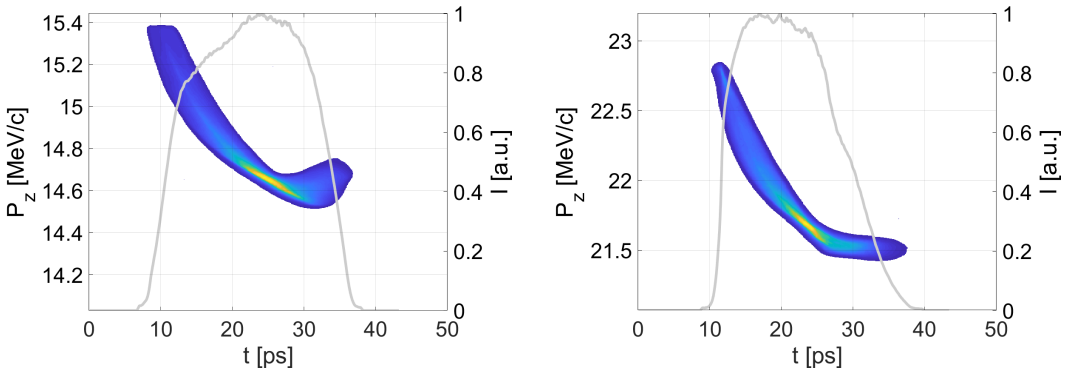

Figure 5.11: The measured longitudinal phase space of the 15 MeV/c beam (left) and the 22 MeV/c beam (right). The gray lines present projections on the time scale of each distribution.

Evaluation of Slice Momentum Spread

The slice momentum spread can be derived from the measured LPS by slicing the LPS into slices with equal time (or position) step size, then calculating the momentum spread of each slice. The number of slices is selected to be 9 slices in order to be consistent with the number of slices from slice emittance measurements (next section). The measured profiles of slice momentum spread are presented in Fig. 5.12. The Average slice mo-

mentum spreads calculated by weighting with the current distribution are 20 keV/c and 39 keV/c for the cases of 15 MeV/c and 22 MeV/c, respectively.

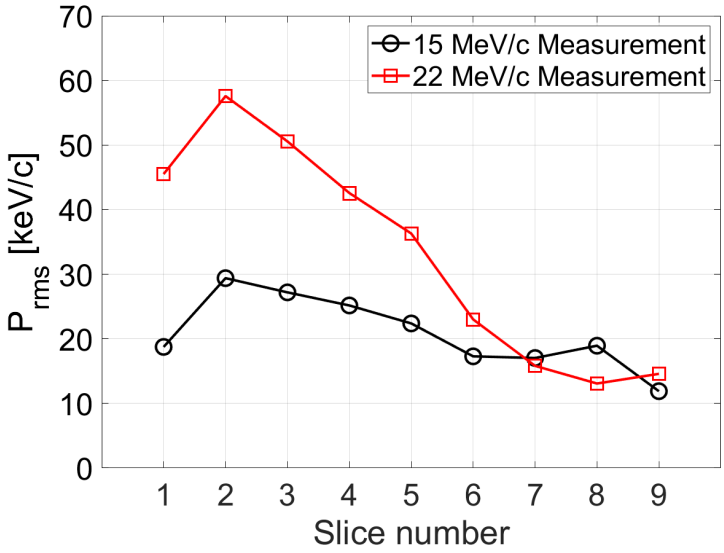

Figure 5.12: Slice momentum spread profiles of the optimized beams which are evaluated from the distributions in Fig. 5.11.

5.6 Transverse emittance Measurements

5.6.1 Emittance Measurement Using Slit Scan Technique

Review of Single Slit Scan Technique Procedure

The emittance measurement systems (EMSYs) are designed for transverse emittance measurement by using the slit-scan technique. Each EMSY consists of horizontal and vertical actuators supplied with a YAG screen and slit masks made of 1 mm thick tungsten. There are slit masks with two gap sizes: 10 µm and 50 µm. Each EMSY has two actuators: one moving horizontally and another one moving vertically. The slit mask converts a space-charge dominated electron beam into an emittance dominated beamlet which is characterized at a screen downstream. The EMSY1 station (HIGH1.Scr1) which is located at Z = 5.277 m was used for transverse emittance measurements in this thesis. Only the slit masks with an opening width of 10 µm were used during the measurements. The beamlets from EMSY1 are characterized at HIGH1.Scr4 which is located 3.133 m downstream from the slit. By moving the slit mask transversely over the beam spot, one obtains local divergence profiles of the electron beam, yielding transverse phase space.

The transverse phase space (x, x') can be reconstructed from the slit-scan data and the geometrical emittance ($\varepsilon_{\mathrm{geo},x}$) can be calculated as

$$\varepsilon_{\mathrm{geo},x} = \sqrt{\langle x^2 \rangle \langle x'^2 \rangle - \langle x x' \rangle^2}. \tag{5.3}$$

By assuming that tails of the phase space distribution are lost during the measurement, due to low particle density and limited sensitivity of the screen, the measured emittance can be scaled to the 100 % emittance by using the scaling factor $\frac{\sigma_x}{\sqrt{\langle x^2 \rangle}}$ where σ_x is the RMS size of the whole beam measured by a YAG screen at the EMSY1 position and $\sqrt{\langle x \rangle^2}$ is the RMS size of the beam obtained from the slit scan.

The 100 % RMS normalized projected emittance used at PITZ can be defined by using Eq. (5.3) with the scaling factor and can be expressed in the form

$$\varepsilon_{n,x} = \beta\gamma \frac{\sigma_x}{\sqrt{\langle x^2 \rangle}} \varepsilon_{\mathrm{geo},x}, \tag{5.4}$$

where the factor $\beta = \sqrt{\gamma^2 - 1}$ can be calculated from the relativistic Lorentz factor γ of the beam. More details on this emittance measurement procedure at PITZ can be found in [86].

Optimization of Transverse Projected Emittance

The transverse projected emittances were measured by using EMSY1. Machine and electron beam parameters used during the measurements are listed in Table 5.1. The first step of the optimization for minimizing the projected transverse emittance was done by measuring emittance as a function of the main solenoid current. The measured results of this dependence are presented in Figure 5.13. The measured vertical emittances are higher than the measured horizontal emittances, especially for the case of the 15 MeV/c beam. This difference is possibly caused by the impact of multipole fields inside the gun cavity system as investigated in [97].

Table 5.1: Machine and electron beam parameters used during the experimental optimization of transverse projected emittance

Parameters	**Values**
PC laser pulse duration [ps]	11 (FWHM), gaussian shape
PC laser diameter on the cathode [mm]	3.7
Peak electric field at the cathode [MV/m]	60.5
Peak electric field in the booster [MV/m]	10 and 17.4
Gun phase w.r.t. MMMG [degree]	0
Booster phase [degree]	for minimum momentum spread
Bunch charge [nC]	4

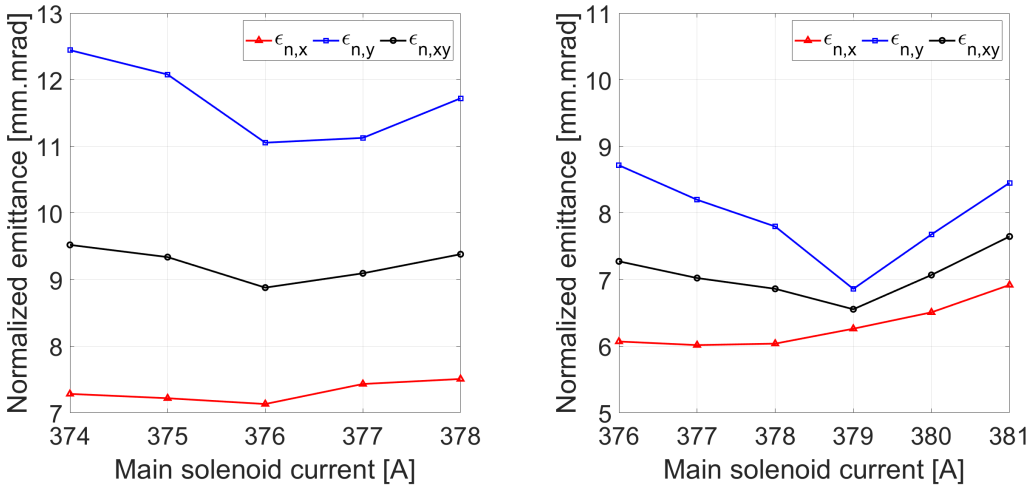

Figure 5.13: Measured transverse normalized emittances as a function of the main solenoid current for the case of 15 MeV/c (left) and for the case of 22 MeV/c (right). Other relevant machine and beam parameters are listed in Table 5.1.

The second step of optimization was to use the quadrupole magnets installed at the gun exit to symmetrize the optimized horizontal and vertical emittances from the first step. The results of projected emittance optimizations are summarized in Table 5.2. The optimized transverse phase spaces measured by EMSY1 for the case of 15 MeV/c and 22 MeV/c are presented in Fig. 5.14 and Fig. 5.15, respectively. The measured emittances for the case of 15 MeV/c still show a strong x-y asymmetry which cannot be improved even when the gun quadrupole magnets were used.

Table 5.2: Results of transverse normalized projected emittance of the 4 nC beams using the solenoid current scan and gun quadrupoles. Other relevant machine and beam parameters are listed in Table 5.1.

Parameters	15 MeV/c	22 MeV/c
I_{m} for optimized emittance [A]	376	379
σ_x for optimized emittance [mm]	1.657	0.865
σ_y for optimized emittance [mm]	1.633	0.930
σ_{xy} for optimized emittance [mm]	1.645	0.897
Optimized $\varepsilon_{\mathrm{n,x}}$ [mm.mrad]	8.640 ± 0.079	6.400 ± 0.050
Optimized $\varepsilon_{\mathrm{n,y}}$ [mm.mrad]	11.049 ± 0.039	6.282 ± 0.050
Optimized $\varepsilon_{\mathrm{n,xy}}$ [mm.mrad]	9.770 ± 0.062	6.344 ± 0.036

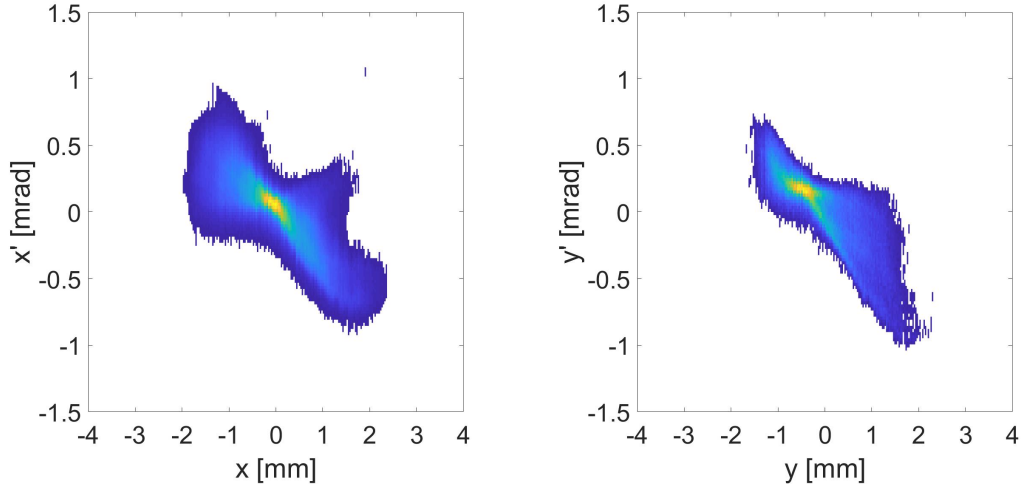

Figure 5.14: Measured horizontal (left) and vertical (right) transverse phase spaces at Z =5.277 m for the case of 15 MeV/c beam as shown in Table 5.2.

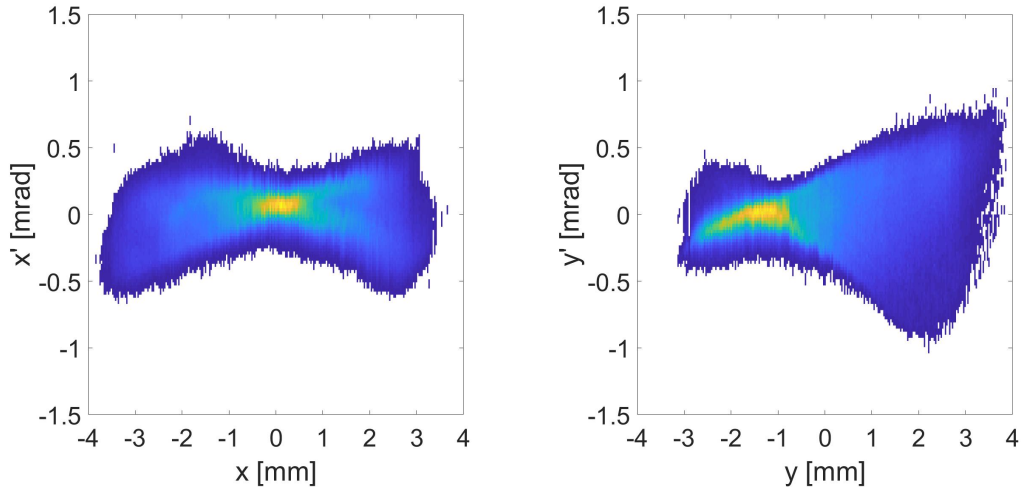

Figure 5.15: Measured horizontal (left) and vertical (right) transverse phase spaces at Z =5.277 m for the case of 22 MeV/c beam as shown in Table 5.2.

5.6.2 Emittance Measurement Using Quadrupole Scan Technique

Quadrupole Scan Technique

The principle of emittance measurement using the quadrupole scan technique is described in [98, 99]. The beam matrix (see Appendix A) in terms of statistical properties of the horizontal phase space can be expressed by

$$\sigma = \begin{pmatrix} \sigma_{11} & \sigma_{12} \\ \sigma_{21} & \sigma_{22} \end{pmatrix} = \varepsilon \begin{pmatrix} \beta & -\alpha \\ -\alpha & \gamma \end{pmatrix} = \begin{pmatrix} \langle x^2 \rangle & \langle xx' \rangle \\ \langle xx' \rangle & \langle x'^2 \rangle \end{pmatrix}. \tag{5.5}$$

Definitions of all variables can be found in Appendix A.

Transformation of the beam matrix transported from position z_0 to position z_f can be derived by

$$\sigma_{z_f} = \mathscr{R}\sigma_{z_0}\mathscr{R}^T, \tag{5.6}$$

where $\mathscr{R}$ is the transport matrix and $\mathscr{R}^T$ is its transpose [83]. According to Eq. (5.5) and Eq. (5.6). The term $\langle x^2 \rangle$, which is the square of the RMS beam size, can be written as

$$\langle x_f^2 \rangle = R_{11}^2 \langle x_0^2 \rangle + R_{12}^2 \langle x_0'^2 \rangle + 2R_{11}R_{12} \langle x_0 x_0' \rangle. \tag{5.7}$$

By applying different transformation matrices $\mathscr{R}$ and using the chi-square (χ^2) method for fitting of the measured data, the elements of the beam matrix at the initial position can be derived by solving the following matrix equation

$$\mathbf{a} = (\mathbf{B}^T\mathbf{B})^{-1}\mathbf{B}^T\mathbf{b}. \tag{5.8}$$

Here

$$\mathbf{a} = \begin{pmatrix} \langle x_0^2 \rangle \\ \langle x_0 x_0' \rangle \\ \langle x_0'^2 \rangle \end{pmatrix}, \tag{5.9}$$

$$\mathbf{b} = \begin{pmatrix} \frac{\langle x_{(1)}^2 \rangle}{\sigma_{\langle x_{(1)}^2 \rangle}} \\ \frac{\langle x_{(2)}^2 \rangle}{\sigma_{\langle x_{(2)}^2 \rangle}} \\ \vdots \\ \frac{\langle x_{(n)}^2 \rangle}{\sigma_{\langle x_{(n)}^2 \rangle}} \end{pmatrix} \tag{5.10}$$

and

$$\mathbf{B} = \begin{pmatrix} \frac{R_{11}^{(1)^2}}{\sigma_{\left\langle x_{(1)}^2 \right\rangle}} & \frac{2R_{11}^{(1)}R_{12}^{(1)}}{\sigma_{\left\langle x_{(1)}^2 \right\rangle}} & \frac{R_{12}^{(1)^2}}{\sigma_{\left\langle x_{(1)}^2 \right\rangle}} \\ \frac{R_{11}^{(2)^2}}{\sigma_{\left\langle x_{(2)}^2 \right\rangle}} & \frac{2R_{11}^{(2)}R_{12}^{(2)}}{\sigma_{\left\langle x_{(2)}^2 \right\rangle}} & \frac{R_{12}^{(2)^2}}{\sigma_{\left\langle x_{(2)}^2 \right\rangle}} \\ \vdots & \vdots & \vdots \\ \frac{R_{11}^{(n)^2}}{\sigma_{\left\langle x_{(n)}^2 \right\rangle}} & \frac{2R_{11}^{(n)}R_{12}^{(n)}}{\sigma_{\left\langle x_{(n)}^2 \right\rangle}} & \frac{R_{12}^{(n)^2}}{\sigma_{\left\langle x_{(n)}^2 \right\rangle}} \end{pmatrix}, \tag{5.11}$$

where $\sigma_{\left\langle x_{(n)}^2 \right\rangle}$ is the error of $\left\langle x_{(n)}^2 \right\rangle$ in the n^{th} measurement. By solving Eq. (5.8), the geometrical horizontal transverse emittance (ε_x) can be calculated from elements of the resulting vector **a** (Eq(5.9)), using $\varepsilon_x = \sqrt{\det\sigma}$.

The error of the fitted parameters was estimated in [98], by introducing the function f

$$f = \begin{pmatrix} \alpha_{x_0} \\ \beta_{x_0} \\ \varepsilon_{x_0,\mathrm{RMS}} \end{pmatrix} = \begin{pmatrix} a_1/\sqrt{a_1a_3 - a_2^2} \\ -a_2/\sqrt{a_1a_3 - a_2^2} \\ \sqrt{a_1a_3 - a_2^2} \end{pmatrix}, \tag{5.12}$$

where a_1, a_2 and a_3 are elements of the vector a. The square error of the parameters ($\sigma^2_{\beta_{x0}}$, $\sigma^2_{\alpha_{x0}}$ and $\sigma^2_{\varepsilon_{x0,\mathrm{RMS}}}$) can be calculated by solving the following equation

$$(\nabla_a f)^T(\mathbf{B}^T\mathbf{B})^{-1}(\nabla_a f) = \begin{pmatrix} \sigma^2_{\beta_{x0}} & \cdots & \cdots \\ \cdots & \sigma^2_{\alpha_{x0}} & \cdots \\ \cdots & \cdots & \sigma^2_{\varepsilon_{x0,\mathrm{RMS}}} \end{pmatrix}. \tag{5.13}$$

Slice Emittance Measurement

Slice emittance is measured by using a combination of the quadrupole scan technique, which is described in Section 5.6.2, and the TDS. Two quadrupole magnets, High1.Q9 and High1.Q10, right before the TDS are used for the measurement. The experimental setup is similar to the one used for the bunch current profile measurement. The bunch is deflected by the TDS and is observed by the screen station PST.Scr2. Then, gradients of the quadrupole doublet are scanned and consequential deflected distributions are measured. By horizontally slicing the deflected distributions, Twiss parameters and emittance of each slice can be calculated from fitting the horizontal RMS size of each slice as a function of the quadrupole gradients.

An example of slicing the deflected distributions into nine slices is shown in Fig. 5.16. Figure 5.17 shows horizontal transverse RMS sizes of slice number 4, 5 and 6 for ten different setups of quadrupole gradients. From data in this plot, the geometrical emittance of each slice can be calculated by solving Eq. (5.8). Profiles of the measured slice emittance are shown in Fig. 5.18. The average values of slice emittance are 8.44 mm.mrad and 5.39 mm.mrad for the cases of 15 MeV/c and 22 MeV/c beam momenta, respectively. Error bars plotted in the figure are derived from Eq. (5.13).

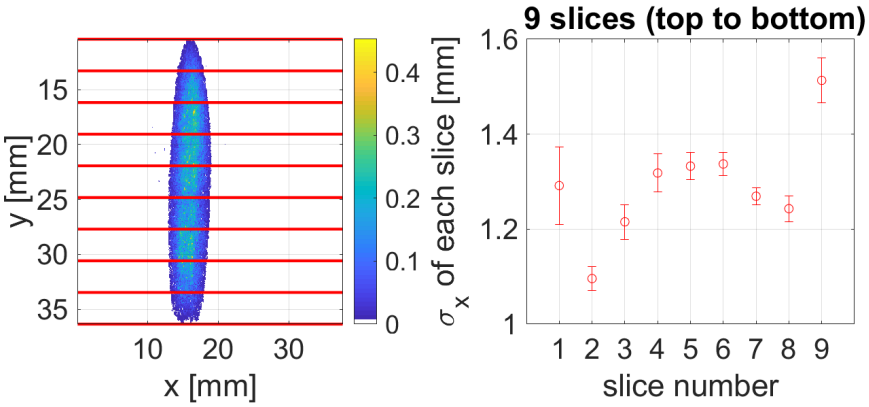

Figure 5.16: An example of slicing the measured deflected distribution into 9 slices

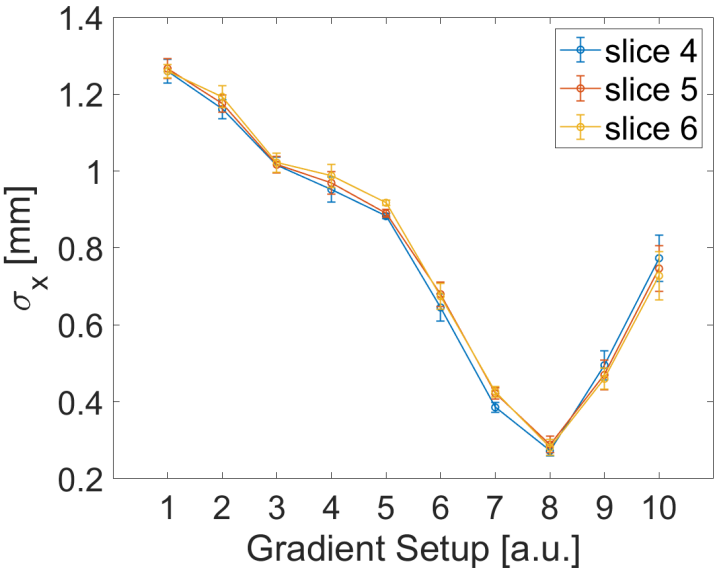

Figure 5.17: Horizontal transverse RMS sizes of slice number 4, 5 and 6 for ten different setups of quadrupole gradients.

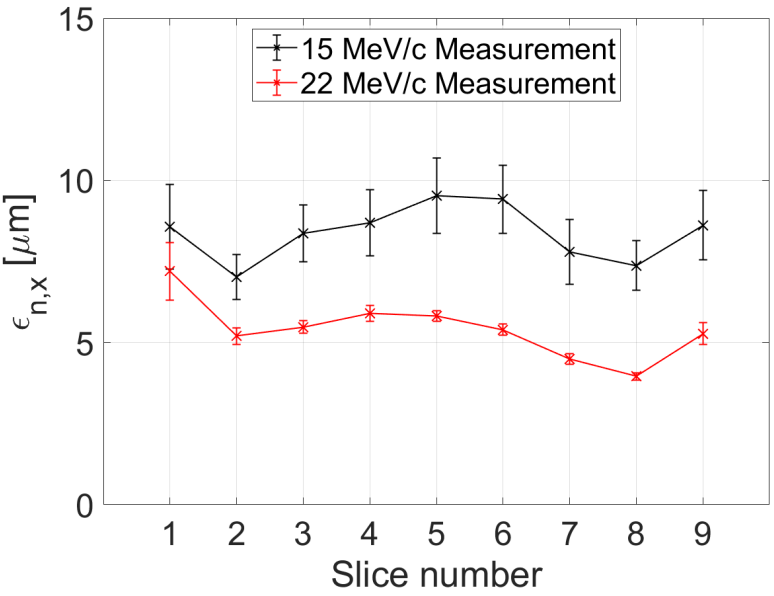

Figure 5.18: Measured profiles of horizontal slice emittance for the cases of the 15 MeV/c beam and the 22 MeV/c beam.

5.7 Follow-up Beam Dynamics Simulations

In order to understand details of space-charge dominated beam dynamics in the proposed photo-injector setup, corresponding simulations have to be performed to reproduce experimental results. Follow-up beam dynamics simulations with the same machine conditions used in the measurements were performed. Machine parameters used in the simulations are listed in Table 5.3.

Table 5.3: Machine and electron beam parameters

Parameters	**Values**
PC laser pulse duration [ps]	11 (FWHM), gaussian
PC laser diameter on the cathode [mm]	3.7
Peak electric field at the cathode [MV/m]	60.5
Peak electric field in the booster [MV/m]	10 and 17.4
Gun phase w.r.t. MMMG [degree]	0
Booster phase [degree]	for minimum momentum spread
Bunch charge [nC]	4

5.7.1 Photocathode Laser Modelling

There are some machine parameters used in the experiments which are different from those in the ideal S2E simulations. Furthermore, there are some practical factors which were not included in the S2E simulations. One of the important factors is that the PC laser transverse distribution has in-homogeneity of the radial profile. The modulation rings and decaying tails at the edge can be seen in the distribution (see Fig. 5.2). In ASTRA simulations, the cylindrical grid algorithm must be used in order to take mirror charges at the cathode into account and this algorithm treats the input distribution as a rotational symmetric distribution [55]. The radial profile including the core and the halo parts (core+halo), as shown in Fig. 5.19, derived from the measured laser distribution is applied into ASTRA simulations in order to include effects from the laser in-homogeneity. Figure 5.20 show the transverse profile of the core+halo distribution used in further ASTRA simulations. The uniform distribution is also shown in the same figure for comparison.

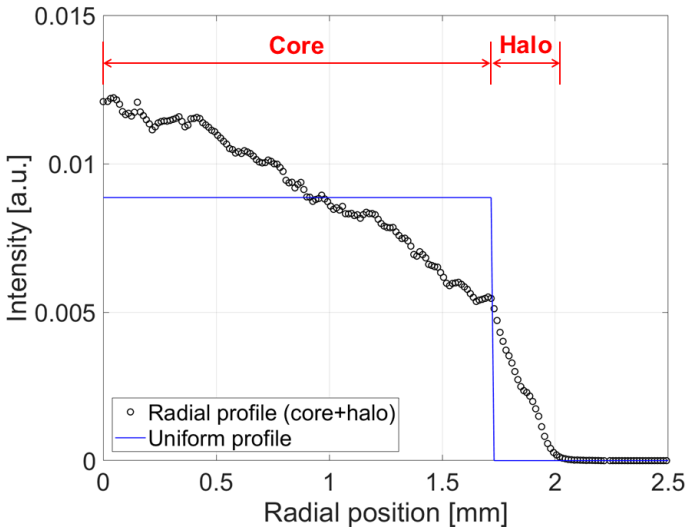

Figure 5.19: Illustration of the radial profile derived from the measured distribution, and the uniform radial profile normally used in ASTRA simulations.

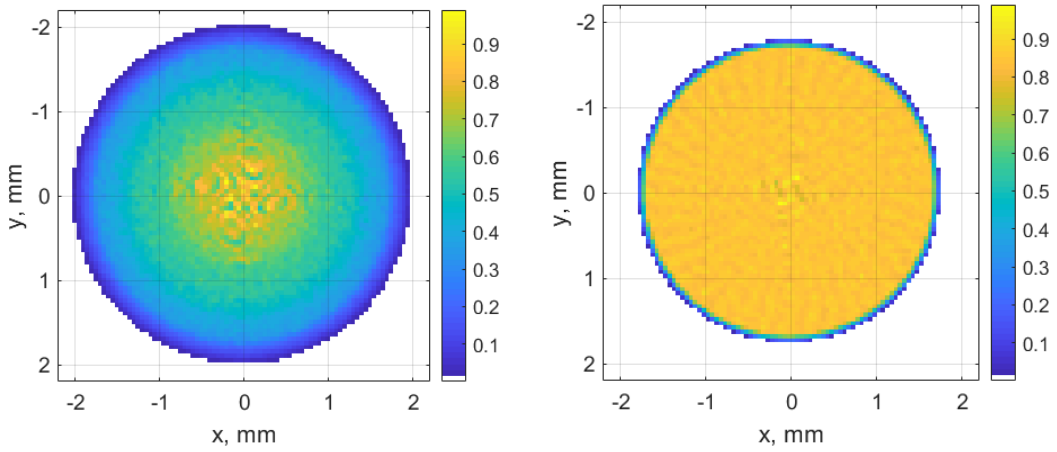

(a) Core+halo distribution

(b) uniform distribution

Figure 5.20: The core+halo distribution (a) used in the ASTRA simulations. A uniform distribution (b) is also shown here for comparison. Both distributions have the same transverse RMS size of 0.864 mm.

5.7.2 Simulation of Charge Production

As discussed in Section 5.2, the dependence of the accelerated charge on the laser pulse energy is important to determine the emission model used in beam dynamics simulations. In order to evaluate the accuracy of the emission model used in ASTRA, a simulation of charge production was performed. The core+halo distribution as shown in Fig. 5.20a was used as an initial distribution. The simulations were done with two sizes of laser diameter, 3.5 mm and 3.7 mm.

Figure 5.21 shows curves of output charge as a function of input charge from the measurement with a laser diameter of 3.5 mm and from the simulations with laser diameters of 3.5 mm and 3.7 mm. For the measured curve, the output charge means charge measured by a current transformer (LOW.ICT1 located at z = 0.903 m) and the input charge (Q_{input}) is calculated by

$$Q_{\text{input}} = E_{\text{laser}} \cdot m,$$

where E_{laser} is the measured laser energy and m is the slope of the linear part of the measured curve. For the simulated curves, the input charge is the initial input charge in ASTRA and the output charge means the bunch charge at z = 0.903 m. All curves show a linear dependence at low input charges (laser pulse energies) as expected in the quantum efficiency limited emission regime [96]. However, the curves reach their saturation point differently. The difference between the measured curve and the simulated curve with the laser diameter size of 3.5 mm means that the emission model implemented in ASTRA is close to its systematic limitation for these space-charge densities at the photocathode. Formations of beam phase space at the cathode could cause discrepancy in final beam parameters.

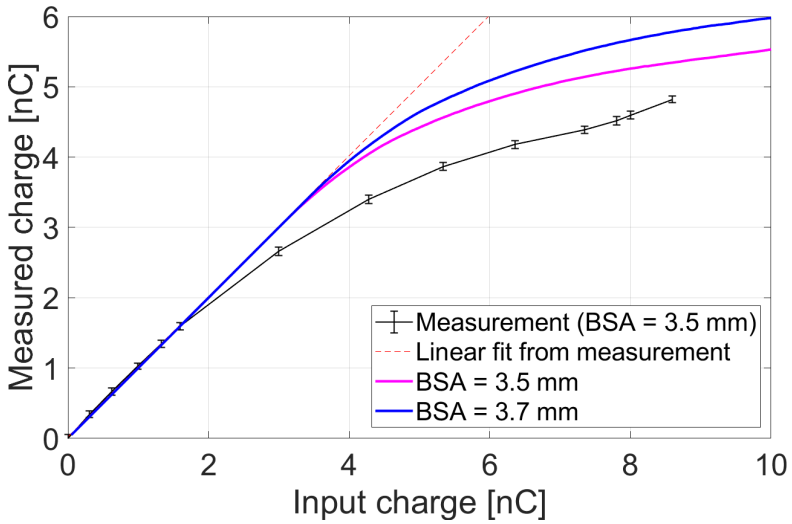

Figure 5.21: Measured charge as a function of the input charge.

5.7.3 Simulated Beam Momenta

In order to reproduce the measured values of average beam momentum and RMS momentum spread in ASTRA simulations, the simulations were done for different booster peak fields and booster phases. Then the momentum distributions after the booster were monitored.

The contour plots of simulated beam momentum and RMS momentum as a function of the booster peak field and the booster phase are shown in Fig. 5.22. Gray circles in the figure present the optimized booster peak field and booster phase for the case of 15 MeV/c where the average momentum is about 15 MeV/c and the RMS momentum is minimized. The red circles are the optimized parameters for the case of 22 MeV/c. Optimized beam momenta and corresponding settings are summarized in Table 5.4.

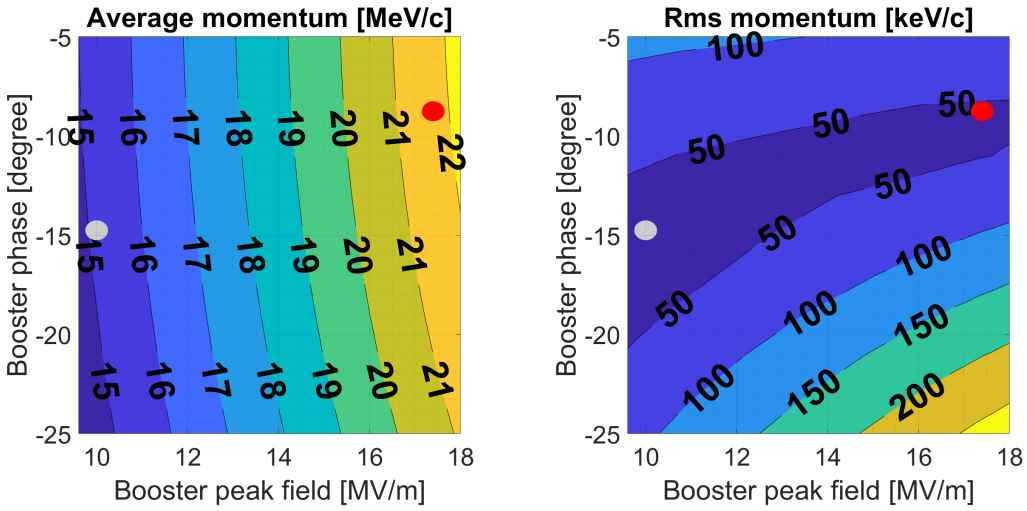

Figure 5.22: Simulated average beam momentum (left) and momentum spread (right) as a function of the booster peak field and the booster phase.

Table 5.4: Simulated optimized beam momenta and corresponding settings of booster peak fields and booster phases

Parameters	15 MeV/c	22 MeV/c
Average momentum [MeV/c]	15.13	21.69
Momentum spread [keV/c]	28.08	41.35
Booster peak field [MV/m]	10	17.4
Booster phase w.r.t MMMG [degree]	-15	-9

5.7.4 Simulated Beam Current Profiles

Simulated beam distributions were transported to PST.Scr2 (see Fig.3.1). High1.Q9 and High1.Q10 were used for focusing the beam at the PTS.Scr2. The current profiles derived from ASTRA distributions for the cases of 15 MeV/c and 22 MeV/c are shown in Fig. 5.23. Both current profiles are almost identical with a peak current of 160 A and an FWHM pulse duration of about 25 ps.

The simulated current profiles in Fig. 5.23 show discrepancies when compared to the measured current profiles in Fig. 5.10. The measured current profile of the 22 MeV/c case is shorter than one of the 15 MeV/c case. A possible reason for this difference could be an artifact from measurement resolutions. Another reason could be discrepancies which arise already in the photoemission modelling (Section 5.7.2).

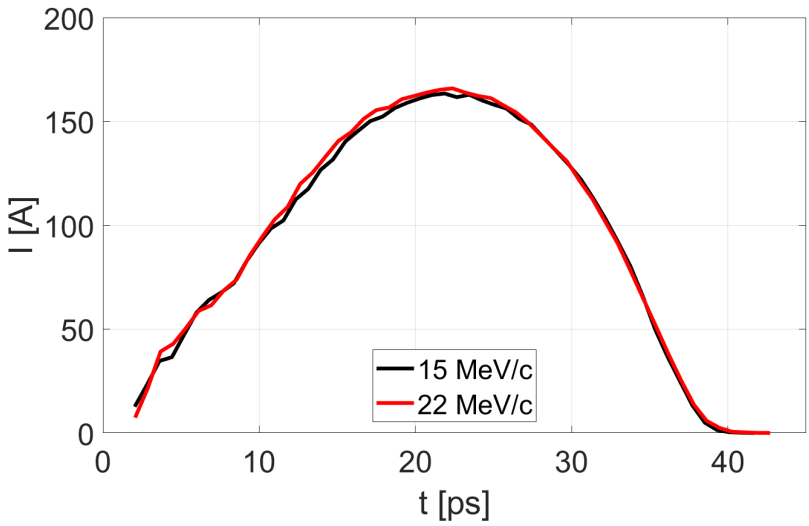

Figure 5.23: Simulated current profiles for the 15 MeV/c beam and 22 MeV/c beam. Relevent machine and beam parameters are listed in Table 5.3

.

5.7.5 Simulated Longitudinal Phase Spaces

The simulated beam distributions were transported to a distance of 18.47 m from the photocathode which is equivalent to the distance from the photocathode to a YAG screen in Disp3.Scr1. Similar to the longitudinal phase space measurement, two additional quadrupole magnets, PST.QT5 and PST.QT6, were used for beam transport and focusing. In order to investigate the effects of TDS fields on the longitudinal phase space, the simulations were done for two cases, without TDS fields (TDS off) and with TDS field (TDS on).

Figure 5.24 shows longitudinal phase space distributions of the 15 MeV/c beam with TDS on and TDS off while Fig. 5.25 shows those of the 22 MeV/c beam. It is obvious from the plots in both figures that TDS fields induce an increase of momentum spread. Evaluations of longitudinal phase spaces are presented in Fig. 5.26. For the 15 MeV/c case, the average slice momentum spread increases from 20 keV/c to 50 keV/c when TDS is on. For the 22 MeV/c case, the average slice momentum spread increases from 18 keV/c to 35 keV/c when TDS is on.

When TDS is on, the average slice momentum spread of the 22 MeV/c case is lower than one of the 15 MeV/c case. This behavior contradicts to the measured results in Fig. 5.12. A major cause of this contradiction could be the limitations of the measurement resolution. The values of beam projected emittance are quite high. They limit the transverse focusability of the beams and therefore limit the minimum achievable momentum resolution [85]. Imperfections of the beam transport could also cause beam dispersions and spoil the beam momentum spread.

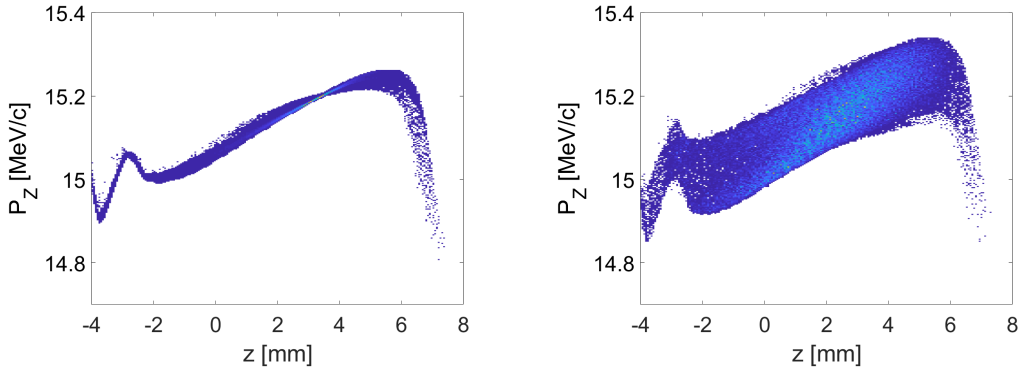

Figure 5.24: Simulated longitudinal phase space of the 15 MeV/c beam while the TDS is off (left) and while the TDS is on (right)

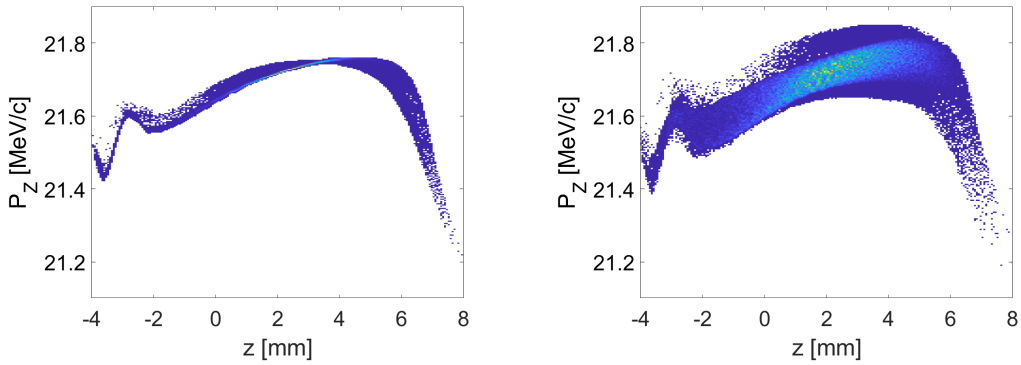

Figure 5.25: Simulated longitudinal phase space of the 22 MeV/c beam while the TDS is off (left) and while the TDS is on (right)

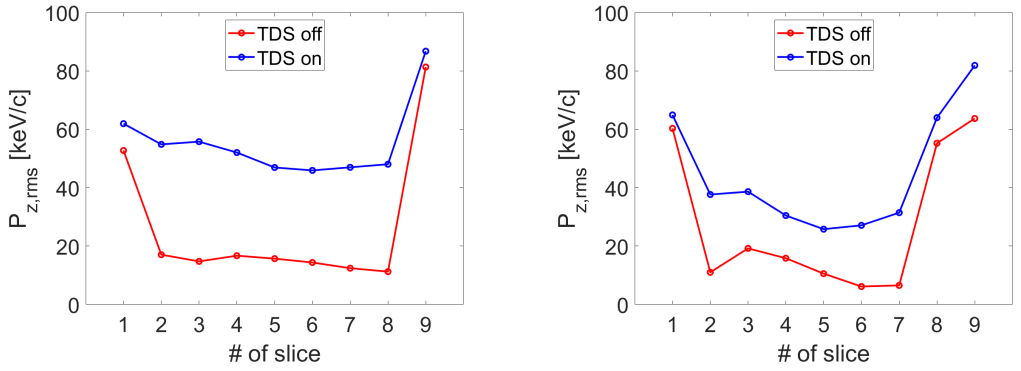

Figure 5.26: Slice momentum profiles for the cases of 15 MeV/c (left) and 22 MeV/c (right) from the simulations of measurements.

5.7.6 Simulation of Transverse Emittance Optimization

Similar to the procedure in Section 5.6.1, the projected transverse emittance was optimized by monitoring the emittance values at EMSY1 (Z = 5.277 m) as a function of the main solenoid current. Plots of simulated normalized emittance as a function of the main solenoid current are presented in Fig. 5.27. The results of projected emittance optimizations are summarized in Table 5.5.

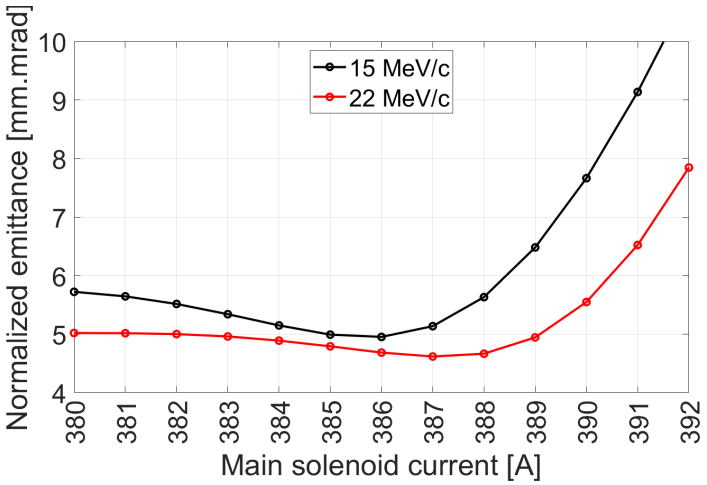

Figure 5.27: Simulated normalized emittance as a function of the main solenoid current for the cases of 15 MeV/c and 22 MeV/c.

Table 5.5: Optimized transverse normalized projected emittance of the 4 nC beams using ASTRA with the core plus halo distribution

Parameters	15 MeV/c	22 MeV/c
I_{m} for optimized emittance [A]	386	387
σ_{xy} for optimized emittance [mm]	2.150	1.486
Optimized $\varepsilon_{\mathrm{n,xy}}$ [mm.mrad]	4.956	4.631

By comparing the values in Table 5.5 to the values derived from measurements in Table 5.2, the emittance values from simulations are smaller than those from the measurements. For the case of 15 MeV/c, the measured value is higher by a factor of 2 than one from the simulation. For the case of 22 MeV/c, the simulated value is smaller than the one from the measurement by about 40 %.

Discrepancies between measured emittance values and those from the ASTRA simulations for the same laser diameter on the cathode were already observed in [16] and [100], especially for bunch charges above 250 pC. This difference is increasing with the bunch

charge and becomes more significant for the 4 nC case. The main reason for this discrepancy is that mechanisms of the space charge dominated photoemission is more complex than it is implemented in the ASTRA code. Another reason is that the gun quadrupole magnets do not fully compensate the asymmetry kick in the gun region.

5.7.7 Simulation of Slice Emittance Measurement

Since space charge effects are neglected in the slice emittance reconstruction from the quadrupole scan, the obtained experimental emittance values can deviate from the real values. Simulations of the slice emittance measurement using the quadrupole scan were performed in order to estimate possible errors from this measurement procedure.

The simulation of measurements using the quadrupole scan method follows the procedure of the real experiments. High1.Q9 and High1.Q10 were used with ten different gradient setup. Then the streaked beams were monitored on PST.Scr2 and used for slice emittance evaluations. Figure 5.28 shows profiles of horizontal slice emittance from the ASTRA simulations and from the simulation of measurements using the quadrupole scan method for both cases of beam momentum. The average values of slice emittance for all cases are listed in Table 5.6. According to the simulations for the case of 15 MeV/c, the value of the average slice emittance is overestimated by 87 %. For the case of 22 MeV/c, it is overestimated by 54 %. This difference can be explained by significant space charge effects that are neglected in the slice emittance reconstruction from the quadrupole scan.

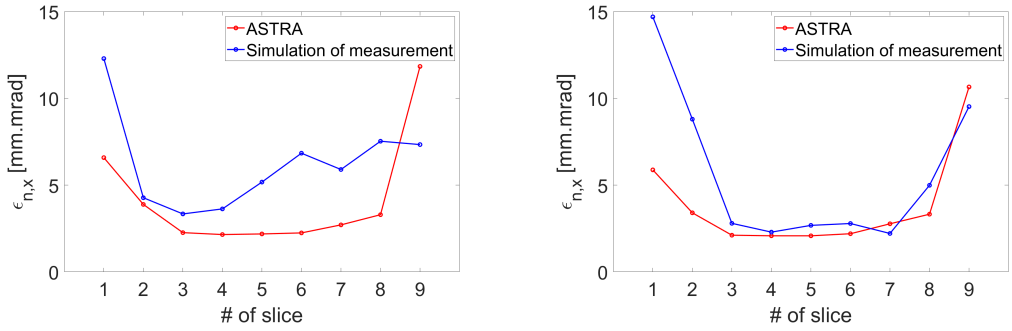

Figure 5.28: Comparison of horizontal slice emittance profiles from the ASTRA simulations and the simulations of measurements. The left plot is for the case of 15 MeV/c beam momentum and the right plot is for the case of 22 MeV/c.

5.8 SASE FEL Simulations

Measured electron beam parameters including beam current (Fig. 5.10), slice emittance (Fig. 5.18), and slice momentum spread (Fig. 5.12) were used for FEL simulations with

Table 5.6: Average horizontal slice emittance of the 4 nC beams from ASTRA simulations and simulations of measurements

Parameters	15 MeV/c	22 MeV/c
ASTRA simulation [mm.mrad]	3.00	2.81
Simulations of measurements [mm.mrad]	5.61	4.32

the GENESIS 1.3 code [48]. Parameters for the case of 15 MeV/c beam were used for the simulations with λ_{rad} = 100 µm while those for the case of 22 MeV/c momentum were used for the simulations with λ_{rad} = 20 µm. The helical undulator with period length of 40 mm is used as the radiator. The Twiss parameters of the beams were assumed to be matched for beam transport along the undulator.

Figure 5.29 presents the results of the simulated FEL pulse energy along the undulator. The values of pulse energy at the undulator exit (Z = 7 m) are 854 µJ and 687 µJ for the case of λ_{rad} =100 µm and λ_{rad} =20 µm, respectively. These pulse energy values are lower than those from optimized S2E simulations by a factor of 2.

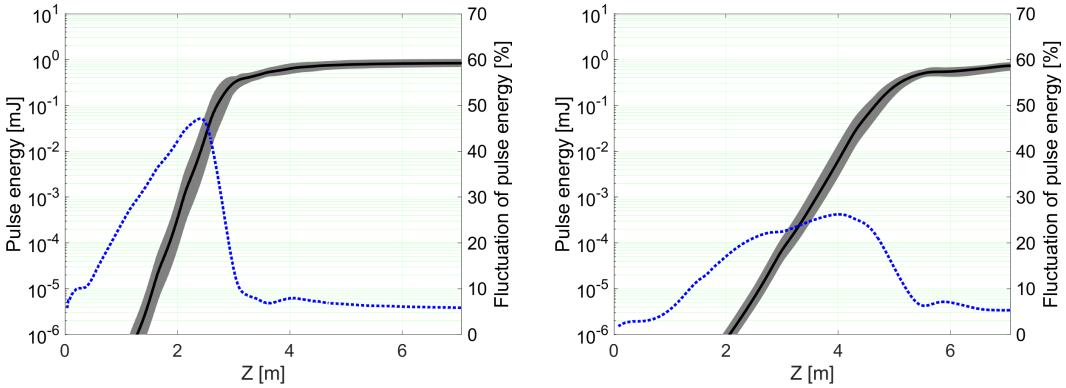

Figure 5.29: Pulse energy along the undulator from the FEL simulations with GENESIS code based on measured electron beam parameters. The left plot is for the case of λ_{rad} =100 µm using 15 MeV/c beam. The right plot is for the case of λ_{rad} =20 µm using 22 MeV/c beam

5.9 Concluding Remarks

Experimental optimization and characterization of 4 nC electron beams were done at PITZ including transverse distributions and time-resolved measurements. SASE FEL simulations based on the measured beam profiles were performed for the radiation wavelengths of 20 µm and 100 µm. The results show that radiation pulse energies close to the mJ level can be achieved within undulator lengths up to 7 m.

Follow-up beam dynamics simulations with the same machine conditions used in the measurements were performed. Discrepancies between simulations and measurements are observed. Possible causes of these discrepancies are space-charge effects, mismatch beam transports, and poor measurement resolutions.

Experiments using a flattop photocathode laser are planned to be performed in order to have the same conditions as implemented in the optimized S2E simulations. Beam measurement procedures and beam dynamics simulation methods have to be improved in order to understand and reduce discrepancies between simulation and measurement results.

Chapter 6

First Experimental measurements of CTR and CDR at PITZ

Based on the calculation results in Chapter 4, a radiation pulse with maximum pulse energies up to 20 µJ and peak frequency around 0.1 THz can be expected from the coherent transition radiation (CTR) and coherent diffraction radiation (CDR) using PITZ electron beams. In order to demonstrate such results experimentally, a screen station in the tomography section in the PITZ beamline (see Fig. 3.1) was modified to be the experimental station for generating CTR and CDR or called shortly as the CTR/CDR station.

This chapter starts with details concerning the design of the CTR/CDR station and the THz diagnostic system. Then, experimental generation and characterization of CTR generated from short electron bunches and from longitudinally modulated electron bunches are presented and discussed. After that, experiments of CDR generation are presented. Finally, concluding remarks are given as a closure.

6.1 The CTR/CDR Station

In order to perform experimental generation and characterization of CTR and CDR, the first CTR/CDR station was designed and installed in the PITZ beamline. Since the space of the beamline is limited, the screen station PST.Scr2 located at 13 m downstream from the cathode (see Fig. 3.1) was modified to be the CTR/CDR station. The reasons for selecting this screen station are:

- There is enough space around the screen station for additional devices.
- There is already an electron beam imaging system consisting of a YAG screen, a vacuum viewport, and a CCD camera at this screen station.
- There is a TDS upstream and can be used for longitudinal beam diagnostics.

The YAG screen is carried by a screen holder that is attached to a linear stepper motor. In order to modify it to be the CTR/CDR Station, CTR/CDR radiators and a viewport that is

transparent in the THz frequency range (THz viewport) are additionally installed.

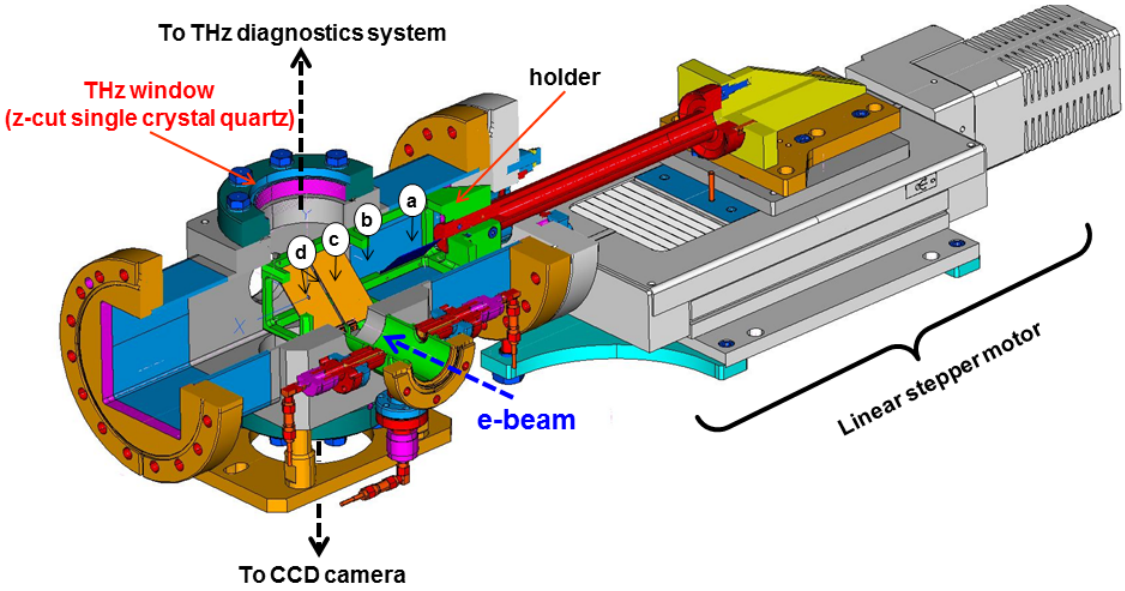

Figure 6.1: 3D model of the CTR/CDR station. The new screen holder includes (a) a YAG screen, (b) a gap for beam transport, (c) a CTR radiator, and (d) CDR radiators (more details are explained in the text). The holder is attached to a linear stepper motor. The top viewport is a THz viewport for transporting THz radiation to the THz diagnostic system while the bottom viewport is a silica viewport for transporting the light from the YAG screen to the CCD camera.

Figure 6.1 shows the 3D model of the THz station. The vacuum viewport and the CCD camera for the beam imaging were kept the same as before. A z-cut single-crystal quartz vacuum viewport transparent in the THz frequency range (manufactured product, model BVPZ64NQZ of Torr Scientific Ltd. [101]) was installed on the top for transporting the generated CTR/CDR to a THz diagnostics system. The old YAG screen holder was replaced with a new modified one that includes:

- a YAG screen with a size of 36 mm×55 mm which is monitored by a CCD camera from the bottom viewport,
- a gap with a size of 36 mm in the horizontal axis for undisturbed electron beam transport,
- a CTR radiator made of an Aluminium sheet with a size of 27 mm×55 mm×1 mm,
- a CDR radiator made of an Aluminium sheet with a size of 27 mm×55 mm×1 mm with a hole in the middle (ϕ = 2 mm),
- a 2 mm gap between two aluminium plates to use as a CDR radiator.

The YAG screen is tilted by 45° with respect to the longitudinal axis of the beamline

in order to observe the electron beam transverse distribution at the CCD camera via the bottom viewport. The radiators are also tilted by 45° with respect to the longitudinal axis of the beamline in order to have the directions of the backward CTR/CDR radiations towards the top viewport.

When each radiator is located at its operational position, the distance between its center and the THz viewport is 71 mm while the vacuum viewport has a radius size of 30 mm. The acceptance angle of this station, therefore, can be calculated from these two parameters and it is equal to 0.42 rad.

6.2 THz Diagnostics System

The THz CTR/CDR that exits the THz viewport is transported to the THz diagnostic system. Properties of the radiation planned to be measured by this system are spectral distribution and the total pulse energy. Different setups are required for measuring each of the properties.

6.2.1 THz Detector: Pyroelectric Detector

A room-temperature pyroelectric detector was used to measure the THz radiation intensity. When the THz radiation falls on a pyroelectric detector, it heats up the detector. Then the pyroelectric crystal inside the detector is expanded and generates a polarization current. This polarization current accumulates a surface charge at electrodes inside the detector. The output signal from the circuit of these electrodes is proportional to the change of the crystal temperature which is determined by the THz radiation pulse energy [26].

The pyroelectric detector used in the system is a manufactured product, model THz20 of SLT Sensor- und Lasertechnik GmbH [102]. The output signal from the sensor is amplified by a signal amplifier with an adjustable gain of 10, 10^2, 10^3 and 10^4. The relaxation time for the heated sensor temperature to the ambient temperature is called the thermal time constant. The thermal time constant of the detector used in the experiment is 300 ms which is much longer than an electron bunch length and also an electron bunch train. Therefore, this detector was used to measure the intensity of a pulse train with 10 Hz repetition rate. At least 50 electron bunches per macro-pulse were used for the THz generation in order to have high enough intensity for the detector. The results of some measurements will be presented in terms of pulse energy, where appropriate. Otherwise, they will be presented in terms of the voltage unit.

6.2.2 Setup for Spectral Distribution Measurement

The THz diagnostics system was set up to be a Michelson interferometer for the spectral distribution measurement. A simplified schematic layout of a Michelson interferometer

is shown in Fig. 6.2. It consists of a beam splitter, a fixed mirror, a movable mirror, and a THz detector arranged as shown in the layout. The radiation that enters the Michelson interferometer is split into two parts by the beam splitter. Then both parts travel to the mirrors and are reflected back to the beam splitter. After that, the two parts are combined and transported to the detector. Principles and equations in this section are revised from Ref. [42]. More detailed explanations and mathematical treatments can be found in the reference.

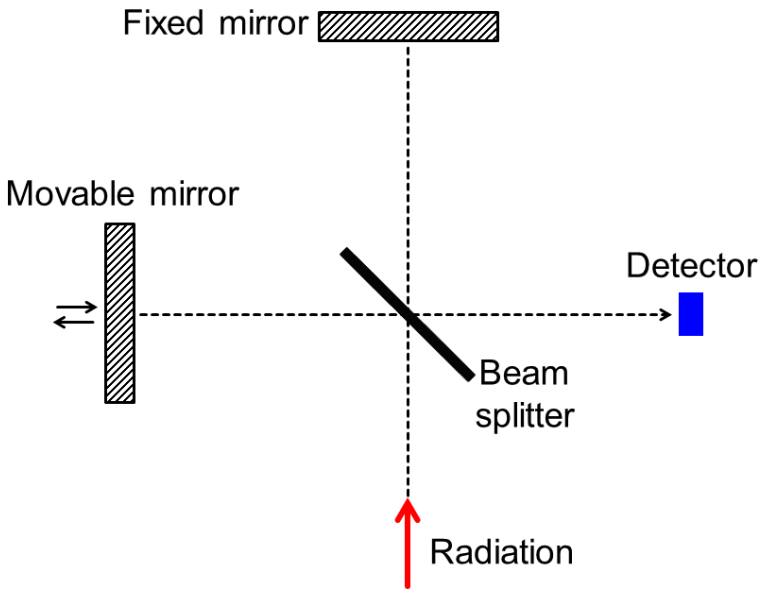

Figure 6.2: A schematic diagram of a Michelson interferometer.

The movable mirror can create a variable optical path difference δ between the two arms which is equal to δ/c in time. The radiation pulse from the fixed arm E_{fixed} and the radiation pulse from the movable arm E_{movable} which are transported to the detector can be expressed in the time domain as

$$E_{\text{fixed}}(t) = R \cdot T \cdot E(t) \quad \text{and} \tag{6.1}$$

$$E_{\text{movable}}(t + \frac{\delta}{c}) = T \cdot R \cdot E\left(t + \frac{\delta}{c}\right) \quad , \tag{6.2}$$

respectively. Here $E(t)$ is the radiation pulse that enters the Michelson interferometer, R and T are the reflection and transmission coefficients of the beam splitter, respectively. The radiation pulse energy measured at the detector (U_{detector}) is then

$$
\begin{aligned}
U_{\text{detector}}(\delta) &\propto \int \left| E_{\text{fixed}}(t) + E_{\text{movable}}(t+\frac{\delta}{c}) \right|^2 \mathrm{d}t \\
&\propto \int |E_{\text{fixed}}(t)|^2 + \left| E_{\text{movable}}(t+\frac{\delta}{c}) \right|^2 + 2\text{Re}\left[E_{\text{fixed}}(t) E^*_{\text{movable}}(t+\frac{\delta}{c}) \right] \mathrm{d}t \\
&\propto 2\text{Re} \int E_{\text{fixed}}(t) E^*_{\text{movable}}(t+\frac{\delta}{c}) \mathrm{d}t + 2\int |E_{\text{fixed}}(t)|^2 \mathrm{d}t \\
&\propto 2\text{Re} \int |R\cdot T|^2 E(t) E^*(t+\frac{\delta}{c}) \mathrm{d}t + 2\int |R\cdot T\cdot E(t)|^2 \mathrm{d}t.
\end{aligned}
\tag{6.3}
$$

The first term is an autocorrelation of the radiation pulse and the second term determines its baseline. An interferogram ($U_{\text{interferogram}}$) is a representation of the radiation autocorrelation [42],

$$
U_{\text{interferogram}}(\delta) \propto 2\text{Re} \int |R\cdot T|^2 E(t) E^*(t+\frac{\delta}{c}) \mathrm{d}t. \tag{6.4}
$$

The radiation power spectrum is the Fourier transformation of the interferogram

$$
U_{\text{interferogram}}(\omega) \propto \int_{-\infty}^{\infty} U_{\text{interferogram}}(\delta) \exp\left(\frac{-i\omega\delta}{c} \right) \mathrm{d}\delta. \tag{6.5}
$$

The top plot in Fig. 6.3 shows an example of an ideal interferogram measured by a Michelson interferometer. The spectral distribution derived by taking the Fourier transform of the interferogram is presented in the bottom plot.

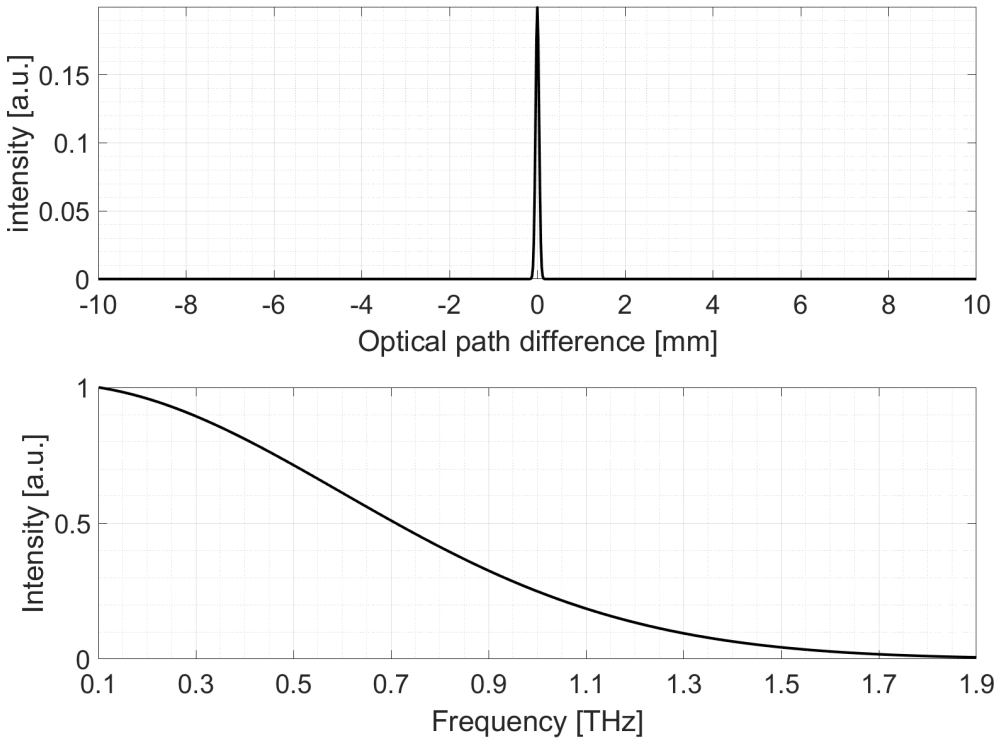

Figure 6.3: An example of an ideal interferogram (top) measured by a Michelson interferometer and corresponding spectral distribution (bottom) calculated by taking the Fourier transform of the ideal interferogram.

Figure 6.4 shows the actual setup of the Michelson interferometer used in measurements. The main components include 90° off-axis goal-coated parabolic mirrors, gold-coated flat mirrors, a THz beam splitter, a copper collector cone, and a THz pyroelectric detector. The role of each component is as follows:

- The first parabolic mirror (90° off-axis, ϕ = 101.6 mm, f = 152.4 mm) is used to convert the divergent radiation from the CTR or CDR to be a collimated (parallel) radiation.
- The second parabolic mirror (90° off-axis, ϕ = 101.6 mm, f = 152.4 mm) is used to focus the collimated radiation from the first parabolic mirror to the third parabolic mirror.
- The third parabolic mirror (90° off-axis, ϕ = 50.4 mm, f = 50.4 mm) is used to collimate the focused radiation from the second parabolic mirror and then transport the radiation to the beam splitter.
- The THz beam splitter (ϕ = 50.4 mm) is used to split the radiation into two parts, then transmit and reflect it to the fixed and the movable flat mirrors. Note that the beam splitter is made of HRFZ-Silicon with a thickness of 3.5 mm (manufactured product, model BS-HRFZ-Si of TYDEX [103]).
- There are two flat mirrors (ϕ = 50.4 mm) in the setup, a fixed flat mirror and a movable flat mirror. The movable one is attached to a translation stage which is movable in 1D by the linear stepper motor.
- The copper collector cone (ϕ = 50.4 mm) is used to collected the combined radiation from the beam splitter for measurements by the pyroelectric detector.
- The pyroelectric detector is used to measure the radiation pulse energy. Its details are already explained in section 6.2.1.

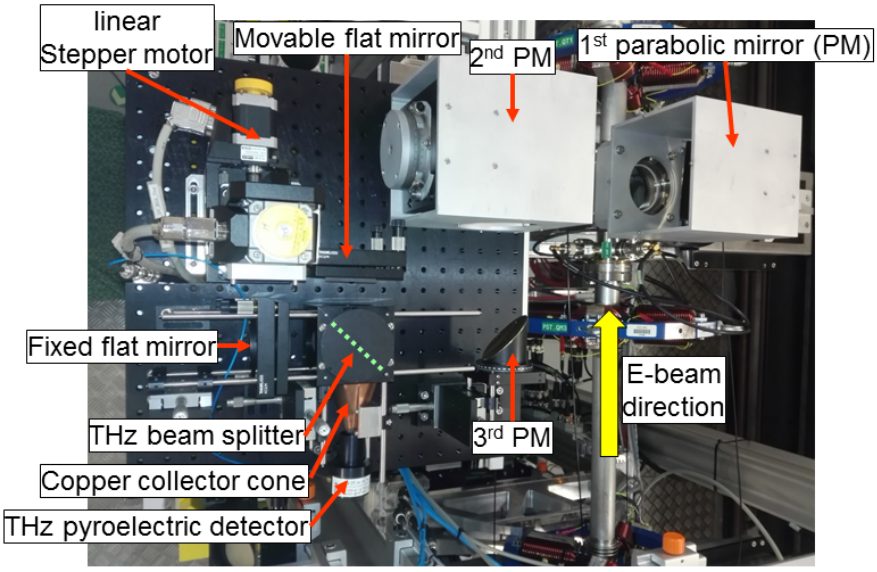

Figure 6.4: The Michelson interferometer setup

6.2.3 Setup for Total Radiation Pulse Energy Measurement

Figure 6.5 shows the setup for the total radiation pulse energy measurement. The first half of the setup is similar to the one for the spectral distribution measurement until the third parabolic mirror. For this setup, the copper collector cone and the THz pyroelectric detector were placed directly after the third parabolic mirror in order to collect all the radiation for measurement by the detector.

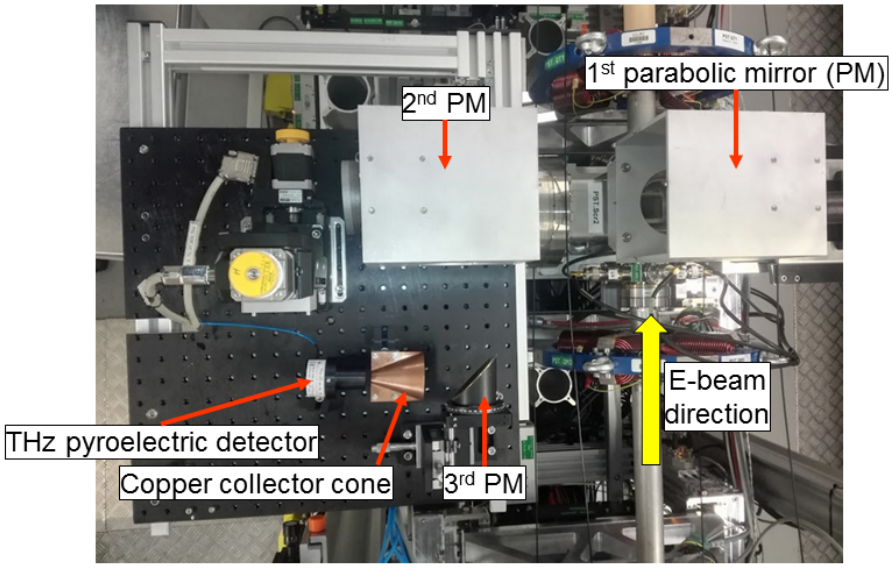

Figure 6.5: The setup for total CTR/CDR radiation pulse energy measurement.

6.3 Characterization of CTR Generated from Short Electron Bunches

By inserting the CTR radiator (an Aluminum plate) into the beam path, the CTR is generated and then transported through the top viewport to the THz diagnostic system. This section presents and discusses characterization results of CTR generated from short electron bunches. These short bunches are generated by using the photocathode laser pulses with a short Gaussian temporal shape (∼2.4 ps FWHM). Then, the bunch is compressed by velocity bunching using the booster cavity as described in the S2E simulations in Chapter 4. Machine parameters used during the experiments are listed in Table 6.1. Due to beamtime limitation, scanning steps of the bunch charge and the booster phase are not as detailed as in the S2E simulations.

Table 6.1: Machine and electron beam parameters for experimental characterization of CTR

Parameters	**Values**
Photocathode FWHM Gaussian laser pulse duration [ps]	2.43
Photocathode laser diameter on the cathode [mm]	2
Number of laser pulses	1 to 150
RF power in the gun [MW]	6.4
RF power in the booster [MW]	3.0
Gun phase w.r.t. MMMG phase [degree]	0
Booster phase w.r.t. MMMG phase [degree]	-80, -60, -30 and 0
Bunch charge [pC]	250 , 500 and 1000

The mean of electron beam momentum was measured as a function of the booster phase by the HEDA1 section. The measured momentum results shown in Fig. 6.6 are useful for calculating the radiation intensity. The TR spectral intensity from an electron can be calculated by the Ginzburg-Frank formula (Eq. (2.29))

$$\left.\frac{\mathrm{d}^2 I}{\mathrm{d}\Omega \mathrm{d}\omega}\right|_{\mathrm{GF}} = \frac{e^2}{4\pi^3 \varepsilon_0 c} \frac{\beta^2 \sin^2\theta}{(1-\beta^2\cos^2\theta)^2} \quad ,$$

The pulse energy per frequency unit can be derived by integration this equation over the solid angle

$$\left.\frac{\mathrm{d}I}{\mathrm{d}\omega}\right|_{\mathrm{GF}} = \int_0^{2\pi}\int_0^{\theta_a} \left.\frac{\mathrm{d}^2 I}{\mathrm{d}\Omega \mathrm{d}\omega}\right|_{\mathrm{GF}} \mathrm{d}\theta \mathrm{d}\phi = 2\pi \int_0^{\theta_a} \left.\frac{\mathrm{d}^2 I}{\mathrm{d}\Omega \mathrm{d}\omega}\right|_{\mathrm{GF}} \mathrm{d}\theta \quad , \tag{6.6}$$

where θ_a is the acceptance angle of the measurement system.

The radiation energy at various acceptance angles can be calculated by using Eq. (6.6). The maximum acceptance angle is limited at $\pi/2$ rad for integration over one hemisphere. The collection efficiency of each acceptance angle is defined as a ratio between the transition radiation pulse energy within the acceptance angle and the TR pulse energy within the acceptance angle of $\pi/2$ rad. Figure 6.7 presents the collection efficiency as a function of the acceptance angle for various beam momenta as presented in Fig. 6.6. The vertical dashed line represents the acceptance angle of the station, 0.42 rad. It indicates that this station has a collection efficiency range of about 40 - 60 % for the beam momentum range of 9.13 to 22.67 MeV/c.

6.3.1 Total Energy Measurement

The setup in Section 6.2.3 was used for the total radiation pulse energy measurement. The backward transition radiation is generated while using various electron beam parameters

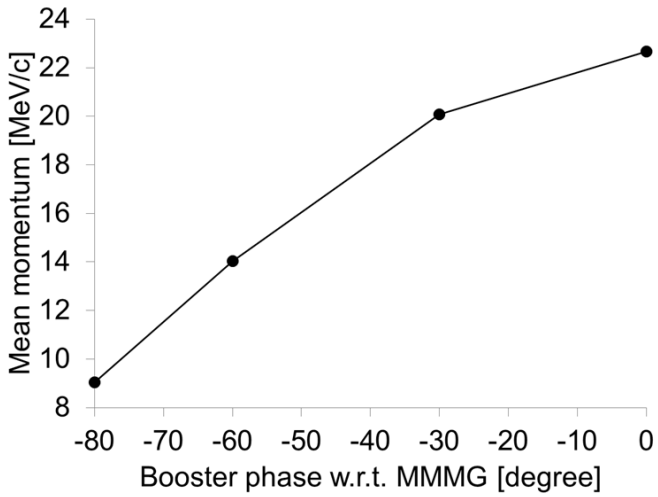

Figure 6.6: Measured mean momentum of the electron beam as a function of booster phase.

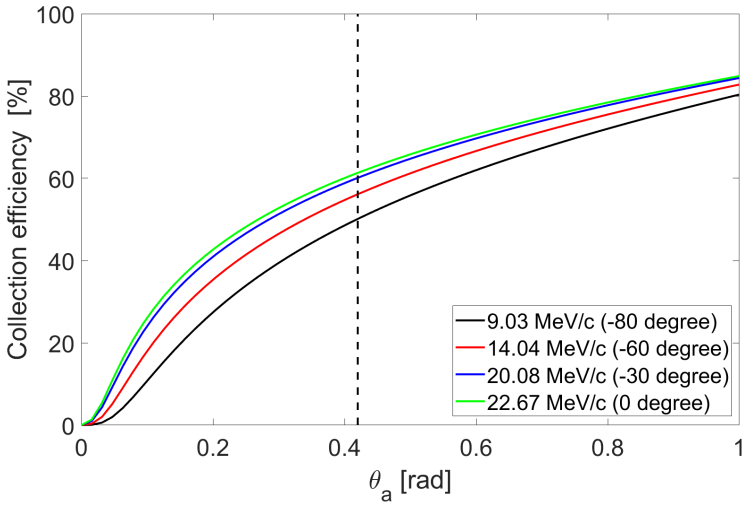

Figure 6.7: TR collection efficiency as a function of the acceptance angle (θ_a) for various electron beam momentum (booster phase).

as presented in Table 6.1. Measurement results of average TR energy per a radiation pulse (generated by an electron bunch) as a function of the booster phase are presented in Fig. 6.8. The range of measured average TR energies per pulse span from 50 nJ to 1.85 µJ

which are lower than the simulated pulse energies in Chapter 4. In practical, the radiation pulse energy loss is due to various reasons including diffraction loss during radiation beam transport, absorption loss at the vacuum viewport and absorption loss by water in a humid air environment.

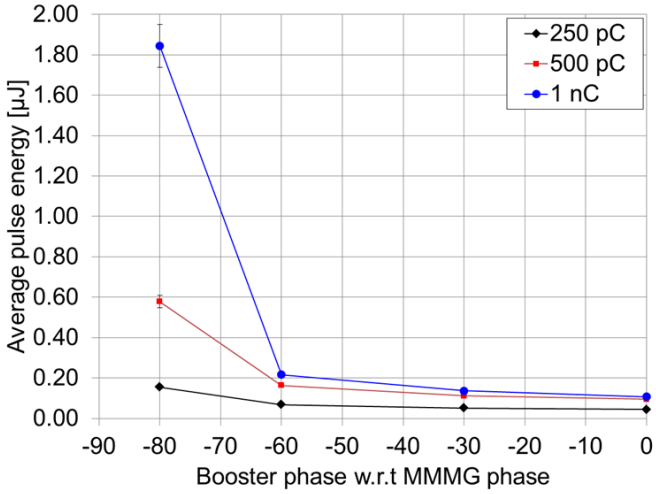

Figure 6.8: Average pulse energy of the CTR as a function of booster phase

Effect of the Beam Size

Based on the generalized Ginzburg-Frank formula, the beam size also has effects on the transition radiation intensity. In order to demonstrate and investigate these effects, the CTR intensity was measured as a function of electron beam RMS sizes which are measured by using the YAG screen. For this demonstration case, the electron bunch charge of 500 pC and the booster phase fixed at the MMMG phase were used.

The results of transition radiation intensity as a function of the beam RMS size are displayed in Fig. 6.9. Note that the halo part of the beam was filtered out during each of the beam size evaluations. The horizontal error bar represents the transverse asymmetry of the beam RMS sizes which could contribute to the discrepancy between the measured and calculated results. The error bar is determined to be the following range: $\pm\frac{|\sigma_x+\sigma_y|}{2}$, where σ_x and σ_y are the horizontal and vertical transverse RMS sizes of the beam, respectively. The vertical error bar represents the statistical error of the intensity measurement. The transition radiation intensities based on the experimental conditions were calculated

and are presented together with the measured results as a red curve. They are in good agreement with the measured results.

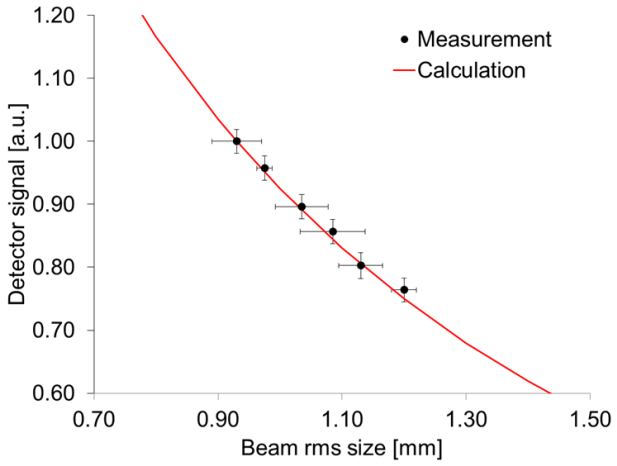

Figure 6.9: Measured transition radiation intensity from various electron beam RMS sizes and corresponding calculations based on the experimental conditions. The intensities are normalized to the measured maximum intensity.

6.3.2 Spectral Distribution Measurements

The spectral distributions of transition radiation are measured by using the Michelson interferometer setup as shown in Fig. 6.4. This setup measures the interferogram of the transition radiation and its Fourier transformation represents the spectral distribution of the radiation as explained in Section 6.2.2. For each interferogram measurement, the moving mirror position is scanned between the range of −10 mm to 10 mm w.r.t the position with zero path difference. The step of the scanning is 0.02 mm.

The measured interferograms of the CTR are presented in Fig. 6.10. The results from the cases with a booster phase of −80° and bunch charges of 250 pC and 1 nC are selected here. Both measured interferograms have left-right asymmetry and oscillations along the optical path difference.

The left-right asymmetry is caused by optical diffraction losses during the interferogram measurements. In order to investigate this effect, propagation of transition radiation through this Michelson interferometer setup was simulated by the THzTransport [104] software. A simple model of the setup was used in the simulation. Only mirrors and the realistic optical path were included, while effects from the THz viewport and the beam

splitter were neglected. The simulations were performed for two cases of the optical path, the longest optical path (middle optical path + 10 mm) and the shortest optical path (middle optical path - 10 mm). The collection efficiency of the setup is defined as the ratio between the radiation intensity at the entrance of the copper collector cone and the radiation intensity at the first parabolic mirror. The simulated collection efficiency as a function radiation frequency is presented in Fig. 6.11. The collection efficiency is up to 56 % for all frequencies below 1.9 THz and strong suppression happens for frequencies below 0.7 THz. The curve of the shortest optical path case is slightly higher than the other curve. This means the total intensity collected by the copper cone is in first-order proportional to the optical path difference and could be a reason for the left-right asymmetry.

Another issue is the oscillations. A possible cause of the small oscillations is water absorption, while effects from the beam splitter and the pyroelectric detector could be the causes of the bigger oscillations. Detailed discussion on this issue can be found in [42].

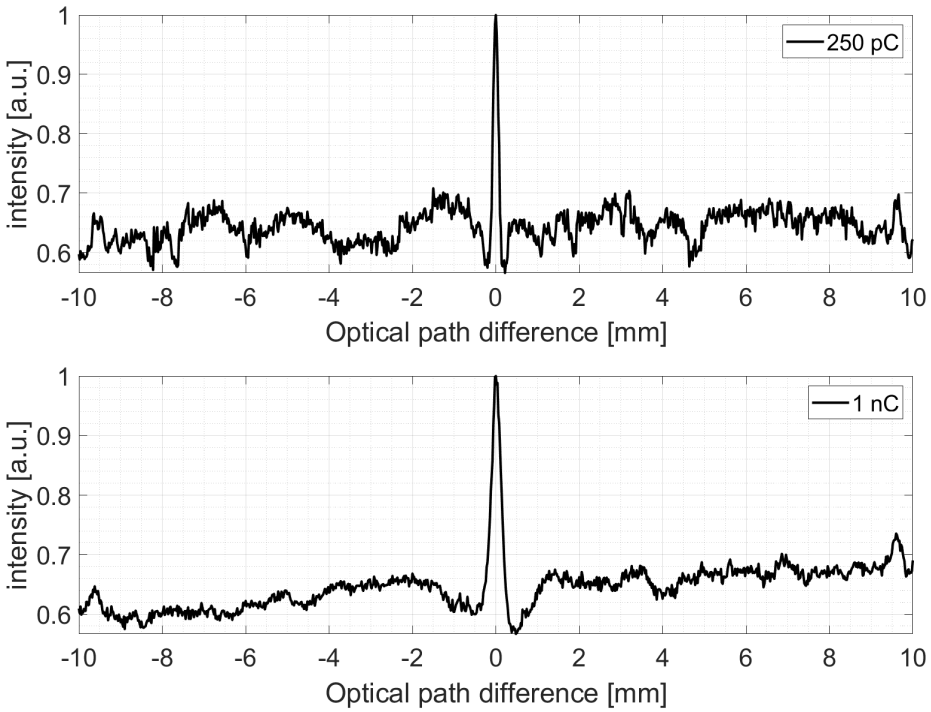

Figure 6.10: Measured interferograms of the CTR from electron bunches with bunch charges of 250 pC (top) and 1 nC (bottom) where a booster phase of 80 degree w.r.t. MMMG phase was used for velocity bunching.

By performing Fourier transformations of the measured interferograms in Fig. 6.10, corresponding spectral distributions are derived and presented in Fig. 6.12. Figure 6.12a shown the normalized spectral distributions. The 1 nC distribution has a peak intensity at the frequency of 0.18 THz and covers a frequency range up to 0.6 THz. The 250 pC

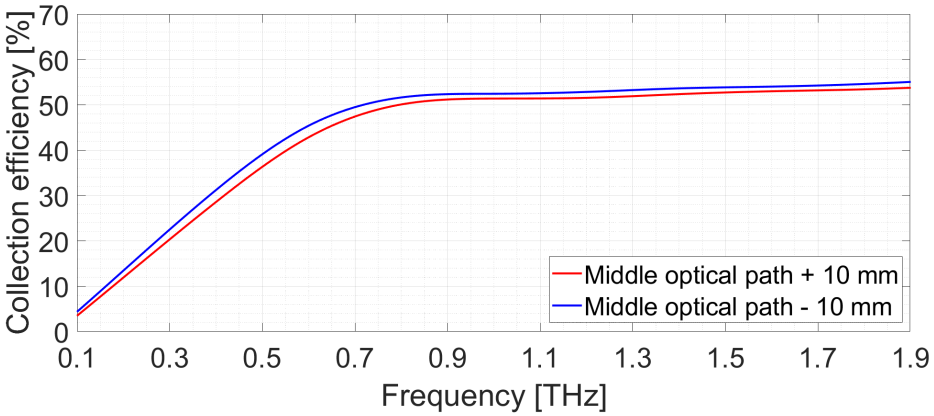

Figure 6.11: Calculation of diffraction loss of the interferometer setup in form of the collection efficiency as a function of radiation frequency.

distribution covers a broader frequency range between 0.18 THz and 1.1 THz. These frequency ranges indicate the temporal coherent characteristic of the radiations. In order to get more information concerning the coherent characteristics of the spectral distributions, the distribution is scaled with a square of the number of electrons within the bunch and presented in Fig. 6.12b. The scaled 1 nC distribution shows significantly higher spectral intensity in the low-frequency part while the scaled 250 pC distribution starts to have higher intensity at the frequency of about 0.5 THz.

6.4 Characterization of CTR Generated from Longitudinal Modulated Electron Bunches

A modulated electron bunch is an electron bunch where its temporal current distribution is modulated to have at least two micro-bunches. The form factor of the modulated beam shows peaks at higher harmonics frequency [95]. Therefore, it is interesting to perform an experiment on CTR generation by using a modulated beam in order to verify this characteristic.

The longitudinally modulated beam is produced by a longitudinally modulated cathode laser pulse. Such a laser pulse can be produced by using the laser pulse shaper in the MBI laser system as explained in Chapter 2. However, the optical sampling system (OSS) used for measurements of the laser temporal profile was not available. Therefore, results of the pulse shaper adjustments were monitored directly from the longitudinal electron beam profiles which are measured by using TDS.

For this experiment, the RF power in the gun and the booster are the same as for experiments in the previous section. The gun and booster phases were fixed at the MMMG

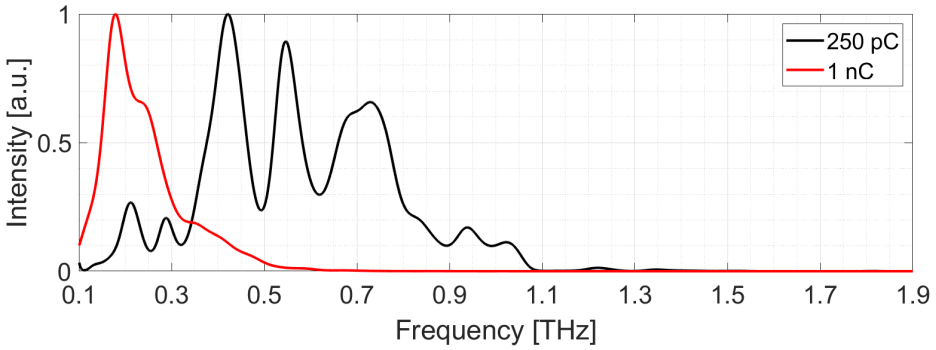

(a) Spectral distributions, normalized to maximum

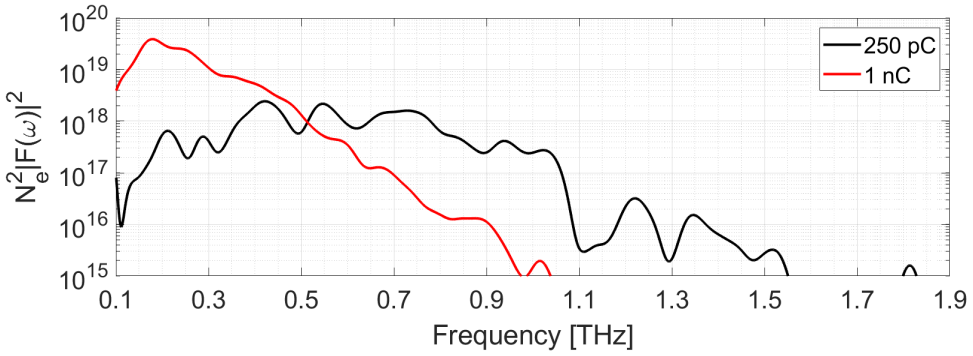

(b) Scaled spectral distributions. Note that the vertical axis has a logarithmic scale.

Figure 6.12: Spectral distributions calculated by taking the Fourier transform of the Interferograms in Fig 6.10

phases (corresponding mean momentum of ∼22 MeV/c) and the electron beam with a bunch charge of 1 nC was used. The measured profile of a modulated beam with 1 nC bunch charge used for the CTR generation is shown in Fig. 6.13. The profile of the compressed beam (-80 degree booster phase off-crest) with 1 nC bunch charge is also presented together for comparison. Note that the comb beam was accelerated with the MMMG phases of the gun and the booster. The modulated-beam profile has 4 peaks with maximum peak current of ∼50 A while the compressed beam has peak current of ∼330 A. The bunch length of each peak of the modulated-beam profile is difficult to estimate since the peaks are not so obvious while one of the compressed profile is about 2.5 ps FWHM. However, both profiles were difficult to focus and transport through the TDS. Therefore the measurement resolutions are quite poor. The measurement resolutions of the comb-beam and the compressed beam profiles are 5.8 ps and 3.4 ps, respectively.

Figure 6.14 shows the measured interferogram of the modulated beam. The interferogram is different from the short bunch case. Higher-harmonic oscillations can be observed. The left-right asymmetry is still remaining as same as observed in previous

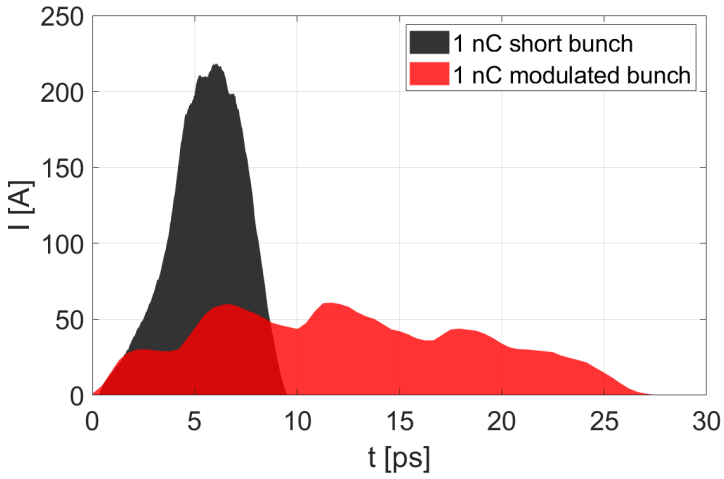

Figure 6.13: Longitudinal distribution of the 1 nC modulated bunch together with the 1 nC short-bunch distribution compressed by velocity bunching (booster phase of -80 degree). Both distributions were measured using the TDS.

measurements.

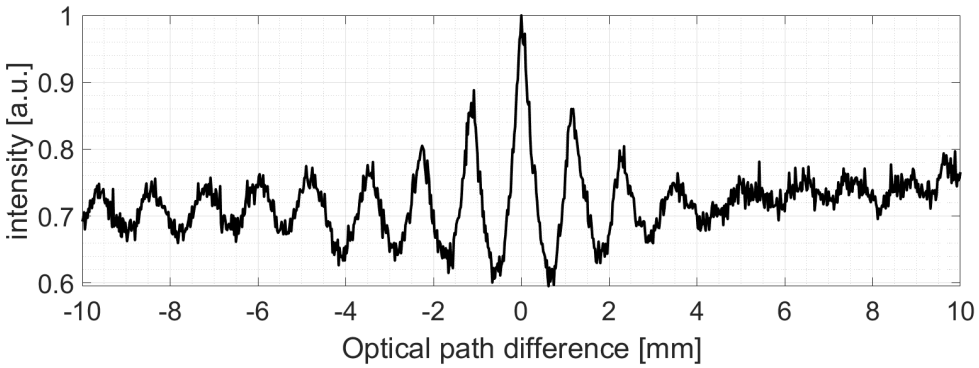

Figure 6.14: Measured interferograms of the CTR from the modulated electron bunch with 1 nC bunch charge.

Corresponding spectral distribution from the interferogram of the modulated-beam are presented in Fig. 6.15a together with the distribution of the 1 nC short bunch case (booster phase of -80°) for comparison. The modulated-beam spectral distribution shows a narrow band frequency with peak intensity at 0.26 THz and FWHM width of about 0.3 THz. The higher harmonic frequencies cannot be seen from this figure. They can be seen from the scaled distribution (with plotting in logarithmic scale). The higher-order frequencies at 0.26, 0.53, 0.79 and 1.1 THz can be seen.

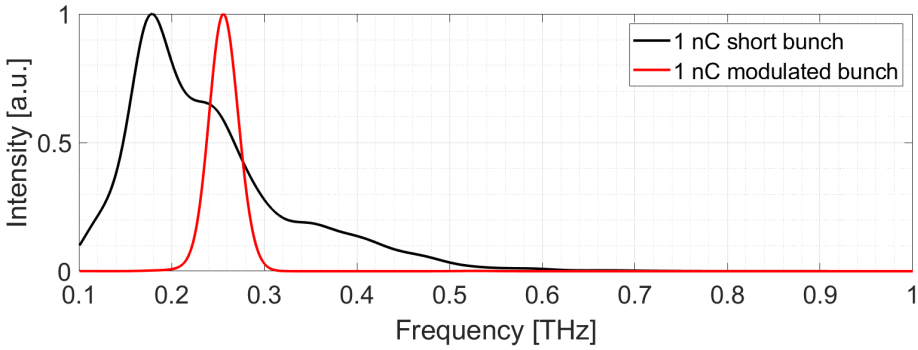

(a) Spectral distributions of the 1 nC short gaussian beam and the 250 nC comb beam

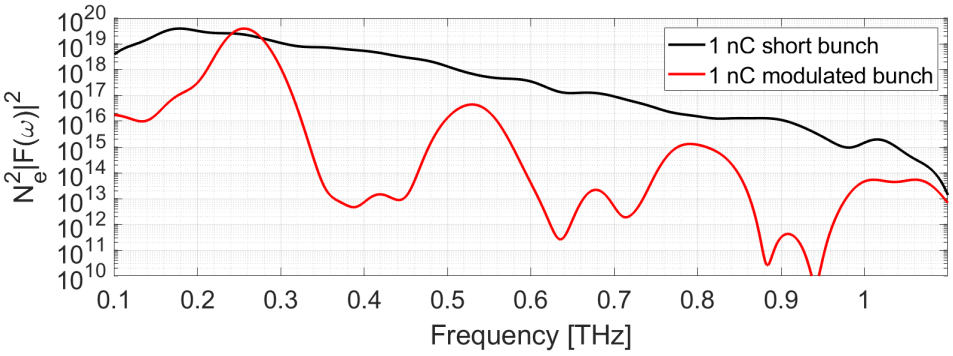

(b) Scaled spectral distributions of the 1 nC short gaussian beam and the 250 nC comb beam. Note that the vertical axis has a logarithmic scale.

Figure 6.15: Spectral distributions calculated by taking the Fourier transform of the Interferograms in Fig. 6.14.

6.5 Characterization of CDR Generated from Short Electron Bunches

The diffraction radiation is generated by an electron beam passing through the circular hole aperture in an aluminum plate or the gap between two aluminum plates as shown in Fig. 6.1. All parameters listed in Table 6.1 were used. Only the bunch charge was fixed at 500 pC. Similar to the CTR experiments, total pulse energy and the spectral distribution of the CDR were measured.

6.5.1 Total Energy Measurement

The backward diffraction radiation intensity as a function of the booster phase w.r.t. MMMG phase is measured. The result is shown in Fig. 6.16 together with the measured result of transition radiation from the aluminum plate for comparison. Comparisons of

intensity from CDR and CTR for different cases are presented in Table 6.2. Note that the intensity drop in the table is the ratio of the CDR intensity subtracted by the CTR intensity to the CTR intensity, and the charge loss means charge loss at the Al-plate when the beam is passing through the aperture.

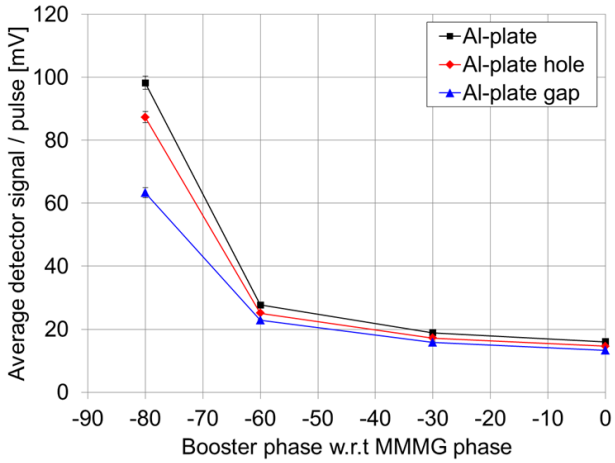

Figure 6.16: CTR (Al-plate as the radiator) and CDR (Al-plate hole and Al-plate gap as the radiators) intensity as a function of the booster phase

Table 6.2: Intensity drops and charge losses for each case of CDR compared to CTR

Booster phase	**Al-plate hole**	**Al-plate hole**	**Al-plate gap**	**Al-plate gap**
	Intensity drop	Charge loss	Intensity drop	Charge loss
0	−8.95 %	18.78 %	−17.02 %	12.29 %
30	−9.04 %	16.12 %	−15.90 %	3.14 %
60	−9.13 %	27.76 %	−17.32 %	10.42 %
80	−11.17 %	26.67 %	−35.52 %	26.22 %

6.5.2 Spectral distribution measurement

The spectral distributions were measured by using the Michelson interferometer. The booster phase was fixed at MMMG phase in order to be able to focus the beam to the smallest beam size and to minimize the charge loss in the CDR process. The measured interferograms from CTR and CDR are displayed in Fig. 6.17. Shapes of interferograms

of all 3 cases are almost identical. Corresponding calculated spectral distributions presented in Fig. 6.18 are also almost identical.

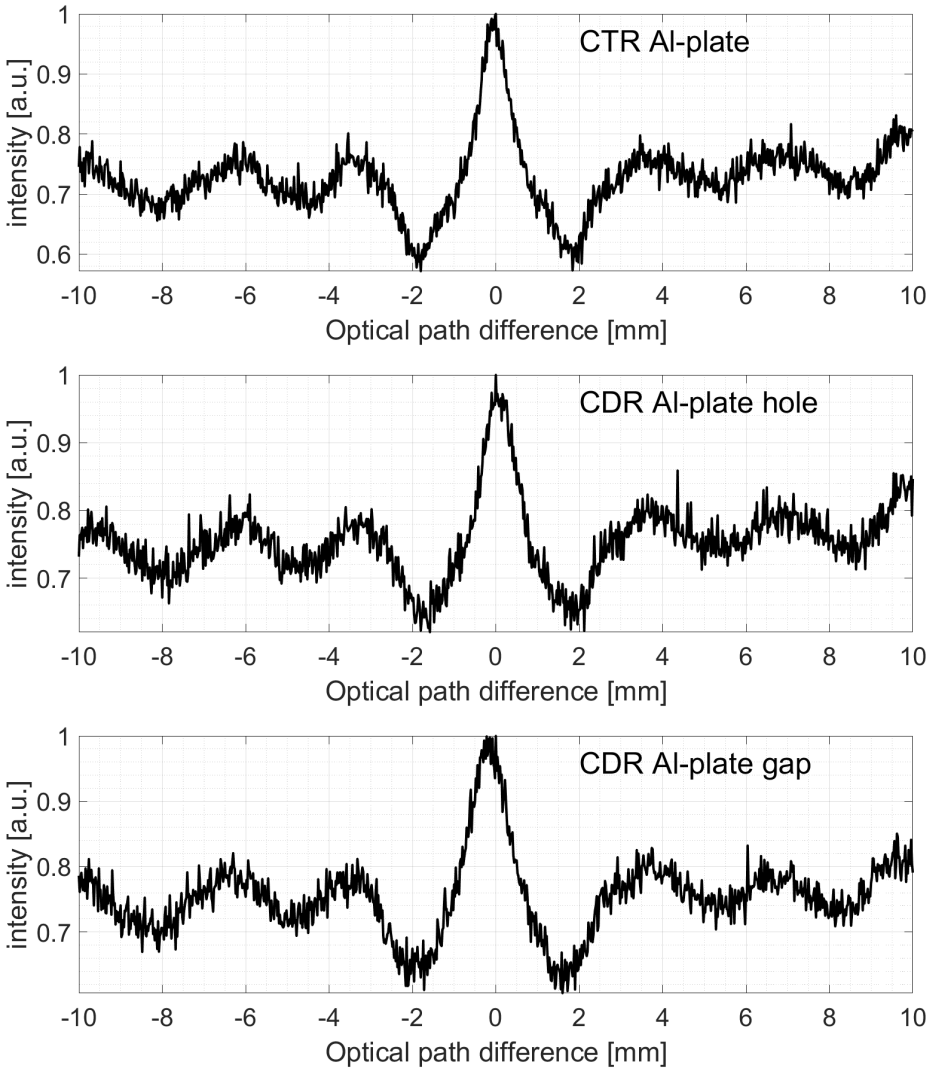

Figure 6.17: Interferograms of the CTR from Al-plate (top) the CDR from Al-plate with a circular hole (middle) and the CDR from Al-plate with a gap (bottom).

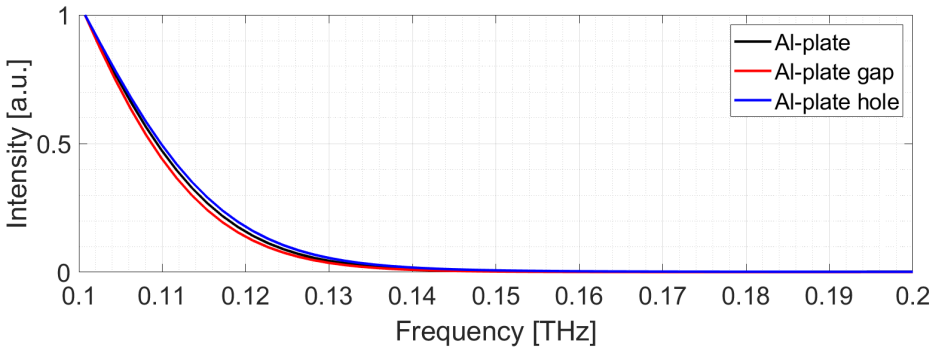

(a) spectral distributions

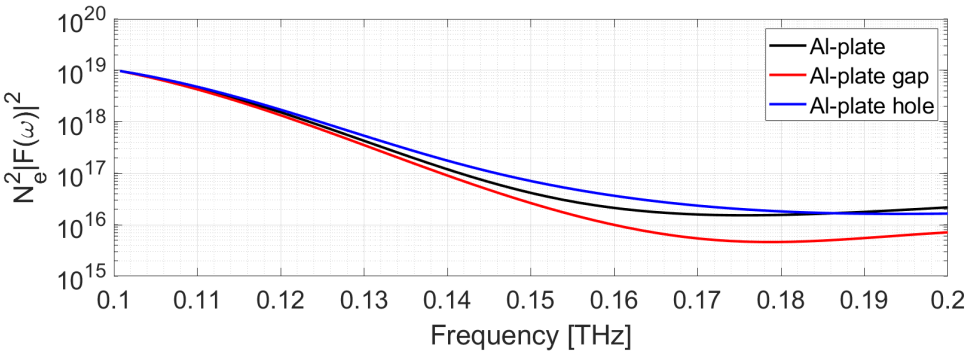

(b) Scaled spectral distributions

Figure 6.18: Spectral distributions of the CTR and the CDR calculated by taking the Fourier transform of the Interferograms in Fig. 6.17

.

6.6 Conclusion Remark

The CTR/CDR station has been designed, fabricated, and commissioning. The first experimental generations of CTR and CDR at PITZ were conducted successfully. Average pulse energies up to 1.85 μJ and coherent frequencies up to 1.5 THz were measured. By generating CTR using the comb beam, the spectral distribution shows narrow-band frequencies in its spectral distribution.

The next step to improve the THz diagnostics system is to use a THz camera. This will allow measuring polarization and the transverse distribution of the radiation and can help with the THz optics alignment. Re-design of the optical layout and setup in an extremely low humidity environment should be considered as well. In order to further investigate differences between CTR and CDR, better signal to noise ratio during the measurements and more sizes of the CDR radiators are required.

The setup for THz radiation diagnostics used in these experiments can be a prototype radiation measurement system for other methods of radiation generation.

Chapter 7

Summary and Outlook

The accelerator-based PITZ facility can be considered an ideal machine for the development of a prototype THz source for pump and probe experiments at the European XFEL. The capabilities of THz production at the PITZ Facility are investigated in this thesis.

7.1 Overview studies of PITZ-based THz sources

THz radiation based on the PITZ accelerator using various mechanisms of radiation generation including bending magnet radiation, edge radiation, undulator radiation, SASE FEL radiation, transition radiation, and diffraction radiation were calculated and presented in Chapter 2. A PITZ-based THz source can provide THz pulse trains which have identical repetition rate as the X-rays pulse trains at the European XFEL. By comparing the PITZ-based THz source to other laser-based and accelerator-based sources, the SASE FEL based on the PITZ accelerator shows remarkably high pulse energy at the mJ level for an FEL radiation wavelength of 100 µm at 27000 pulses per second.

7.2 Studies of the THz SASE FEL Option

S2E Simulations

S2E simulations of the SASE FEL using an APPLE-II type undulator with a period length of 40 mm in the helical mode were performed and discussed in Chapter 4. The ASTRA code was used for beam dynamics simulations, the Genesis 1.3 code was used for simulations of the FEL process. The simulations using a flattop photocathode laser with a temporal duration of 22 ps FWHM show that the FEL process reaches saturation within an undulator length of about 3 m and 6 m for the 100 µm and 20 µm cases, respectively. Pulse energies of sub-mJ to mJ level are achievable.

Radiation pulses from SASE FEL have strong fluctuations which are not favorable for many pump-probe experiments. To improve the radiation pulse stability, more suitable FEL options, like a seeded THz FEL, have to be implemented. Studies of THz FEL seeding options will be performed in the future.

Electron Beam Characterizations

Experimental optimization and characterization of electron beams with a high bunch charge of 4 nC using a Gaussian photocathode laser with a temporal duration of $\sim$11 ps FWHM for the SASE FEL option were performed and presented in Chapter 5. Parameters of the beam which are required as input for the FEL simulations were measured including slice emittance, slice energy spread and current distribution. The measurements were conducted for two cases of electron beam momentum, 15 MeV/c and 22 MeV/c, which is corresponding to the FEL radiation wavelength of 100 µm and 20 µm, respectively. SASE FEL simulations based on the measured beam profiles were performed. The results show that a radiation pulse energy close to the mJ level can be achieved within a saturation length up to 7 m. The FEL pulse energies are lower than those from the S2E simulations in Chapter 4 by a factor of $\sim$2.

7.3 Studies of THz CTR and CDR

S2E Simulations

S2E simulations of the THz radiation generation by means of CTR and CDR were also performed and discussed in Chapter 4. By using a short-Gaussian photocathode laser pulse and the electron bunch charge up to 1 nC, a CTR radiation pulse energy up to 10 µJ and frequencies covering up to 0.2 THz can be expected. CDR calculations for several cases were also performed. Their pulse energies are slightly lower than those of the CTR case. S2E simulations of CTR generated by using a comb beam were also performed. The spectral distribution of the comb bunch has several peaks of more narrow-band frequencies.

As seen from the simulation results, the RMS bunch duration can only be compressed down to about 1 ps by velocity bunching using the CDS booster. In order to compress the bunch more, another approach is needed like using a chicane bunch compressor, using a shorter photocathode pulse or using an additional buncher cavity.

Experimental Generations of CTR and CDR

First experimental generation of CTR and CDR at PITZ was performed successfully and presented in Chapter 6. The average pulse energy of up to 1.85 µJ and the coherent fre-

quency of up to 1.8 THz were measured. By generating CTR using the comb beam, the spectral distribution shows narrow-band frequencies in its spectral distribution.

7.4 Next step of THz Generation Studies at PITZ

As mentioned in Section 7.2, the THz SASE FEL is one of the most interesting options of PITZ-based THz sources. The next step is to perform first proof-of-principle experiments of THz SASE FEL generation at PITZ. In the S2E simulation studies, an APPLE-II type undulator was used as the radiator. However, building a new APPLE-II type undulator is quite expensive. Another interesting option of the undulator is the LCLS-I undulator modules which are available on loan from the Stanford Linear Accelerator Center (SLAC), USA [105].

Figure 7.1 shows the top-view drawing of the PITZ tunnel including tunnel annex and the possible location of the LCLS-I undulator. Preliminary S2E simulation studies of a THz SASE FEL based on an LCLS-I undulator and the PITZ accelerator are presented and discussed in Appendix B.

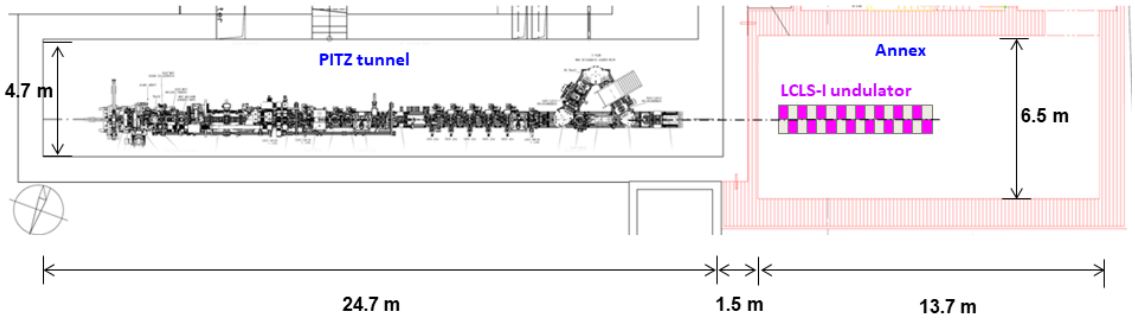

Figure 7.1: Top-view drawing of the PITZ tunnel including tunnel annex and possible location of the LCLS-I undulator.

For the next few years, proof-of-principle experiments on THz SASE FEL generation based on an LCLS-I undulator and the PITZ accelerator have the highest priority for THz research activities at PITZ. Studies on seeding FEL options will be performed in parallel in order to be ready to upgrade the FEL facility after finishing the proof-of-principle experiments.

Appendix A

Transportation Matrices and Electron Beam Parameters

PITZ accelerator consists of two RF accelerating sections; a RF photoelectron gun (called shortly as a RF gun) and a RF linear accelerator called CDS booster. Electrons are generated by photoelectric emission from a photocathode inside the RF gun using external laser pulses, then accelerated by the RF gun and the CDS booster. More details about PITZ accelerator are explained in Chapter 3. Since the electrons are generated by laser pulses, therefore the electrons also have pulse-like longitudinal density. A pulse (or a group) of electrons is called an electron bunch and a train of electron bunches is called an electron beam.

This appendix aims to introduce transverse phase space of an electron bunch, transportation Matrices for an electron dynamics which are also applicable for transformation of the phase space, and definition of important electron beam parameters.

A.1 Transverse Phase Space

Principles and equations in this section are summarized from Ref. [83]. More detailed explanations and mathematical treatments can be found in the reference.

Concept of phase space is popularly used for describing status of an electron bunch. Each electron in the bunch is represented by a point in six-dimensional (6D) phase space with coordinates (x, p_x, y, p_y, z, p) where x and y are the transverse coordinates, z is the longitudinal coordinate, p_x and p_y are the transverse momenta, and $p = \sqrt{p_x^2 + p_y^2 + p_z^2}$ where p_z is the longitudinal momenta. In accelerator physics, using of the relative momentum coordinates instead of the momentum coordinates is much more convenient. Therefore, the original 6D-coordinates are often used as $(x, x', y, y', z, \delta p)$ where $x' \approx p_x/p_0$, $y' \approx p_y/p_0$, and $\delta p = (p - p_0)/p_0$ where p_0 is the average momentum of the electron bunch.

By neglecting coupling among three planes, the 6D phase space can be split into three independent 2-dimensional (2D) planes of phase space. For the transverse planes, the electron beam motion can be represented separately into the horizontal x, x' phase space and the vertical y, y' phase space. An ellipse surrounding all electrons in phase space is called the phase ellipse. The horizontal phase ellipse is described by

$$\gamma x^2 + 2\alpha x x' + \beta x'^2 = \varepsilon, \tag{A.1}$$

where α, β, γ and ε are ellipse parameters or also called Twiss parameters. The plot of Eq. (A.1) is shown in Fig. A.1. The area of phase ellipse called the geometrical emittance

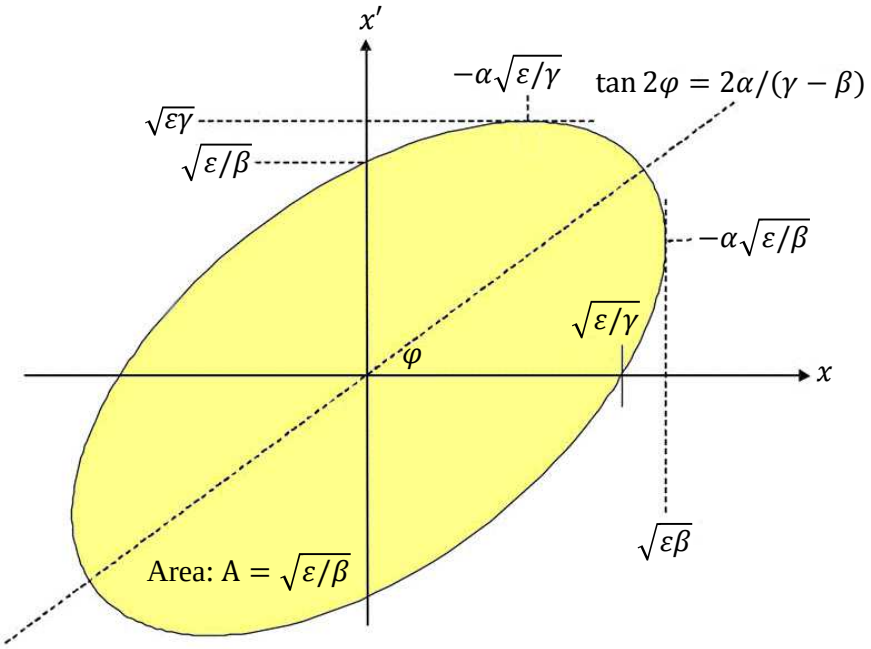

Figure A.1: Horizontal phase ellipse plotted from Eq. (A.1) [83].

ε is defined by

$$\int_{ellipse} x x' = \pi\varepsilon. \tag{A.2}$$

The other Twiss parameters determine shape and orientation of the ellipse and also have correlation as

$$\gamma\beta - \alpha^2 = 1. \tag{A.3}$$

For a 2D phase space, the beam matrix (σ) is defined with the Twiss parameters as

$$\sigma = \begin{pmatrix} \sigma_{11} & \sigma_{12} \\ \sigma_{21} & \sigma_{22} \end{pmatrix} = \varepsilon \begin{pmatrix} \beta & -\alpha \\ -\alpha & \gamma \end{pmatrix}. \tag{A.4}$$

From definition of the beam matrix and by assuming a Gaussian particle distribution in the phase space, relations of the Twiss parameters to statistical properties of the particle distribution in the horizontal plane are:

$$\langle x_i^2 \rangle = \varepsilon\beta, \tag{A.5}$$

$$\langle x'^2_i \rangle = \varepsilon\gamma, \tag{A.6}$$

$$\langle x_i x'_i \rangle = -\varepsilon\alpha. \tag{A.7}$$

By using Eq. (A.3) to Eq. (A.7), the beam geometrical emittance, or called RMS emittance (ε_{RMS}) in this context, can be expressed by

$$\varepsilon_{RMS} = \sqrt{\langle x_i^2 \rangle \langle x'^2_i \rangle - \langle x_i x'_i \rangle^2}. \tag{A.8}$$

By following Liouville's theorem, the density of the electron beam in phase space remains constant. When the beam is accelerated, the emittance has to be scaled according to the beam momentum in order to keep consistency with Lioville's theorem. Therefore, the scaled emittance called a normalized RMS emittance is introduced as

$$\varepsilon_{n,RMS} = \frac{\bar{p}_z}{m_0 c}\varepsilon_{RMS}, \tag{A.9}$$

where m_0 is the mass of an electron [106].

All principles and equations in this section are also applicable for the vertical plane, therefore, the symbol x in all equations in this section can be replaced by the symbol y for the case of the vertical plane.

A.2 Transportation Matrices

By neglecting the space-charge effects and assuming that trajectories of electrons in the bunch are independent from one another, a way to calculate electron motions under an influence of the Lorentz force analytically is to use the matrix formalism [83]. The general solutions of electrons transport from position z_0 to position z_f can be presented in matrix formulation by

$$\begin{pmatrix} x \\ x' \\ y \\ y' \\ z \\ \delta p \end{pmatrix}_{z_f} = \begin{pmatrix} R_{11} & R_{12} & R_{13} & R_{14} & R_{15} & R_{16} \\ R_{21} & R_{22} & R_{23} & R_{24} & R_{25} & R_{26} \\ R_{31} & R_{32} & R_{33} & R_{34} & R_{35} & R_{36} \\ R_{41} & R_{42} & R_{43} & R_{44} & R_{45} & R_{46} \\ R_{51} & R_{52} & R_{53} & R_{54} & R_{55} & R_{56} \\ R_{61} & R_{62} & R_{63} & R_{64} & R_{65} & R_{66} \end{pmatrix} \begin{pmatrix} x \\ x' \\ y \\ y' \\ z \\ \delta p \end{pmatrix}_{z_0}, \tag{A.10}$$

or in a simplified form as

$$X_{z_f} = \mathscr{R} X_{z_i}, \tag{A.11}$$

where 6×6 matrix $\mathscr{R}$ is the transport matrix, X_{z_i} is the initial coordinate vector and X_{z_f} is the final coordinate vector of the electron [107], By assuming that the motion in x,y and z planes are independent from each other (uncoupling motion), all elements in $\mathscr{R}$ those concerning to coupling between two planes can be set to 0 and the matrix formulation can be expressed in form of 2×2 transport matrices for each motion plane as

$$\begin{pmatrix} x \\ x' \end{pmatrix}_{z_f} = \begin{pmatrix} R_{11} & R_{12} \\ R_{21} & R_{22} \end{pmatrix} \begin{pmatrix} x \\ x' \end{pmatrix}_{z_0}, \tag{A.12}$$

$$\begin{pmatrix} y \\ y' \end{pmatrix}_{z_f} = \begin{pmatrix} R_{33} & R_{34} \\ R_{43} & R_{44} \end{pmatrix} \begin{pmatrix} y \\ y' \end{pmatrix}_{z_0}, \tag{A.13}$$

$$\begin{pmatrix} z \\ \delta p \end{pmatrix}_{z_f} = \begin{pmatrix} R_{55} & R_{56} \\ R_{65} & R_{66} \end{pmatrix} \begin{pmatrix} z \\ \delta p \end{pmatrix}_{z_0}. \tag{A.14}$$

Next, 2×2 transportation matrices of a drift space and quadrupole magnets are introduced. The mathematical treatments using hard edge model magnets to derive these matrices can be found in Ref. [83]. At the end, a formula for the beam matrix transformation matrices is presented.

A.2.1 Drift Space

For a drift space of length $\ell = z_f - z_0$, the transportation matrix for the motion in a transverse plane is

$$\mathscr{R}_{drift,transverse} = \begin{pmatrix} R_{11} & R_{12} \\ R_{21} & R_{22} \end{pmatrix} = \begin{pmatrix} R_{33} & R_{34} \\ R_{43} & R_{44} \end{pmatrix} = \begin{pmatrix} 1 & \ell \\ 0 & 1 \end{pmatrix}, \tag{A.15}$$

and one for the motion in the longitudinal plane is

$$\mathscr{R}_{drift,long} = \begin{pmatrix} R_{55} & R_{56} \\ R_{65} & R_{66} \end{pmatrix} = \begin{pmatrix} 1 & \frac{\ell}{\gamma^2} \\ 0 & 1 \end{pmatrix}, \tag{A.16}$$

where $\gamma = 1/\sqrt{1 - \frac{v^2}{c^2}}$ is the Lorentz factor of the electron.

A.2.2 Quadrupole Magnet

An electron beam is focused by a quadrupole magnet in one transverse plane and defocused in the other one. For a quadrupole magnet with an effective length of ℓ and focusing

strength of k, the transportation matrix in the focusing plane is

$$\mathscr{R}_{FQ} = \begin{pmatrix} \cos\sqrt{k\ell} & \frac{1}{\sqrt{k}}\sin\sqrt{k\ell} \\ -\sqrt{k}\sin\sqrt{k\ell} & \cos\sqrt{k\ell} \end{pmatrix}, \tag{A.17}$$

while one for the motion in the defocusing plane is

$$\mathscr{R}_{DQ} = \begin{pmatrix} \cosh\sqrt{k\ell} & \frac{1}{\sqrt{k}}\sinh\sqrt{k\ell} \\ \sqrt{k}\sinh\sqrt{k\ell} & \cosh\sqrt{k\ell} \end{pmatrix}, \tag{A.18}$$

and since quadrupole fields have no effects to the longitudinal motion, the transformation matrix for the motion in the longitudinal plane is similar to one of the drift space case as presented in Eq. (A.16).

A.2.3 Transformation in Phase Space

In order to use the transportation matrices with phase ellipse transformation, a phase ellipse can be represented by a beam matrix. Then, transformation of the beam matrix transported from position z_0 to position z_f can be derived by

$$\sigma_{z_f} = \mathscr{R}\sigma_{z_i}\mathscr{R}^T, \tag{A.19}$$

where $\mathscr{R}$ is the transport matrix and $\mathscr{R}^T$ is its transpose [83].

A.3 Electron Beam Parameters

Properties of an electron beam can be represented in forms of statistical parameters such as root mean square (RMS) or standard deviation values. Definitions of some parameters which are frequently used in this thesis are given in this section.

A.3.1 Beam size

The RMS beam size in the horizontal plane (x_{RMS}) can be calculated by

$$x_{rms} = \sqrt{\frac{\sum(x_i - \bar{x})^2}{n}}, \tag{A.20}$$

where n is a number of electrons. Accordingly, the RMS beam size in the vertical plane (y_{RMS}) can be calculated by

$$y_{RMS} = \sqrt{\frac{\sum(y_i - \bar{y})^2}{n}}, \tag{A.21}$$

and the RMS beam size in the longitudinal plane (z_{RMS}), called RMS bunch length, can be calculated by

$$z_{RMS} = \sqrt{\frac{\sum(z_i - \bar{z})^2}{n}}. \tag{A.22}$$

Note that z_{RMS} is often presented as a time duration of the bunch (RMS bunch duration; t_{RMS}) by

$$t_{RMS} \cong \frac{z_{RMS}}{c}. \tag{A.23}$$

where $c \approx 3 \times 10^8$ m/s is the speed of light in vacuum.

A.3.2 Beam momentum

Each electron has momentum components in all directions p_x, p_y and p_z. In case of a relativistic electron beam ($p_z >> p_x, p_y$), the transverse components are negligible when calculating a mean momentum of the electron beam

$$\bar{p} \approx \bar{p}_z = \frac{\sum p_{z,i}}{n}. \tag{A.24}$$

The RMS momentum, or also called momentum spread, can be calculated by

$$p_{z,RMS} = \sqrt{\frac{\sum(p_{z,i} - \bar{p}_z)^2}{n}}. \tag{A.25}$$

A.3.3 Beam emittance

The definition of geometrical emittance and normalized emittance are already given in Eq. (A.8) and Eq. (A.9), respectively.

Appendix B

S2E Simulations of THz SASE FEL based on PITZ Accelerator and the LCLS-I Undulator

The LCLS-I undulator module is a planar hybrid-permanent magnet undulator [9], and its important parameters are presented in Table B.1. LCLS-I undulators are available for loan from SLAC [105]. A re-usage of them for the proof-of-principle experiments of the THz SASE FEL at PITZ is quite interesting and understudies. This appendix presents S2E simulations from the photocathode to the THz SASE FEL generation in the undulator section.

Table B.1: Important parameters of the LCLS-I undulator module [9]

Parameter	**Detail**
Nominal gap	6.8 mm
Period length	30 mm
K-value	3.49
Total length	3.4 m
Number of period / a module	113 periods
Vacuum chamber sizes	11 mm $\times$ 5 mm

The ASTRA code [55] was used for beam dynamics simulations including generation of electron bunches in the RF gun, further acceleration by the CDS booster, further transport of the electron beam and matching into the undulator section, and simulations of the beam transport through the undulator section. Then, the best-obtained matching solution was used to simulate THz SASE FEL with a radiation wavelength of $\sim$100 µm using the Genesis 1.3 code [48].

B.1 Modeling of the LCLS-I Undulator Field

A measured field profile of a typical LCLS-I undulator [105] is presented in Fig. B.1a. This field profile was used to reconstruct a 3D magnetic field map used for simulations of the beam transport through the undulator section. Details about modeling of the undulator field by applying Fourier transformation to the measured field profile can be found in [108]. Figure B.1b shows the reconstructed magnetic field profile used in ASTRA simulations.

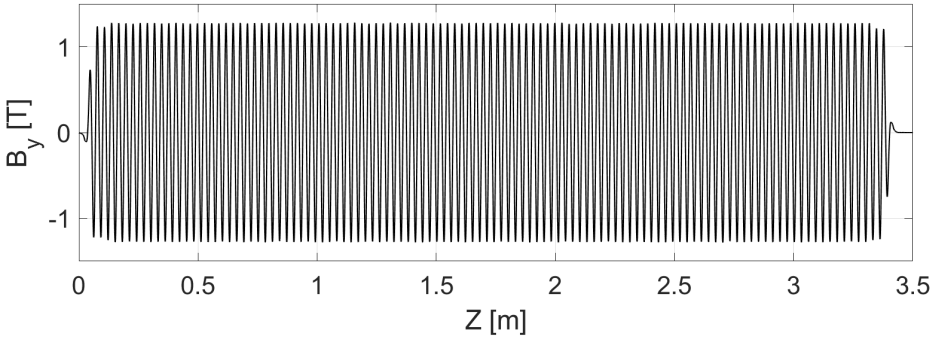

(a) Measured vertical magnetic field (B_y) along the beam direction

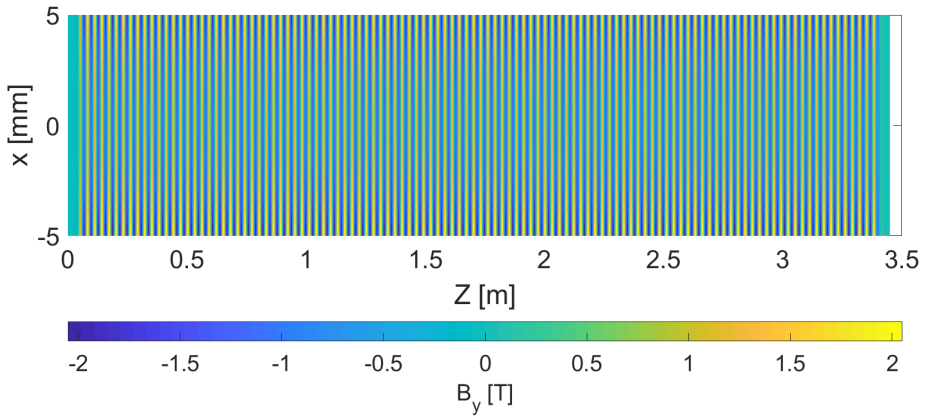

(b) Reconstructed vertical magnetic field (B_y) on the horizontal plane (xz-plane)

Figure B.1: Measured and reconstructed magnetic field profiles of the LCLS-I undulator.

In order to simulate electron beam dynamics along the undulator, ASTRA simulations were performed by using an ideal model electron distribution with a flattop temporal (7 mm FWHM) and Gaussian transverse phase spaces (projected emittance of 4 mm mrad). Twiss parameters of the input beam were tuned to minimize the beam size along the undulator and to have a beam waist at the center of the undulator length. Transverse phase spaces of the optimum setup are shown in Fig. B.2 and corresponding RMS sizes of the

matched electron beam in the undulator simulated by ASTRA are shown in Fig. B.3). The results of this matching will be used as a benchmark for the optimization of beam dynamics simulations.

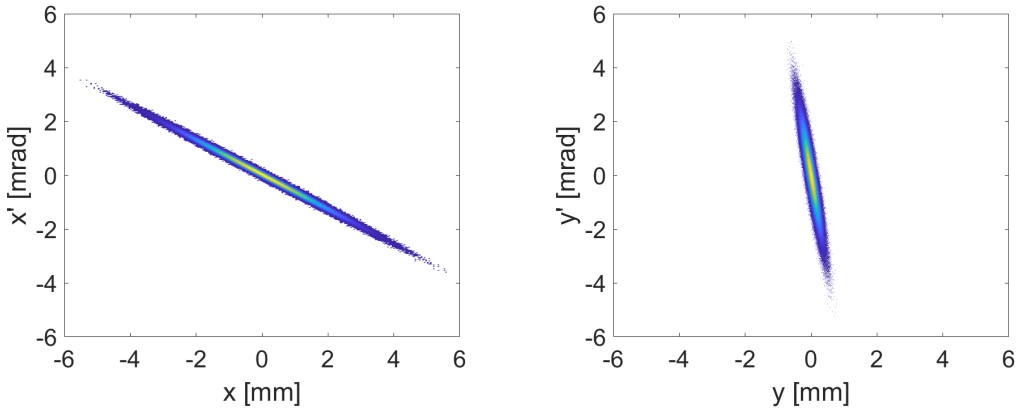

Figure B.2: Horizontal (left) and vertical (right) transverse phase spaces of the model beam matched into the undulator.

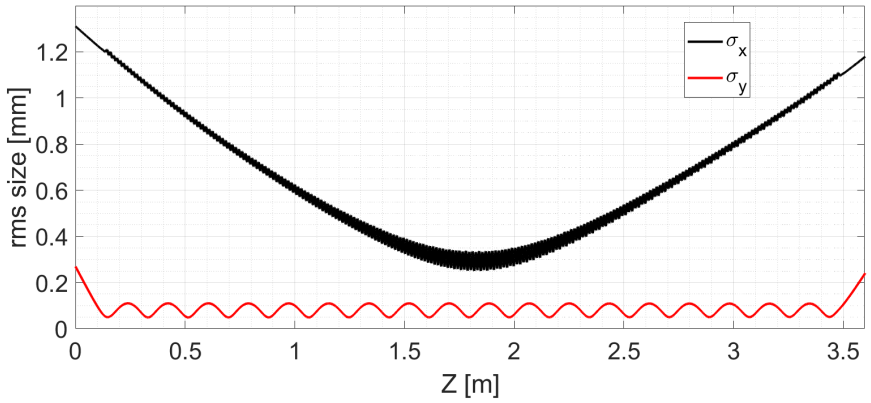

Figure B.3: RMS sizes of the matched electron beam in the undulator simulated by ASTRA.

B.2 Beam Dynamics Simulations

Simulations of Beam Generation and Acceleration by the Gun and the Booster Cavities

Beam dynamics simulations were performed using the ASTRA code [55] with 200000 macroparticles. The PITZ RF gun with a peak cathode field of 60 MV/m operated at the launch phase of maximum mean momentum gain (MMMG) is used to generate 4 nC electron bunches. Photocathode laser pulses with a flattop temporal profile (21.5 ps FWHM) and with a radially homogeneous transverse distribution were used. The diameter of the laser spot size was set to 5 mm. Beam mean longitudinal momentum of ∼16.7 MeV/c required for generating THz radiation with ∼100 μm radiation wavelength is achieved using a booster cavity. The booster cavity gradient and phase were tuned in order to yield the required mean beam momentum and a small correlated energy spread ($\langle zE \rangle \rightarrow 0$) of the electron beam close to the undulator (z = 29 m). This optimization resulted in a peak booster field of 12.85 MV/m and a phase of -26 deg w.r.t. MMMG. The main gun solenoid was tuned to control electron beam size and emittance.

Transverse and longitudinal phase spaces of the optimized electron beam at the first emittance measurement station (EMSY1 at z = 5.277 m) are shown in Fig. B.4. This beam setup was used as a starting point for studies on the space charge dominated beam transport towards the undulator section.

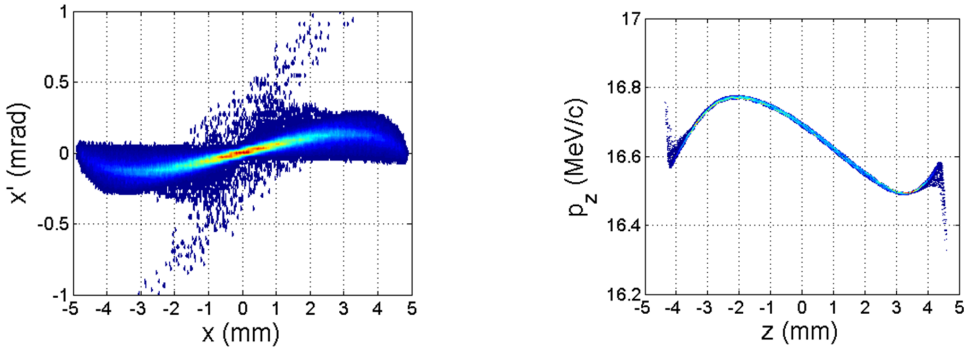

Figure B.4: Transverse (left) and longitudinal (right) phase spaces of the optimized electron beam at z = 5.277 m.

Simulations of Beam Transport to Undulator

Installation of LCLS-I undulators is foreseen in the PITZ tunnel annex for a proof-of-principle SASE THz experiment. The concrete wall between main and annex tunnels is 1.5 m thick and starts at ∼24 m downstream from the photocathode plane. This space is

considered for the electron beam to drift only without any focusing elements inside and assuming a standard beam pipe ($\phi = 35$ mm). Then, the beam has to transport through the undulator vacuum chamber (a racetrack profile with 5×11 mm cross-section and 3.4 m length [9]). In order to test the feasibility of such transport, a fast space charge tracking code Space Charge Optimizer (SCO) [90] was used. The results of ASTRA tracking till EMSY1 position (5.277 m) were used as an input for the SCO by applying a corresponding interface. Three triplets of quadrupole magnets were involved in optimization. First two of them were chosen from the magnets available in the present PITZ beamline, and the last one was assumed to be installed at the end of the main tunnel. The solution obtained from the optimized SCO tracking was plugged into the ASTRA input lattice. Results of the final ASTRA simulation are shown in Fig. B.5. Transverse and longitudinal phase spaces of the electron beam, as well as its slice parameters at the undulator entrance, are shown in Fig. B.6.

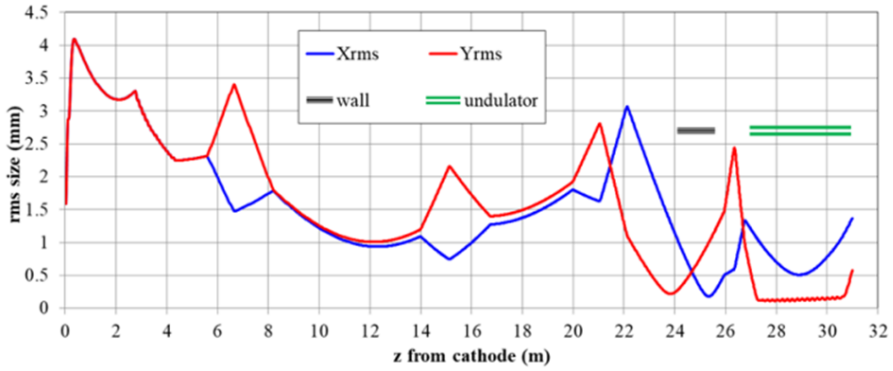

Figure B.5: Beam transport in the PITZ linac, including wall and undulator section (ASTRA simulations).

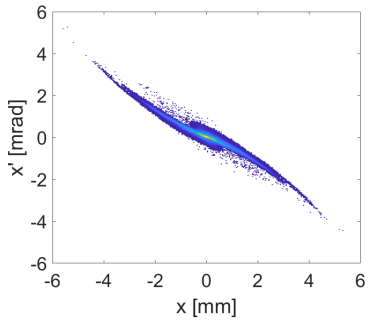

(a) Horizontal phase space

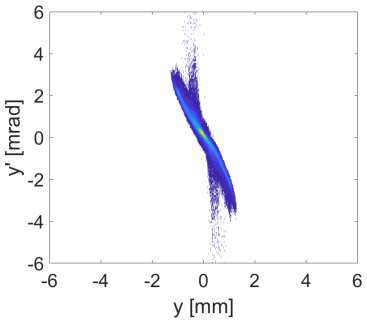

(b) Vertical phase space

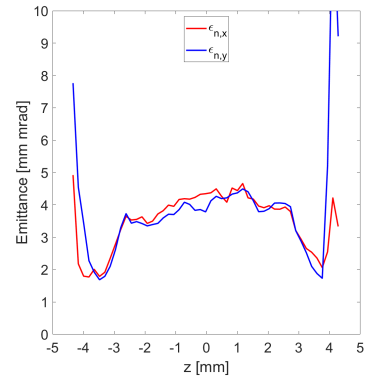

(c) Slice emittance

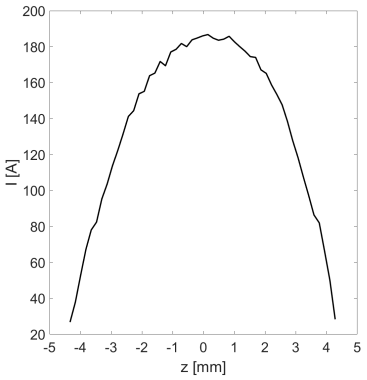

(d) Beam current

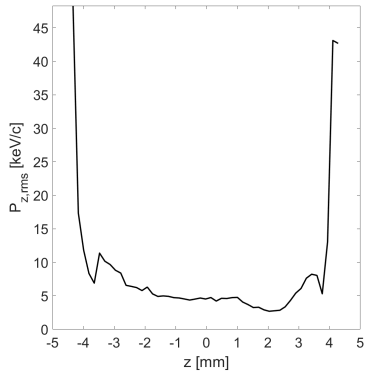

(e) Slice momentum spread

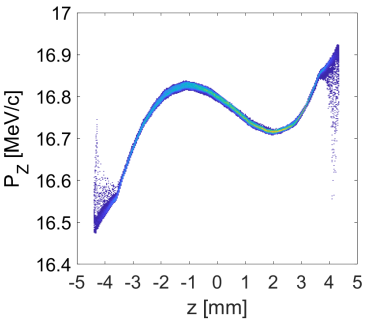

(f) Longitudinal phase space

Figure B.6: Phase space distributions ans longitudinal slice profiles of the matched beam at the undulator entrance.

B.3 THz SASE FEL Simulations

Electron beam parameters as shown in Fig. B.6 were used to simulate THz SASE FEL with the GENESIS 1.3 code [48]. Only one LCLS-I undulator was used and only the fundamental wavelength λ_u of the undulator field was included. The number of undulator periods was set to 113; no end cell features were included.

Results of GENESIS 1.3 simulations using the optimized input beam are shown in Fig. B.7. Grey curves refer to single-shot realizations, and the black curve corresponds to the average over a hundred realizations (simulation seeds). The main parameters of THz pulses obtained from the statistical analysis of hundred realizations are summarized in the Table B.2. The average THz pulse at the undulator exit has average pulse energy of 440 µJ (see black curve in the top plot of Fig. B.7) and has peak power of 32 MW with the RMS pulse duration is 6 ps (see black curve in the bottom-left plot of Fig. B.7). The average spectrum has a centre at ∼107 µm and a FWHM width of ∼5 µm (see black curves in the bottom-right plot of Fig. B.7).

Table B.2: Simulated THz radiation properties

Paramaters	**Values**
Pulse energy [mJ]	0.44 ± 0.11
Peak power [MW]	43.0 ± 10.2
Pulse RMS duration [ps]	5.6 ± 0.7
Centre wavelength [µm]	106.5
Spectrum width FWHM [µm]	4.5

Simulations of the THz SASE FEL for the PITZ setup with APPLE-II type undulator in Chapter 4 yielded rather high level of the radiation pulse energy (up to ∼3 mJ at 100 µm wavelength). Current start-to-end simulations of the proof-of-principle experiment resulted in a reduction of this level by a factor of 5. This can be related to the planar type of the LCLS-I undulator in contrary to the helical undulator APPLE-II used in Chapterr 4. The planar undulator assumes asymmetric beam matching and therefore less efficient interaction of electrons with the radiated field, whereas for the helical undulator the focusing in both transverse planes makes this interaction more homogeneous and efficient. Another source of the reduced THz power output is space charge effect, which should be taken into account by matching and transport of 4 nC and 16 MeV electron bunches in the narrow undulator gap.

B.4 Conclusion Remarks

Start-to-end beam dynamics simulations have been performed for the proof-of-principle experiment on THz SASE FEL generation at PITZ by using an LCLS-I undulator. Space

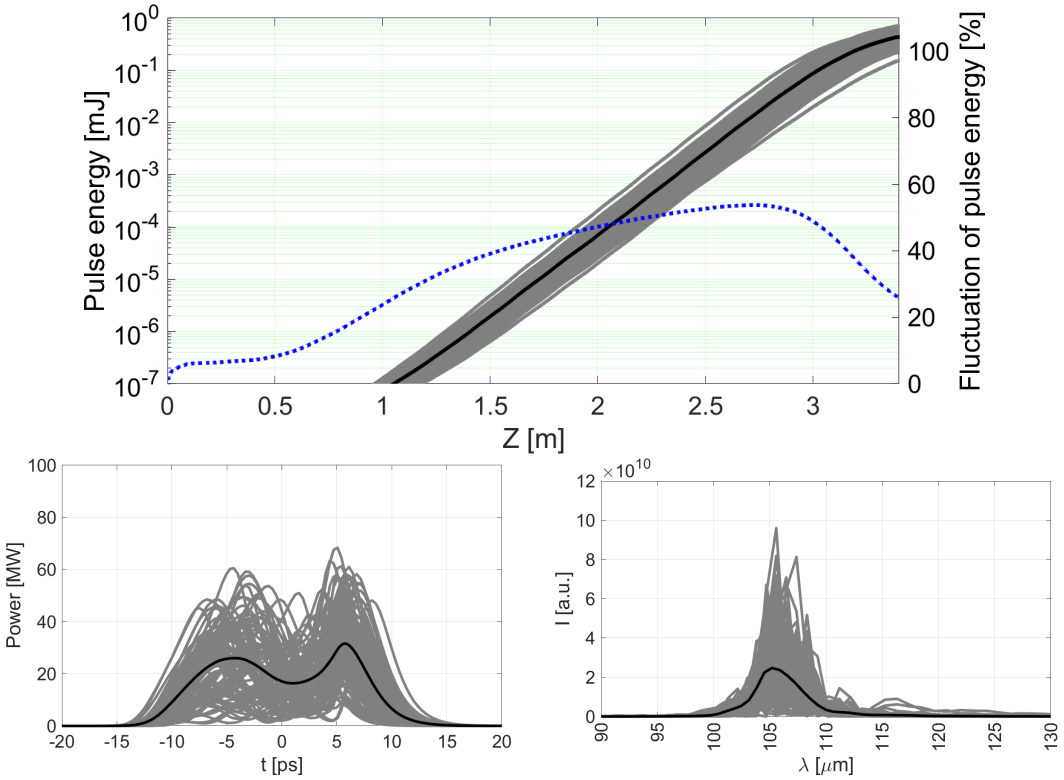

Figure B.7: Results of THz SASE FEL simulations with GENESIS code for the 100 µm case. Pulse energy along the undulator for the nominal (a) and tuned (b) beams. The blue dotted line shows the fluctuation of the pulse energy along the undulator axis. Radiation pulse profile at the undulator exit for the nominal (c) and tuned (d) beams. Corresponding spectra at the undulator exit for the nominal (e) and tuned (f) beams.

charge dominated electron beam transport through the PITZ accelerator was optimized by combining and iterating ASTRA and SCO codes. Obtained electron beam 6D phase space at the undulator entrance was used as an input for the THz SASE FEL simulations by means of GENESIS 1.3. The simulated THz pulse has an average pulse energy of 440 µJ at the center wavelength of ∼100 µm.

Several effects are still not considered in the simulations: the possible impact of the narrow vacuum chamber of the undulator (wakefield of electron bunch and waveguide effect of the FEL process). The space charge model used in ASTRA and GENESIS simulations inside the undulator has limited applicability. The impact of possible undulator imperfections onto beam transport and FEL radiation has still to be estimated as well.

References

[1] The Southeastern Universities Research Association (SURA), *SURA | Technology Commercialization | Terahertz*. http://www.sura.org/commercialization/terahertz.html.

[2] M. Altarelli *et al.*, "XFEL, the European X-ray Free-Electron Laser: Technical Design Report," Tech. Rep. DESY 2006-097, DESY, July 2007.

[3] European XFEL GmbH, *European XFEL*. https://www.xfel.eu/index_eng.html.

[4] K. J. Gaffney and H. N. Chapman, "Imaging Atomic Structure and Dynamics with Ultrafast X-ray Scattering," *Science*, vol. 316, pp. 1444–1448, June 2007.

[5] S. S. Dhillon *et al.*, "The 2017 Terahertz Science and Technology Roadmap," *Journal of Physics D: Applied Physics*, vol. 50, no. 4 043001, 2017.

[6] R. A. Lewis, "A Review of Terahertz Sources," *Journal of Physics D: Applied Physics*, vol. 47, no. 37 374001, 2014.

[7] S. L. Dexheimer, *Terahertz Spectroscopy: Principles and Applications*, vol. 131 of *Optical Science and Engineering*. CRC Press, 2008.

[8] K.-E. Peiponen, A. Zeitler, and M. Kuwata-Gonokami, *Terahertz Spectroscopy and Imaging*, vol. 171 of *Springer Series in Optical Sciences*. Berlin, Heidelberg: Springer Berlin Heidelberg, 2013.

[9] J. Stohr, "Linac Coherent Light Source II (LCLS-II) Conceptual Design Report," Tech. Rep. SLAC-R-978, SLAC National Accelerator Laboratory, Menlo Park, CA, USA, Nov. 2011.

[10] A. S. Fisher *et al.*, "THz Pump and X-Ray Probe Development at LCLS," in *Proceedings of 33rd International Free-Electron Laser Conference 2011*, (Shanghai, China), Aug. 2011. TUPB22.

[11] R. Ganter, "SwissFEL Conceptual Design Report," Tech. Rep. PSI Bericht Nr. 10-04, The Paul Scherrer Institute (PSI), July 2010.

[12] P. Zalden *et al.*, "Terahertz Science at European XFEL," Tech. Rep. XFEL.EU TN-2018-001-01.0, The European XFEL, 2018.

[13] M. Pergament *et al.*, "Versatile Optical Laser System for Experiments at the European X-ray Free-electron Laser Facility," *Optics Express*, vol. 24, Dec. 2016.

[14] W. Ackermann *et al.*, "Operation of a Free-electron Laser from the Extreme Ultraviolet to the Water Window," *Nature Photonics*, vol. 1, pp. 336–342, June 2007.

[15] F. Stephan *et al.*, "Detailed Characterization of Electron Sources yielding First Demonstration of European X-ray Free-Electron Laser Beam Quality," *Physical Review Special Topics - Accelerators and Beams*, vol. 13, Feb. 2010.

[16] M. Krasilnikov *et al.*, "Experimentally Minimized Beam Emittance from an L-band Photoinjector," *Physical Review Special Topics - Accelerators and Beams*, vol. 15, Oct. 2012.

[17] I. Isaev *et al.*, "Conditioning Status of the First XFEL Gun at PITZ," in *Proceedings of 35th International Free-Electron Laser Conference 2013*, (Manhattan, USA), Aug. 2013. TUPSO30.

[18] M. Otevrel *et al.*, "Report on Gun Conditioning Activities at PITZ in 2013," in *Proceedings of 5th International Particle Accelerator Conference 2014*, (Dresden, Germany), June 2014. THPRO044.

[19] E. Schneidmiller, M. Yurkov, M. Krasilnikov, and F. Stephan, "Tunable IR/THz Source for Pump Probe Experiments at the European XFEL," in *Proceedings of 34th International Free-Electron Laser Conference 2012*, (Nara, Japan), Aug. 2012. WEPD55.

[20] M. Gensch, "Follow up on THz Radiation." Presentation of ARD-ST3 Annual Workshop, DESY, Zeuthen, Germany, July 2017.

[21] S. T. Thornton and A. F. Rex, *Modern Physics for Scientists and Engineers*. Boston, MA, USA: Cengage Learning, 4th ed., 2013.

[22] A. I. Fisenko and V. Lemberg, "On the Radiative and Thermodynamic Properties of the Extragalactic Far Infrared Background Radiation Using COBE FIRAS Instrument Data," *Astrophysics and Space Science*, vol. 352, pp. 231 – 234, July 2014.

[23] Bommel, Wout van and Rouhana, Abdo, *Lighting Hardware*. Koninklijke Philips Electronics N.V., Sept. 2011.

[24] L. M. Lepodise, *THz Spectroscopic Studies of Materials Using the FTIR Technique: Experiment and Simulation*. PhD thesis, University of Wollongong, Wollongong, New South Wales, Australia, 2014.

[25] P. Schmüser, M. Dohlus, J. Rossbach, and C. Behrens, *Free-Electron Lasers in the Ultraviolet and X-Ray Regime: Physical Principles, Experimental Results, Technical Realization*. Springer, Cham, 2014.

[26] R. A. Lewis, *Terahertz Physics*. Cambridge University Press, 2012.

[27] RP Photonics Consulting GmbH, *Encyclopedia of Laser Physics and Technology - CO2 Lasers, Carbon Dioxide Laser*. https://www.rp-photonics.com/co2_lasers.html/.

[28] R. A. Meyers, *Encyclopedia of Lasers and Optical Technology*. New York, USA: Academic Press, 1991.

[29] Synrad, a Novanta company, *p Series 100W - 400W CO2 Lasers - Synrad*. https://www.synrad.com/products/lasers/p-series/.

[30] O. A. Klimenko *et al.*, "Terahertz Wide Range Tunable Cyclotron Resonance p-Ge Laser," *Journal of Physics: Conference Series*, vol. 193, p. 012064, Nov. 2009.

[31] R. Pecharroman-Gallego, "An Overview on Quantum Cascade Lasers: Origins and Development," in *Quantum Cascade Lasers* (V. N. Stavrou, ed.), InTech, Apr. 2017.

[32] L. Li *et al.*, "Terahertz Quantum Cascade Lasers with 1 W Output Powers," *Electronics Letters*, vol. 50, pp. 309–311, Feb. 2014.

[33] R. W. BOYD, *Nonlinear Optics*. Elsevier Academic Press, 3rd ed., 2008.

[34] J. A. Fülöp *et al.*, "Efficient Generation of THz Pulses with 0.4 mJ Energy," *Optics Express*, vol. 22, Aug. 2014.

[35] C. Vicario *et al.*, "High efficiency THz generation in DSTMS, DAST and OH1 pumped by Cr:Forsterite Laser," *Optics Express*, vol. 23, Feb. 2015.

[36] I.-C. Ho, X. Guo, and X.-C. Zhang, "Design and Performance of Reflective Terahertz Air-Biased-Coherent-Detection for Time-Domain Spectroscopy," *Optics Express*, vol. 18, Feb. 2010.

[37] A. Sell, A. Leitenstorfer, and R. Huber, "Phase-Locked Generation and Field-Resolved Detection of Widely Tunable Terahertz Pulses with Amplitudes Exceeding 100 MV/cm," *Optics Letters*, vol. 33, Dec. 2008.

[38] B. Liu, H. Bromberger, A. Cartella, T. Gebert, M. Först, and A. Cavalleri, "Generation of Narrowband, High-Intensity, Carrier-Envelope Phase-Stable Pulses Tunable Between 4 and 18 THz," *Optics Letters*, vol. 42, Jan. 2017.

[39] M. Beck, H. Schäfer, G. Klatt, J. Demsar, S. Winnerl, M. Helm, and T. Dekorsy, "Impulsive Terahertz Radiation with High Rlectric Fields from an Amplifier-Driven Large-Area Photoconductive Antenna," *Optics Express*, vol. 18, Apr. 2010.

[40] A.-S. Müller and M. Schwarz, "Accelerator-Based THz Radiation Sources," in *Synchrotron Light Sources and Free-Electron Lasers* (E. Jaeschke, S. Khan, J. R. Schneider, and J. B. Hastings, eds.), Springer, Cham, 2015.

[41] J. A. Clarke, *The Science and Technology of Undulators and Wigglers*. Oxford University Press, July 2004.

[42] C. T. Settakorn, *Coherent THz Transition Radiation: Generation, Characterization, and Applications*. VDM-Verl. Müller, 2010.

[43] S. Casalbuoni, B. Schmidt, and P. Schmüser, "Far-Infrared Transition and Diffraction Radiation - Part I: Production, Diffraction Effects and Optical Propagation," Tech. Rep. TESLA Report 2005-15, DESY, 2005.

[44] A. W. Chao and M. Tigner, *Handbook of Accelerator Physics and Engineering*. River Edge, NJ, USA: World Scientific, 1999.

[45] K. Bane and G. Stupakov, "TerahertzRadiation from a Pipe with Small Corrugations," *Nuclear Instruments and Methods in Physics Research Section A: Accelerators, Spectrometers, Detectors and Associated Equipment*, vol. 677, pp. 67–73, June 2012.

[46] R. Bosch, "Focusing of Infrared Edge and Synchrotron Radiation," *Nuclear Instruments and Methods in Physics Research Section A: Accelerators, Spectrometers, Detectors and Associated Equipment*, vol. 431, pp. 320–333, July 1999.

[47] E. L. Saldin, E. A. Schneidmiller, and M. V. Yurkov, *The Physics of Free Electron Lasers*. Advanced Texts in Physics, Berlin, Heidelberg: Springer Berlin Heidelberg, 2000.

[48] S. Reiche, *Genesis1.3 code*. http://genesis.web.psi.ch/.

[49] E. Saldin, E. Schneidmiller, and M. Yurkov, "FAST: a Three-Dimensional Time-Dependent FEL Simulation Code," *Nuclear Instruments and Methods in Physics Research Section A: Accelerators, Spectrometers, Detectors and Associated Equipment*, vol. 429, no. 1, pp. 233 – 237, 1999.

[50] H. Freund and P. van der Slot, "MINERVA, A New Code to Model Free-Electron Lasers," in *Proceedings of The 36th International Free Electron Laser Conference 2014*, (Basel, Switzerland), Aug. 2014. TUP020.

[51] T. Tanaka, "SIMPLEX: Simulator and Postprocessor for Free-Electron Laser Experiments," *Journal of Synchrotron Radiation*, vol. 22, pp. 1319–1326, Sept. 2015.

[52] S. Casalbuoni, B. Schmidt, P. Schmüser, and B. Steffen, "Far-Infrared Transition and Diffraction Radiation - Part II: The THz Beamline at the VUV-FEL Linac," Tech. Rep. 2006-04, DESY, 2006.

[53] J. H. Booske *et al.*, "Vacuum Electronic High Power Terahertz Sources," *IEEE Transactions on Terahertz Science and Technology*, vol. 1, pp. 54–75, Sept. 2011.

[54] M. Thumm, "State-of-the-Art of High Power Gyro-Devices and Free Electron Masers. Update 2016," Tech. Rep. KIT Scientific Reports; 7735, KIT Scientific Publishing, 2017.

[55] K. Flöttmann, *A Space Charge Tracking Algorithm (ASTRA)*. http://www.desy.de/~mpyflo/.

[56] M. Gensch, "Super-Radiant Linac-Based THz Sources in 2013," in *Proceedings of the 35th International Free-Electron Laser Conference 2013*, (New York, USA), Aug. 2013. WEIBNO01.

[57] P. Neyman, W. Colson, S. Gottshalk, J. Blau, and K. Cohn, "Free Electron Lasers in 2017," in *Proc. of 38th International Free Electron Laser Conference 2017*, (Santa Fe, NM, USA), Aug. 2017. MOP066.

[58] Y. Saveliev *et al.*, "Recent Developments on ALICE (Accelerators and Lasers In Combined Experiments) at Daresbury Laboratory," in *Proc. of International Particle Accelerator Conference 2010*, (Kyoto, Japan), May 2010.

[59] G. Andonian *et al.*, "Observation of Coherent Terahertz Edge Radiation from Compressed Electron Beams," *Phys. Rev. ST Accel. Beams*, vol. 12, p. 030701, Mar 2009.

[60] HZDR, *High-Field High-Repetition-Rate Terahertz facility @ ELBE (TELBE)*. https://www.hzdr.de/db/Cms?pNid=2609.

[61] W. Schöllkopf *et al.*, "The new IR and THz FEL facility at the Fritz Haber Institute in Berlin," in *Proc.SPIE*, vol. 9512, 2015.

[62] G. Isoyama, R. Kato, S. Kashiwagi, T. Igo, and Y. Morio, "Development of FEL and SASE in the far-infrared region at ISIR, Osaka University," *Infrared Physics and Technology*, vol. 51, no. 5, pp. 371 – 374, 2008.

[63] Y. Shen *et al.*, "Nonlinear Cross-Phase Modulation with Intense Single-Cycle Terahertz Pulses," *Phys. Rev. Lett.*, vol. 99, p. 043901, Jul 2007.

[64] K. Lekomtsev, A. Aryshevpresenter, M. Shevelev, N. Terunuma, J. Urakawa, A. Ponomarenko, and A. Tishchenko, "Experimental Investigation of THz Smith-Purcell Radiation From Composite Corrugated Capillary," in *Proceedings of the 7th International Particle Accelerator Conference*, (Busan, Korea), May 2016. TUPOW044.

[65] K. Bane, S. Antipov, M. Fedurin, K. Kusche, C. Swinson, and D. Xiang, "Measurement of Terahertz Generation in a Metallic, Corrugated Beam Pipe," in *Proceedings of 38th International Free-Electron Laser Conference 2017*, (Busan, Korea), May 2016. TUPOW053.

[66] F. Stephan and M. Krasilnikov, "High Brightness Photo Injectors for Brilliant Light Sources," in *Synchrotron Light Sources and Free-Electron Lasers* (E. Jaeschke, S. Khan, J. R. Schneider, and J. B. Hastings, eds.), Springer, Cham, 2016.

[67] M. Gross *et al.*, "Preparations for a Plasma Wakefield Acceleration (PWA) Experiment at PITZ," *Nucl. Instrum. Methods Phys. Res A*, vol. 740, pp. 74–80, 2014.

[68] M. Gross *et al.*, "Observation of the Self-Modulation Instability via Time-Resolved Measurements," *Phys. Rev. Lett.*, vol. 120, p. 144802, Apr 2018.

[69] O. Lishilin, *Study of Self-Modulation of an Electron Beam in Plasma*. Dissertation, University of Hamburg, Hamburg, 2019.

[70] H. Qian, M. Gross, M. Krasilnikov, a. Oppelt, and F. Stephan, "Investigation of High Repetition Rate Femtosecond Electron Diffraction at PITZ," in *Proc. of International Particle Accelerator Conference 2017*, (Copenhagen, Denmark), May 2017.

[71] D. Zahn and H. Qian, "First MeV electron diffraction test at PITZ." Presentation of PITZ Collaboration Meeting, DESY, Zeuthen, Germany, Dec. 2017.

[72] I. Will, G. Koss, and I. Templin, "The Upgraded Photocathode Laser of the TESLA Test Facility," *Nucl. Instrum. Methods Phys. Res A*, vol. 541, no. 3, pp. 467–477, 2005.

[73] S. Lederer *et al.*, "Investigations on the Increased Lifetime of Photocathodes at FLASH and PITZ," in *Proceedings of the 23rd Particle Accelerator Conference 2009*, (Vancouver, British Columbia, Canada), May 2009.

[74] M. Hänel, *Experimental Investigations on the Influence of the Photocathode Laser Pulse Parameters on the Electron Bunch Quality in an RF Photoelectron Source*. PhD thesis, University of Hamburg, Hamburg, Germany, 2010.

[75] M. Gross, "PITZ Laser Systems." Presentation in Technisches Seminar, DESY, Zeuthen, Germany, Nov. 2017.

[76] I. Will and G. Klemz, "Generation of flat-top Picosecond Pulses by Coherent Pulse Stacking in a Multicrystal Birefringent filter," *Optics express*, vol. 16, no. 19, pp. 14922–14937, 2008.

[77] B. Dwersteg, K. Flöttmann, J. Sekutowicz, and C. Stolzenburg, "RF Gun Design for the TESLA VUV Free Electron Laser," *Nucl. Instrum. Methods Phys. Res A*, vol. 393, no. 1, pp. 93 – 95, 1997.

[78] V. Paramonov *et al.*, "The PITZ CDS Booster Cavity RF Tuning and Start of Conditioning," in *Proceedings of Linear Accelerator Conference LINAC2010*, (Tsukuba, Japan), Sept. 2010. MOP081.

[79] Danfysik A/S, *Danfysik*. http://www.danfysik.com/en/products/magnets/conventional/.

[80] PITZ, *Magnets - PITZ: PITZ Wiki*. https://wiki-zeuthen.desy.de/PITZ/Magnets.

[81] B. Instrumentation, *Bergoz Instrumentation*. http://www.bergoz.com/.

[82] Allied Vision Technologies GmbH., *Machine Vision Cameras Selector - Allied Vision*. https://www.alliedvision.com/en/products/cameras.html.

[83] H. Wiedemann, *Particle Accelerator Physics*. Berlin: Springer, 3rd ed., 2007.

[84] J. Rönsch, *Investigations on the Electron Bunch Distribution in the Longitudinal Phase Space at a Laser Driven RF Electron Source for the European X-FEL*. PhD thesis, University of Hamburg, Hamburg, Germany, 2010.

[85] D. Malyutin, *Time Resolved Transverse and Longitudinal Phase Space Measurements at the High Brightness Photo Injector PITZ*. PhD thesis, University of Hamburg, Hamburg, Germany, 2014.

[86] S. Rimjaem *et al.*, "Optimizations of Transverse Projected Emittance at the Photo-Injector Test facility at DESY, Location Zeuthen," *Nucl. Instrum. Methods Phys. Res A*, vol. 671, pp. 62 – 75, 2012.

[87] L. Kravchuk *et al.*, "Layout of the PITZ Transverse Deflecting System for Longitudinal Phase Space and Slice Emittance Measurements," in *Proceedings of International Linear Accelerator Conference, LINAC2010*, (Tsukuba, Japan), Sept. 2011. TUP011.

[88] S. Sasaki, "Analyses for a Planar Variably-Polarizing Undulator," *Nuclear Instruments and Methods in Physics Research Section A: Accelerators, Spectrometers, Detectors and Associated Equipment*, vol. 347, pp. 83–86, Aug. 1994.

[89] M. Altarelli *et al.*, "FERMI@Elettra Conceptual Design Report," Tech. Rep. DESY 2006-097, DESY, July 2007.

[90] A. Bondarenko and A. Matveenko, "Implementation of 2D-emittance Compensation Scheme in the BERLinPro Injector," in *Proceedings of 33rd International Free-Electron Laser Conference 2011*, (Shanghai, China), Aug. 2011. THPB02.

[91] S. G. Anderson *et al.*, "Velocity Bunching of High-brightness Electron Beams," *Phys. Rev. ST Accel. Beams*, vol. 8, p. 014401, Jan 2005.

[92] M. Ferrario *et al.*, "Velocity Bunching Experiments at SPARC," in *Proceedings of the 23rd Particle Accelerator Conference*, (Vancouver, BC, Canada), May 2009. MO6RFP071.

[93] S. Di Mitri, "Bunch Length Compressors," *CERN Yellow Reports: School Proceedings*, vol. 1, 2018.

[94] B. Zeitler, K. Floettmann, and F. Grüner, "Linearization of the Longitudinal Phase Space without Higher Harmonic Field," *Phys. Rev. ST Accel. Beams*, vol. 18, p. 120102, Dec 2015.

[95] B. Marchetti *et al.*, " Novel Schemes for the Optimization of the SPARC Narrow Band THz Source," *Review of Scientific Instruments*, vol. 86, p. 073301, July 2015.

[96] C. Hernandez-Garcia *et al.*, "Charge Production Studies from Cs2Te Photocathodes in a Normal Conducting RF Gun," *Nuclear Instruments and Methods in Physics Research Section A: Accelerators, Spectrometers, Detectors and Associated Equipment*, vol. 871, pp. 97–104, Nov. 2017.

[97] M. Krasilnikov *et al.*, "Electron Beam Asymmetry Compensation with Gun Quadrupoles at PITZ," in *Proceedings of 38th International Free-Electron Laser Conference 2017*, (Santa Fe NM, USA), Aug. 2017. WEP007.

[98] F. Löhl, *Measurements of the Transverse Emittance at the VUV-FEL*. Diploma thesis, University of Hamburg, Hamburg, Germany, 2005.

[99] B. Beutner, "Emittance Measurement at the European XFEL." Internal Presentation in PITZ Physics Seminar, DESY, Zeuthen, Germany, Oct. 2016.

[100] G. Vashchenko, *Transverse Phase Space Studies with the New CDS Booster Cavity at PITZ*. PhD thesis, University of Hamburg, Hamburg, Germany, 2013.

[101] TSL, *Viewports*. http://torrscientific.co.uk/viewports/.

[102] SLT Sensor- und Lasertechnik GmbH, *pyrosensor.de — Lasermessköpfe aus Deutschland*. http://www.pyrosensor.de/.

[103] TYDEX, *TYDEX THz Beam Splitters*. http://www.tydexoptics.com/products/thz_optics/thz_beam_splitter/.

[104] B. Schmidt, *THzTransport*, 2017. For information on the Mathematica code THz-Transport please contact: bernhard.schmidt@desy.de.

[105] H.-D. Nuhn. Personal Communication, 2017.

[106] K. Flöttmann, "Some basic features of the beam emittance," *Phys. Rev. ST Accel. Beams*, vol. 6, p. 034202, Mar 2003.

[107] D. C. Carey, K. L. Brown, and F. Rothacker, "Third order TRANSPORT with MAD input: A Computer program for designing charged particle beam transport systems," Tech. Rep. SLAC-R-0530, SLAC National Accelerator Laboratory, Menlo Park, CA, USA, 1998.

[108] M. Krasilnikov, P. Boonpornprasert, F. Stephan, E. Schneidmiller, M. Yurkov, and H.-D. Nuhn, "Start-to-End Simulations of THz SASE FEL Proof-of-Principle Experiment at PITZ," in *Proceedings of 13th Int. Computational Accelerator Physics Conf.*, (Key West, FL, USA), Oct. 2019. TUPAF23.